DISS. ETH NO. 24805

A 40 000 000 RPM MAGNETICALLY LEVITATED SPINNING BALL MOTOR

A thesis submitted to attain the degree of

DOCTOR OF SCIENCES of ETH ZURICH

(Dr. sc. ETH Zurich)

presented by

MARCEL SCHUCK

M.Sc. University of Illinois at Urbana-Champaign
MBA, Collège des Ingénieurs

born on *21.07.1988*

citizen of *Germany*

accepted on the recommendation of

Prof. Dr. Johann W. Kolar, examiner
Prof. Dr. Robert Pilawa-Podgurski, co-examiner

2017

Acknowledgments

I would like to express my gratitude to all the people who encouraged and supported me during my PhD studies both on a scientific and personal level.

I am very thankful to Prof. Dr. Johann W. Kolar for giving me the opportunity to conduct this interesting and interdisciplinary project under his guidance and for providing a highly inspiring, creative, and motivating environment at the Power Electronic Systems Laboratory (PES). I deeply appreciate the trust and autonomy I was granted when carrying out this research.

I am very grateful to Prof. Dr. Robert Pilawa-Podgurski for agreeing to be the co-examiner of this thesis. I am also very thankful to him for sharing his extensive knowledge with me and for providing me with a well-founded introduction to the field of power electronics.

Furthermore, I am also indebted to Prof. Dr. Jörg Hugel, whose financial support through the Else & Friedrich Hugel Fund for Mechatronics made it possible to carry out this project. His continuous personal support and interest in the research served as a great motivational factor.

I am sincerely thankful to my colleagues Dr. Tobias Wellerdieck, Pascal Püntener, Thomas Holenstein, and Patricio Peralta for the many fruitful discussions and excellent collaboration. I am much indebted to Dr. Daniel Steinert and Dr. Thomas Nussbaumer for their continuous support and valuable contributions to this project.

During my PhD studies I was positively influenced by all my colleagues and the very helpful staff at the PES, as well as at the collaborating company Levitronix GmbH. I am deeply thankful for these valuable experiences.

Many thanks go to all the students who spent their time and effort conducting their academic internship, group project, semester thesis, or master thesis under my supervision. Their interest and valuable contributions to this work are much appreciated.

I would like to thank my friends for their encouragement and for creating such a pleasant environment.

Last but not least, I would like to thank my girlfriend Jacqueline Alexander and my family for their love and support without which this work would not have been possible.

Zurich, November 2017
Marcel Schuck

Contents

Abstract

Electrical power is largely converted to or from mechanical energy using electric motors. Several applications have driven the miniaturization of these machines, which requires high rotational speeds to achieve a desired power level at a decreased size. Rotational speeds of several hundred thousand revolutions per minute (rpm) have been used industrially, and drive systems in research environments have reached rotational speeds of up to one million rpm. The highest measured rotational speed achieved with an electrically driven rotor was 37.98 million rpm and dates back to 1947. Since then, this speed has not been reproduced or exceeded, despite subsequent efforts. In conjunction with the application-driven trend toward high rotational speeds, this has fostered interest in the underlying physical limitations regarding the achievable rotational speed, independent of a specific application. To explore these boundaries and to provide technological solutions for the related challenges, the design and implementation of an electric motor capable of reaching 40 million rpm is reported in this work.

Submillimeter scale steel spheres are used as rotors, which were selected based on their structural and dynamic stability. To limit bearing and gas friction losses at such ultra-high rotational speeds, the rotor is magnetically suspended inside a vacuum without mechanical contact. Acceleration is carried out by the principle of a solid rotor induction machine, for which a detailed analytical model is provided. A suitable stator design using power ferrite cores for magnetic field frequencies in the megahertz range is developed. The design of an optical sensor system, which measures the rotor position without mechanical contact in all degrees of freedom, is outlined. This system provides the input to the high bandwidth digital control scheme required for active magnetic stabilization of the rotor. A power electronic converter system capable of generating the high frequency drive currents as well as the bearing currents necessary for magnetic suspension is presented. All subsystems were assembled to provide an experimental prototype of the ultra-high-speed motor.

During a series of acceleration experiments with various rotor sizes and materials, a rotational speed slightly above 40 million rpm was reached with a rotor of 0.5 mm in diameter, which is, to the knowledge of the author, the highest rotational speed achieved by an electrically driven rotor to date. Circumferential speeds exceeding 1000 m/s and centrifugal accelerations of more than 4×10^8 times the gravitational acceleration were reached. The results open up new research possibilities, such as the testing of materials under extreme centrifugal load, and provide insights for the development of future ultra-high-speed electric drive systems.

Kurzfassung

Elektrische Energie wird in einer Vielzahl technischer Anwendungen mittels Generatoren aus mechanischer Energie gewonnen oder in Elektromotoren in solche umgewandelt, wobei der Miniaturisierung i. Allg. hohe Bedeutung zukommt. Um die Maschinengröße bei gleichbleibender Leistung zu verringern ist der Einsatz hoher Drehzahlen notwendig. Drehzahlen von mehreren hunderttausend Umdrehungen pro Minute (U/min) werden bereits im industriellen Umfeld eingesetzt. Mit Antriebssystemen unter Laborbedingungen konnten bis zu einer Million U/min erreicht werden. Die höchste gemessene mit einem elektrisch angetriebenen Rotor erzielte Drehzahl wurde bereits 1947 publiziert und lag bei 37,98 Millionen U/min. Trotz nachfolgender Versuche konnte dieser Drehzahlwert seither nicht reproduziert oder überschritten werden. Dieser Sachverhalt, in Kombination mit dem genannten anwendungsgetriebenen Entwicklungstrend zu hohen Drehzahlen, resultierte im Interesse an den zugrundeliegenden physikalischen Limitierungen hinsichtlich der unabhängig von einer spezifischen Anwendung erreichbaren Drehzahlen. Zur Untersuchung dieser Grenzen und um technologische Lösungen für die damit in Bezug stehenden Herausforderungen zu erforschen beschreibt die vorliegende Arbeit die Entwicklung und Implementierung eines Elektromotors welcher imstande ist Drehzahlen von bis zu 40 Millionen U/min zu erreichen.

Aufgrund ihrer strukturellen und dynamischen Stabilität werden Stahlkugeln mit Größen im Submillimeterbereich als Rotoren eingesetzt. Um Verluste aufgrund von Lager- und Gasreibung bei hohen Drehzahlen zu begrenzen wird der Rotor im Vakuum kontaktfrei magnetisch gelagert. Seine Beschleunigung erfolgt nach dem Prinzip einer Kurzschlussläufer-Asynchronmaschine für welches ein detailliertes analytisches Model präsentiert wird. Ein geeignetes Statordesign welches Leistungsferrite als Kerne verwendet und für Magnetfeldfrequenzen im Megahertzbereich geeignet ist wird präsentiert. Weiterhin wird die Entwicklung eines optischen Sensorsystems, welches in der Lage ist die Position des Rotors in allen Freiheitsgraden kontaklos zu messen, vorgestellt. Dieses System

stellt die Eingangssignale für ein digitales Regelungsschema bereit das zur aktiven magnetischen Stabilisierung des Rotors benötigt wird. Ein leistungselektronisches Konvertersystem zur Generierung der hochfrequenten Antiebsströme sowie der Spulenströme für die magnetische Lagerung wird vorgestellt. Alle Subsysteme wurden zu einem funktionsfähigen experimentellen Prototyp des Ultrahochgeschwindigkeitsmotors kombiniert.

Im Rahmen einer Reihe von Beschleunigungsexperimenten mit verschiedenen Rotorgrößen und Materialien konnte eine Drehzahl von über 40 Millionen U/min bei einem Rotordurchmesser von 0.5 mm erreicht werden. Nach Wissen des Autors entspricht dies der höchsten jemals mit einem elektrisch angetriebenen Rotor erreichten Drehzahl. Umfangsgeschwindigkeiten von mehr als 1000 m/s und Zentrifugalbeschleunigungen oberhalb des 4×10^8-fachen der Erdbeschleunigung wurden erreicht. Die Ergebnisse eröffnen neue Forschungsmöglichkeiten, beispielsweise im Bereich von Materialtests unter extremen zentrifugalen Belastungen und liefern Erkenntnisse für die Entwicklung zukünftiger elektrischer Antriebssysteme im Höchstdrehzahlbereich.

Notation

Unless otherwise stated directly in the text, the following notation is used throughout this thesis.

Symbols - Latin

a	radius	m
a_r	centrifugal acceleration	m/s^2
A	area	m^2
A	magnetic vector potential	Vs/m
b	mechanical damping	Ns/m
B	magnetic flux density	T
c	speed	m/s
c_p	specific heat at constant pressure	J/(kgK)
c_v	specific heat at constant volume	J/(m^{3}K)
C_s	shape factor	
C	capacity	F
d	diameter	m
D	electric displacement	C/m^2
e	error	
E	Youngs's modulus (Chapter 2)	N/m^2
E	electric field	V/m
f	frequency	Hz
f	linearized force around operating point	N
F	force	N
h	height	m
H	magnetic field	A/m
i	current	A
I	current value	A
I	stress invariant (Chapter 2)	N/m^2
I	moment of inertia	kgm^2
J	current density	A/m^2
k	mechanical stiffness	N/m

k_f	thermal conductivity	W/(mK)
k_s	force/displacement constant	N/m
k_i	force/current constant	N/A
Kn	Knudsen number	
L	inductance	H
L	angular momentum (Chapter 2)	Nms
m	mass	kg
m	magnetic moment	Am^2
M	magnetization	A/m
M	molar mass (Chapter 4)	kg/mol
Ma	Mach number	
n	rotational speed	rpm
Nu	Nusselt number	
p	pressure	$\mathrm{N/m}^2$
p	power density (Chapter 4)	$\mathrm{W/m}^3$
P	power	W
P	transmission probability (Chapter 8)	
Pr	Prandtl number	
$\dot{Q}$	rate of heat flow	W
r	radius	m
R	resistance	Ω
R	magnetic reluctance (Chapter 5)	1/H
Re	Reynolds number	
t	time	s
T	torque	Nm
v	velocity	m/s
v	voltage	V
V	voltage value	V
V	volume	m^3
w	energy density	$\mathrm{J/m}^3$
W	energy	J
x, y, z	spatial directions	m

Symbols - Greek

α	displacement angle	$^\circ$
α_th	thermal accommodation coefficient	
γ	heat capacity ratio	
δ	shape ratio (Chapter 2)	

δ	skin depth (Chapter 4)	m
ϵ	permittivity	F/m
ϵ	strain (Chapter 2)	
ϵ	emissivity (Chapter 4)	
θ	polar angle	rad
ϑ	temperature	°C or K
λ	mean free path	m
μ	permeability	H/m
μ	dynamic viscosity	$\mathrm{Ns/m^2}$
ν	kinematic viscosity	$\mathrm{m^2/s}$
ν	Poisson's ratio (Chapter 2)	
ρ	electrical resistivity	Ωm
ρ	mass density	$\mathrm{kg/m^3}$
σ	mechanical stress (Chapter 2)	$\mathrm{N/m^2}$
σ_t	tangential-momentum accommodation coefficient (Chapter 4)	
σ	decay constant (Chapters 7 & 8)	1/s
σ	electrical conductivity	$\mathrm{S/m^2}$
τ	shear stress (Chapter 2)	$\mathrm{N/m^2}$
τ	time constant	s
φ	azimuthal angle	rad
Φ_m	magnetic scalar potential	Vs/m
Φ	magnetic flux	Wb
ω	angular frequency	rad/s

Subscripts

b	bearing
c	coil
c	compressive (Chapter 2)
c	continuum (Chapter 4)
Cu	copper
dc	direct current
drv	drive
ec	eddy current
el	electrical
ext	external
f	field
f	fluid (Chapter 4)

fm	free molecular (Chapter 4)
g	gravitational
in	internal
i	current
m	magnetic
m	motor
max	maximum
meas	measured value
mech	mechanical
min	minimum
PM	permanent magnet
r	radial
r	rotor
ref	reference value
r, φ, z	spatial directions in cylindrical coordinates
s	displacement
s	shape
sw	switching
t	tangential
t	tensile
v	von Mises
x, y, z	spatial directions in Cartesian coordinates

Constants

c	speed of light	3×10^8 m/s
g	gravitational acceleration	9.81 m/s^2
k_B	Boltzmann constant	1.381×10^{-23} J/K
N_A	Avogadro constant	6.022×10^{23} 1/mol
ϵ_0	vacuum permittivity	8.854×10^{-12} F/m
μ_0	vacuum permeability	$4\pi \times 10^{-7}$ H/m
σ_B	Stefan-Boltzmann constant	5.670×10^{-8} W/(m^{2}K^4)

Conventions and Operators

$\vec{B}$	vector
$f(\ldots)$	function of
d	differential operator
∂	partial derivative
∇	nabla operator

Abbreviations

2D	two-dimensional
3D	three-dimensional
ac	alternating current
ADC	analog-to-digital converter
AMB	active magnetic bearing
dc	direct current
DSP	digital signal processor
FEM	finite element method
FFT	fast Fourier transform
FPGA	field programmable gate array
fps	frames per second
iGSE	improved general Steinmetz equation
LED	light emitting diode
MSPS	megasamples per second
NIR	near infrared
ODE	ordinary differential equation
PC	personal computer
PCB	printed circuit board
PID	proportional-integral-derivative
PM	permanent magnet
PSD	position sensitive device
PWM	pulse-width modulation
rpm	revolutions per minute
SAM	spin angular momentum
UTS	ultimate tensile strength
VSM	vibrating sample magnetometer

Chapter 1

Introduction

1.1 Motivation and Objectives

Electric motors and generators are used in numerous fields today. Fueled by applications such as centrifuges, drive systems for turbo compressors, machining spindles, flywheels, and generators for microscale gas turbines, a trend toward miniaturization and increased power density of these machines has developed in recent years [1]. This trend is facilitated by motors featuring low torque and high rotational speeds [2]. Some applications, such as rotating mirror optical systems, directly demand high rotational speeds [3]. These developments sparked interest in the underlying physical limitations regarding the achievable rotational speed, independent of a specific application. Historically, significant efforts have been made to push the limits of the achievable rotational speeds. While the latter were generally limited to values below 100 000 revolutions per minute (rpm) until the 1920s [4], rapid developments facilitated a rotational speed of almost 38 million revolutions per minute (Mrpm) in a laboratory environment by 1947 [5]. However, such speeds could not be reproduced in subsequent attempts with similar setups [6, 7], despite several technological advancements. This resulted in the aforementioned speed having been considered the world record for the highest rotational speed achieved with an electrically driven rotor for almost 70 years.

The objective of this thesis is to reproduce and break the rotational speed record from 1947. For this purpose, the underlying physical boundaries are identified and concepts for expanding the applicability of electric machines to such ultra-high rotational speeds are presented. The theoretical background, design, and implementation of an electric motor capable of reaching 40 Mrpm are outlined in this work. The developed techno-

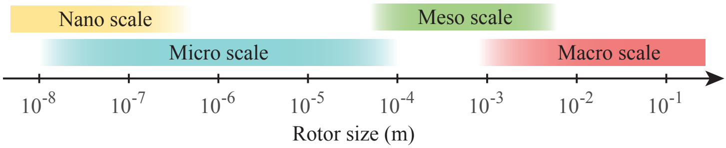

Figure 1.1: Definition of scales used for categorization of the surveyed systems.

logical solutions are aimed at providing insights for future generations of high-speed electrical drive systems.

1.2 History of Ultra-High-Speed Rotation

To put this work into historical context, a brief overview of achieved rotational speeds over time is provided in this section. The focus is placed on identifying the research works, laboratory setups, and technologies that facilitated high-speed rotation rather than on providing a comprehensive review. The surveyed systems are categorized chronologically and based on the scale of the employed rotor, for which a definition is provided in Fig. 1.1.

Macro- and Mesoscale Systems

Early works aimed at reaching high-speed rotation were fueled by the desire to generate high centrifugal accelerations in centrifuges for rapid sedimentation [8]. The centrifugal acceleration $a_c = \omega^2 r$, where ω denotes the angular frequency of rotation and r denotes the radius of the considered point, is directly linked to high rotational speeds. Centrifuges in which the rotor was suspended by ball bearings were used in laboratory experiments in the 1920s and reached rotational speeds in the range of 30 000 rpm [9]. By using oil lubricated journal bearings and an oil-turbine drive, the achievable rotational speed was increased to 160 000 rpm by the end of the 1930s [10].

Imbalances of the rotor and the associated forces that need to be carried by the employed bearings become increasingly problematic at high rotational speeds. Accordingly, contact-free suspension of the rotor by means of gas bearings was used in subsequent motor setups aimed at achieving high rotational speeds. The technique was proposed in [11], where a rotor of 11.7 mm in diameter was spun at 660 000 rpm. A rotational speed of 1.3 Mrpm, which was reached with a rotor of 9 mm in diameter suspended and driven by hydrogen, was reported in [4]. The achievable rotational speed employing such a suspension system is inherently limited by gas friction and the properties of the gas flow. Overcoming these limitations required the development of a technique that can be applied to rotors spinning in a vacuum.

The suspension of rotors by means of magnetic forces was initially proposed in 1937 at the University of Virginia [12] and the majority of subsequent developments took place at the same institution. Rotational speeds of up to 72 000 rpm were reached with a rotor suspended in vacuum at very low frictional torques during initial experiments [13]. By 1941, the attained rotational speed had successively been increased to 6.6 Mrpm, which was reached using a steel sphere of 2.38 mm in diameter as a rotor [14, 15]. In 1946, J. W. Beams et al. published the results of several acceleration experiments, during which a maximum rotational speed of 23.16 Mrpm was achieved with a 0.795 mm steel sphere shortly before mechanical failure of the rotor due to centrifugal loading occurred [16]. Extension of these results by the same researchers led to a rotational speed of 37.98 Mrpm, which was achieved with a 0.521 mm sphere [5]. In 1950, an experiment using a sphere with a diameter of 0.396 mm was published [17]. Because of the small size of the rotor, it was not possible to measure its rotational speed and the mechanical limit, which was estimated to be at 48 Mrpm, was not reached. Such high rotational speeds could not be reproduced in closely related experiments for more than six decades, despite significant technological advancements, especially in the field of the control electronics. In experiments published in 1979, the smallest levitated rotor had a diameter of 1.5 mm and reached a rotational speed of 12.64 Mrpm [6]. In 2005, a rotational speed of 2.88 Mrpm attained with a 1 mm sphere and limited by gas friction under medium vacuum conditions was published [7].

Micro- and Nanoscale Systems

Significant research effort has been invested to demonstrate high power densities in microelectromechanical systems (MEMS) by reaching high rotational speeds. In 2004, a MEMS electric induction motor was presented, in which a gas-bearing-supported 4 mm rotor reached 55 000 rpm [18]. The same bearing type was used in [19] to reach a rotational speed of 1.7 Mrpm using a micro air turbine. A rotational speed of 29 600 rpm was achieved using an electrostatic bearing in a variable-capacitance micromotor [20].

By further downscaling the rotor and using a quadrupole ion trap, graphene flakes with diameters of approximately 0.4 µm were levitated in [21]. By using circularly polarized light to drive the flake, a maximum rotational frequency, which was inferred from modulated light scattered off the rotating flake, in the range of 330 Mrpm (5.5 MHz) was obtained. In 2013, Arita et al. used simultaneous optical trapping and rotation of 4.4 µm spherical birefringent vaterite crystals in high vacuum to demonstrate a stable rotation rate of 5 MHz and 600 Mrpm (10 MHz) for short durations, before the particle disintegrated [22]. As of this writing, the latter value is listed by *Guinness World Records* as the “Highest man-made RPM” [23].

The recently evolved research area of nanoelectromechanical systems (NEMS) offers the potential for further downscaling of the rotor [24]. Nanowires with diameters of 150–400 nm and lengths of 800 nm–10 µm have been driven by various techniques and used as rotors in nanomotors. In [25], such a rotor was driven by an electric field to rotate around its transverse axis, reaching a rotational speed of $\sim$ 18 000 rpm. Driving rotors of similar size to rotate around their longitudinal axis by means of ultrasound led to rotational speeds in the range of 150 000 rpm [26] and using propulsion by rotating magnetic fields, precession at 1 kHz near a surface was demonstrated [27]. In [28] spherical gold nanoparticles with an average radius of 200 nm were trapped in water against a glass surface and accelerated to approximately 180 000 rpm (3 kHz) by a polarized laser beam. The achievable rotational speed was limited by the occurring drag torques and substantial heating of the particle due to absorption of the laser power. Driving smaller gold nanorods by resonant light scattering led to rotational speeds of up to 2.52 Mrpm (42 kHz) [29]; the speeds were limited by the same factors as in [28], due to the similarities of the employed techniques.

An overview of the aforementioned works based in their evolution is provided in Fig. 1.2. Furthermore, Fig. 1.3 provides an overview of the achieved rotational speeds depending on the rotor diameter and identifies the mechanical stress limit for mesoscale systems.

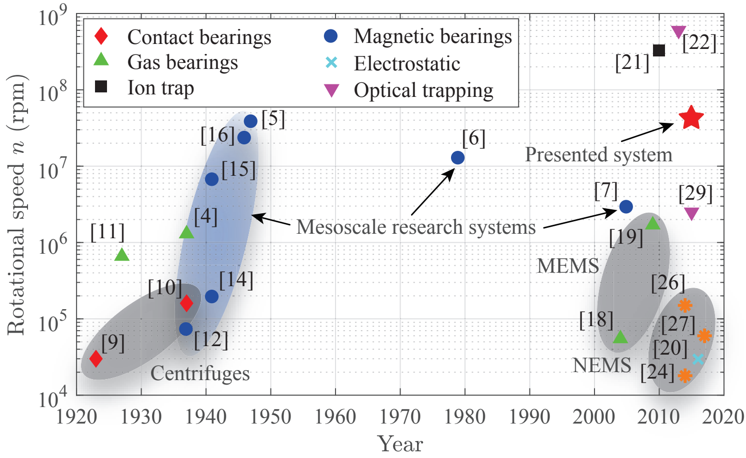

Figure 1.2: Historical development of ultra-high-speed rotation including the employed technologies and system scales. The system presented in this work is shown by the red star.

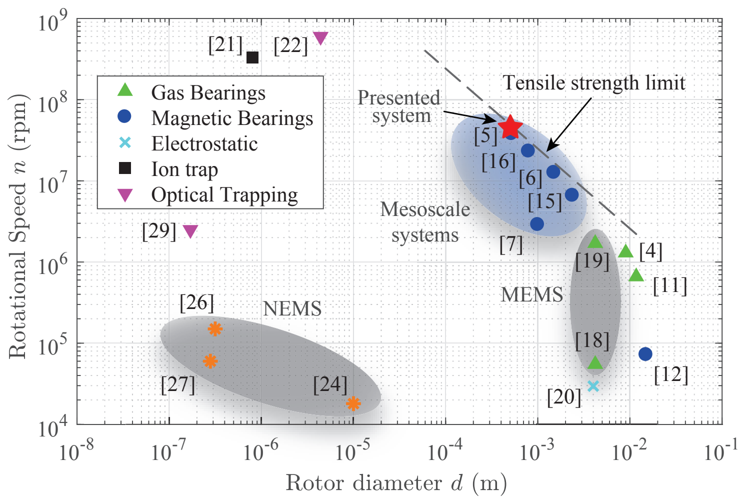

Figure 1.3: Achieved rotational speeds depending on the rotor diameter including the employed technologies and system scales. The system presented in this work is shown by the red star.

1.3 Potential Applications

Despite the goal of exploring the physical limitations of ultra-high-speed rotation independent of a specific application in this work, a short overview of potential target areas into which the findings could be transferred is provided here. High rotational speeds are directly linked to high losses and reduced reliability of conventional bearing technologies, such as ball and journal bearings. The magnetic bearing technology used in this work including the developed sensor systems and control schemes could beneficially be applied in fields where high rotational speeds are required, resulting in lower losses, increased reliability, and maintenance-free operation. The only remaining limit to the achievable rotational speeds is then imposed by the mechanical construction of the rotor.

Two main reasons for the use of ultra-high rotational speeds can be identified, namely the achievement of high power densities in small-scale drive systems and a direct requirement imposed by the desired application. Subsequently, both directions are briefly explored.

1.3.1 Small-Scale Drives

Miniaturization of electrical drive systems is usually linked to increased rotational speeds to provide a desired power level despite the low achievable torques. From scaling laws based on the principles of electromechanical energy conversion, it can be shown that high power densities are achieved for small-scale machines if the rotational speed can be increased sufficiently [2, 30]. An overview of such systems featuring both high power and high rotational speed, is provided in [1, 31–35]. Typical applications include turbo compressor systems, generators for microscale gas turbines, machining spindles, and flywheels. The rotational speeds of industrially available electrical drives are limited to below 500 000 rpm even for specialized systems to date and speeds of up to 1 Mrpm have been demonstrated in research setups. Figure 1.4 shows the trend toward ultra-high rotational speeds and its continuation, including exemplary fields of applications. The targeted rotational speed of this work has been added.

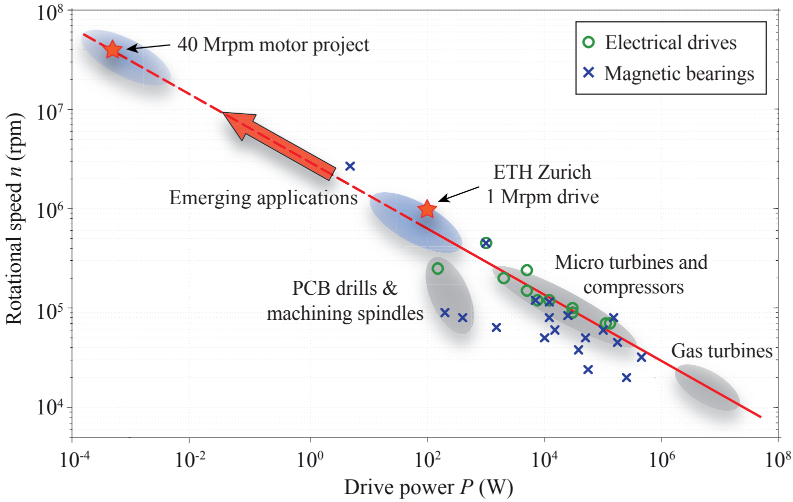

Figure 1.4: Trend toward ultra-high rotational speeds including exemplary application areas.

1.3.2 Optical Systems and Research Instruments

Several optical setups which are applied, e.g., in scanners, high-speed imaging, and laser systems feature rotating optical components that are used to alter the spatial or temporal behavior of a light beam [3]. This diverted beam is used to scan an area and the scanning speed of the system is limited by the rotational speed of the aforementioned optical components. In a high-speed camera capable of recording 25 million frames per second, a three-faced polygon mirror is rotated at speeds of up to 1.2 Mrpm by a helium gas turbine [36, 37]. The lifetime of this turbine is limited by the employed ball bearings and could be greatly enhanced by the application of a magnetic suspension technique such as presented in this work. Its high potential in optical systems was already outlined in [38], where a magnetically suspended mirror rotating at high rotational speeds was presented.

Ultra-high rotational speeds, such as achieved in this work, also open up new research possibilities for studying the behavior of materials under extreme centrifugal loads, e.g., in the field of materials science. Aside from investigating failure mechanisms in bursting experiments [39], studies of more complex phenomena, such as the strength and adhesion of thin films applied to the rotor, are possible [40]. Because of the use of mesoscale rotors, centrifugal accelerations of 10^8 times gravity can be achieved. This provides the basis for hypergravity experiments at much higher levels in the field of physics.

1.4 State of the Art

As systems of various sizes and power levels employing high rotational speeds have already been presented in the previous sections, the scope is limited to mesoscale systems and the achievement of highest rotational speeds here.

In 1946, an experimental setup for suspending small scale rotors in vacuum was presented in [16]. This setup, including an explanation of its components, is provided in Fig. 1.5. A magnetic suspension technique as initially proposed in [12] was used and the setup is a revised version of that used earlier in [15]. The rotor was actively suspended in the vertical direction by adjusting the current in a solenoid based on the position of the rotor. The latter was measured using a sensing coil that was placed below the rotor. Passive damping of the rotor in the horizontal direction was implemented by using a damping needle suspended in a fluid at its lower end and magnetically coupled to the rotor at the top. The rotor was accelerated by the principle of a solid rotor induction machine. The highest measured rotational speed attained with this or a similar setup was 37.98 Mrpm, which was initially published in 1947 [5]. An overview of the general research activities at the time is provided in [41].

A similar setup was used in a study published in 1979, which was aimed at developing a research instrument for the study of nuclear atomic phenomena, which requires the generation of ultra-high centrifugal fields [6]. The highest measured rotational speed in this study was 12.64 Mrpm.

The experiments of [16] were revived in 2002, where a setup with a ferrite magnetic circuit on the stator side was used [42, 43]. The highest achieved rotational speed was 2.88 Mrpm, which was limited by gas friction [7].

In summary, the highest measured rotational speeds of electrically

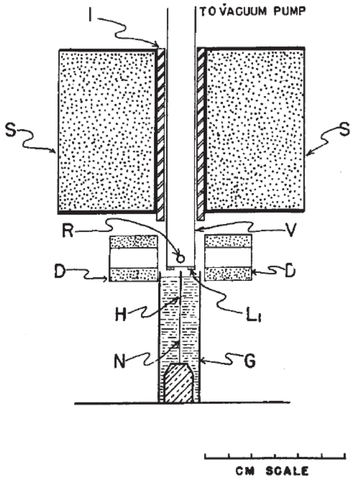

Symbol	Explanation
R	rotor
S	solenoid
D	drive coils
L_1	sensing coil
I	iron tube
H	iron wire
G	glass tube
V	glass chamber
N	damping needle

Figure 1.5: Cross-sectional view of the experimental setup used in [16].

driven rotors, which constitute the basis for this work, were already achieved in the 1940s and were not reproduced or exceeded in the meantime, despite subsequent attempts.

1.5 Challenges

The design and implementation of an electric motor that is capable of accelerating a rotor to speeds of several tens of million rpm and achieve the highest measured rotational speed of an electrically driven rotor involve several challenges:

- A rotor that is mechanically capable of reaching the desired ultra-high rotational speeds has to be selected. Its diameter has to be in the submillimeter range to limit the occurring mechanical stresses and a material featuring high specific strength has to be used. Moreover, low tolerances to prevent rotor imbalances and the dynamic stability of rotation around the desired axis have to be guaranteed.
- The employed suspension system for the rotor needs to feature extremely low friction as high power loss would otherwise result and

prevent the achievement of ultra-high rotational speeds. To reduce gas friction drag, a suspension technique that can be employed in vacuum has to be developed and applied. The absence of sufficient natural damping requires active stabilization of the rotor in all translatory degrees of freedom (DOF). Successful application of a magnetic suspension technique requires knowledge of the magnetic material properties of the rotors, which is not commonly available.

- A suitable drive system that is capable of accelerating the rotor without mechanical contact and through the wall of a vacuum chamber needs to be developed. Comprehensive knowledge of the entailed losses in the rotor, occurring drag torques due to gas friction, heat transfer mechanisms between the rotor and its environment, and the resulting rotor temperature is necessary. The latter has to be limited such that mechanical stability of the rotor can be guaranteed.
- A machine stator featuring low electromagnetic losses at field frequencies in the megahertz range is required. As this exceeds the frequencies occurring in common electric machines by far, a significantly different design needs to be developed.
- A sensor system for accurately measuring the position of the submillimeter size rotor in all dimensions is required. This system has to be capable of measuring without contact from a distance of several millimeters (more than 10 times the rotor diameter) through the wall of the vacuum chamber. Moreover, it must be free of interference with the magnetic bearing and drive systems. In addition, a sensor system with a bandwidth of several hundreds of kilohertz for reliable measurement of the rotational speed needs to be developed.
- Power electronic converters capable of the combined generation of drive currents in the megahertz range and currents for magnetic suspension of the rotor need to be developed. A corresponding control system featuring high linearity, accuracy, and speed is necessary for successful stabilization of the rotor due to its low inertia.
- The design and integration of the overall motor system have to feature very low tolerances and precise placement of all necessary components closely around the rotor is challenging due to the confined space. The integration of a well-sealed vacuum system and decoupling of vibrations originating from the employed pumps are

Table 1.1: Physical properties of a rotor spinning at 40 Mrpm

Parameter	Symbol	Value	Unit
Rotor sphere radius	a	0.25	mm
Density of rotor material	ρ_{r}	7610	kg/m^3
Rotational speed	n	40 000 000	rpm
Rotational frequency	f	666.67	kHz
Sphere volume	V	0.065	mm^3
Rotor mass	m	0.50	mg
Moment of inertia	I	1.25×10^{-14}	kg·m^2
Rotational Energy	W	0.11	J
Circumferential speed	v	1047 (3770)	m/s (km/h)
Centrifugal acceleration	a_r	4.4×10^9 (4.5×10^8)	m/s^2 (g)

necessary for successful operation of a practical experimental setup. Suitable procedures for handling and preparation of rotors down to 0.5 mm in size are required to achieve repeatable experimental conditions for obtaining quantitative statistical results.

To illustrate some of the aforementioned challenges, Table 1.1 provides an overview of characteristic physical quantities for a spherical rotor of 0.5 mm in diameter spinning around an axis through its center of mass at 40 Mrpm.

1.6 Outline of the Thesis

The goal of this thesis is to achieve a new record for the highest measured rotational speed of an electrically driven rotor. This requires exceeding a rotational speed of 37.98 Mrpm which was already published in 1947 and has not been reproduced afterward. For this purpose, the design and implementation of an electric motor that is capable of reaching such ultra-high rotational speeds are presented. Based on an identification of the physical boundaries, concepts for expanding the applicability of electric machines to this speed range are developed and implemented.

After this introduction, the process for selecting a suitable rotor based on its magnetic and mechanical properties is outlined in Chapter 2. The chapter also provides measured results for the magnetic properties of spherical steel rotors, which are relevant for the suspension of these rotors.

In Chapter 3, the concept of magnetic suspension at low friction losses is introduced and analyzed in detail. The selection of a suitable topology for active stabilization of the rotor in all DOF is outlined alongside an analytical calculation of the magnetic suspension forces. Furthermore, the design and optimization of a magnetic actuator for suspending the rotor against the gravitational force which integrates a vacuum system is presented.

Chapter 4 provides models for the occurring drive torque and rotor losses based on analytical solutions for the underlying field problem of a spherical rotor spinning in a rotating magnetic field. In conjunction with analytical mathematical descriptions of the windage losses and heat transfer rates between the rotor and its environment in various gas flow regimes, a thermal model of the rotor is derived. The latter provides the basis for assessing admissible operating conditions under which ultra-high rotational speeds can be achieved.

Suitable stator topologies for generating rotating magnetic fields in the megahertz range at low high–frequency losses are presented in Chapter 5. Designs employing power ferrite materials for guiding the magnetic flux toward the rotor are outlined, for which the achievable acceleration rates are only restricted by the thermal limit of the rotor.

Chapter 6 presents optical sensor systems for measuring the rotor position in all DOF as well as its rotational speed without contact through the wall of a vacuum chamber. The system has a bandwidth of several hundreds of kilohertz. Both sensor systems operate from a distance equivalent to a multiple of the rotor diameter, due to the limited available space in the vicinity of the rotor.

The power electronic converter system required for generating the high frequency drive currents as well as the currents necessary for magnetic stabilization of the rotor is presented in Chapter 7. The same chapter details the employed control structures and their implementation on a system consisting of a combination of a digital signal processor (DSP) and a field programmable gate array (FPGA).

Chapter 8 describes the developed and implemented setup of the ultra-high-speed motor. Results regarding the performance of the developed magnetic bearing systems are provided and the models of Chapter 4 are verified experimentally. Exemplary acceleration curves derived from a series of run-up experiments during which approximately 50 rotors of different sizes and materials were accelerated to their bursting speeds are provided. A quantitative statistical analysis of the achieved rotational speeds is carried out alongside a comparison to the failure models introduced in Chapter 2. The failure mechanism of the rotors is investigated using high-speed-image recordings of the rotor explosion and a subsequent microscopic analysis of the rotor fragments. Measured results for an acceleration experiment during which a rotational speed slightly above 40 Mrpm was reached are provided.

Chapter 9 concludes the thesis and provides an outlook on future work.

1.7 Scientific Contributions

The following list summarizes the main contributions presented in this thesis.

- In [C1] and [J1], the assessment of suitable rotor materials with an emphasis on their magnetic properties is presented. Measured results for the magnetization curves of steel spheres subsequently used as rotors are provided which were previously unavailable in the literature.
- [C6] presents magnetic actuators for active stabilization of the rotor in all DOF alongside the required position sensors. Such a suspension system is a prerequisite for achieving ultra-high rotational speeds as previously employed passive damping of the rotor in the horizontal direction cannot reliably be applied due to the small rotor sizes required in this work.
- A feasibility analysis for passive stabilization of the rotor by means of an electrodynamic bearing, which does not require the rotor to be ferromagnetic and can, therefore, be applied to a wide variety of materials, is provided in [C2].
- In [C3], various stator designs suitable for drive field frequencies in the megahertz range are demonstrated. Designs employing ferrite core materials to increase the magnetic flux density at the rotor facilitate acceleration rates of the rotor up to its thermal limit, which

had not been attained previously. This facilitates the conduction of rapid and repeatable acceleration experiments.

- [C4] presents an analysis of the interaction between the drive system and active magnetic suspension of the rotor in the horizontal direction as outlined in [C6]. Guidelines for choosing the magnitudes of the respective flux density are provided, such that the decelerating torque generated by the suspension system does not impair the acceleration of the rotor.
- The occurring rotor losses due to the drive system and a thermal model of the rotor are studied in [C5]. Based on the provided findings, the operating conditions of the motor can be chosen such that a critical rotor temperature is not exceeded and the material retains its full mechanical strength to reach ultra-high rotational speeds.
- In [J3], an overview of historical and recent developments in the field of ultra-high-speed rotation is presented, followed by a summary of the magnetic suspension technique used for the submillimeter-size rotors. The motor torque and drag torques are analyzed alongside the entailed losses and resulting rotor temperature. A detailed quantitative statistical analysis of the achieved rotational speeds in ~ 50 acceleration experiments, which were carried out using various rotor sizes and materials, is provided. During these experiments, a rotational speed slightly above 40 Mrpm was reached. An assessment of the rotor failure mechanisms is provided based on high-speed recordings of rotor explosions and subsequent microscopic analyses of the fragments.

1.8 List of Publications

Parts of this work have been published or are being considered for publication in international journals or conference proceedings. These publications are listed below.

The publications [J2] and [C7] present works in the areas of electric machines and magnetic bearings which were conducted during the research period at the Power Electronics Systems Laboratory and are not directly related to this project.

Journal Papers

[J1] M. Schuck, T. Nussbaumer, and J. W. Kolar, "Characterization of Electromagnetic Rotor Material Properties and their Impact on an Ultra-High Speed Spinning Ball Motor," *IEEE Transactions on Magnetics*, vol. 52, no. 7, July 2016.

[J2] P. Puentener, M. Schuck, D. Steinert, T. Nussbaumer, and J. W. Kolar, "A 150 000rpm Bearingless Slice Motor," *IEEE/ASME Transactions on Mechatronics*, under review.

[J3] M. Schuck, D. Steinert, T. Nussbaumer, and J. W. Kolar, "Ultra-Fast Rotation of Magnetically Levitated Macroscopic Steel Spheres," *AAAS Science Advances*, vol. 4, no. 1, January 2018.

Conference Papers

[C1] M. Schuck, T. Nussbaumer, and J. W. Kolar, "Electromagnetic Suitability Analysis and Characterization of Ultra-High Speed Spherical Steel Rotors," *13th Joint Magnetism and Magnetic Materials Conference (INTERMAG 2016)*, San Diego, CA, USA, January 2016.

[C2] M. Schuck, J. Schäfer, T. Nussbaumer, and J. W. Kolar, "Analysis and Design of a Passive Electrodynamic Bearing for an Ultra-High Speed Spinning Ball Motor," *Advances in Magnetics Conference (AIM 2016)*, Bormio, Italy, March 2016.

[C3] M. Schuck, J. Schäfer, D. Steinert, and J. W. Kolar, "Improved Stator Design for an Ultra-High Speed Spinning Ball Motor," *International Symposium on Power Electronics, Electrical Drives, Automation and Motion (SPEEDAM 2016)*, Anacapri, Italy, June 2016.

[C4] M. Schuck, D. Steinert, and J. W. Kolar, "Torque Interaction of the Drive and Active Radial Magnetic Bearing in an Ultra-High Speed Spinning Ball Motor," *International Symposium on Magnetic Bearings (ISMB15)*, Kitakyushu, Japan, August 2016.

[C5] M. Schuck, D. Steinert, and J. W. Kolar, "Rotor Losses in an Ultra-High Speed Spinning Ball Motor," *International Conference on Electrical Machines (ICEM 2016)*, Lausanne, Switzerland, September 2016.

[C6] M. Schuck, D. Steinert, and J. W. Kolar, “Active Radial Magnetic Bearing for an Ultra-High Speed Motor,” *European Conference on Power Electronics and Applications (ECCE Europe 2016)*, Karlsruhe, Germany, September 2016.

[C7] M. Schuck, A. Da Silva Fernandes, D. Steinert, and J. W. Kolar, “A High Speed Millimeter-Scale Slotless Bearingless Slice Motor,” *IEEE International Electric Machines & Drives Conference (IEMDC 2017)*, Miami, FL, USA, May 2017.

Chapter 2

Rotor Selection

The achievable rotational speed of an electric machine is usually limited by the occurring drag torques, which are generated, e.g., by friction in the employed bearings, eddy currents, and air friction. Consequently, the achievable rotational speed is constricted by thermal limitations. If the aforementioned losses can be made sufficiently small, the achievable rotational speed is ultimately limited by the centrifugal stress occurring in the rotor and the capability of the rotor material to withstand this stress.

To provide an understanding of the requirements for rotors being mechanically capable of reaching rotational speeds of several tens of millions of rpm, this chapter provides an overview of mechanical failure mechanisms. Suitable materials are assessed based on their capability to withstand high centrifugal stress and guidelines for selecting a suitable rotor shape are provided based on the dynamic rotational stability.

As the suspension and driving techniques applicable to the rotor depend on its material and shape, the rotor selection is a prerequisite for the analyses of subsequent chapters.

2.1 Mechanical Limit

The maximum mechanical stress σ_{max} inside a spinning rotor occurs along the axis of rotation and can be calculated as

$$\sigma_{\mathrm{max}} = C_{\mathrm{s}} \rho_{\mathrm{r}} \omega_{\mathrm{r}}^2 a^2, \tag{2.1}$$

where ρ_r, ω_r, and a denote the density of the rotor material, its angular rotational frequency, and the rotor radius, respectively. The factor C_s is used to account for the influence of the rotor shape on σ_max. The rotor material needs to be capable of withstanding this stress, as rotor failure would occur otherwise. The maximum stress a certain material can withstand is characterized by the ultimate tensile strength for ductile materials and the yield strength for brittle materials.

The rotational speed limit for a given rotor material and shape can be expressed by the achievable circumferential speed as

$$v_\mathrm{max} = \omega_\mathrm{max} a = \sqrt{\frac{1}{C_\mathrm{s}} \frac{\sigma_\mathrm{max}}{\rho_\mathrm{r}}}, \tag{2.2}$$

which is independent of the rotor diameter. This shows that the achievable rotational speed is governed by the relation

$$n_\mathrm{max} \propto \frac{1}{a}. \tag{2.3}$$

This limit can also be observed when analyzing the achieved rotational speeds of previous mesoscale systems, for which an overview is provided in Fig. 2.1. These systems used steel spheres as rotors for which the diameters have to be well below 1 mm to attain the desired rotational speeds. To achieve high rotational speeds for a given radius, the rotor should consist of a material that has a high strength to density ratio and is shaped to yield a small value of C_s. These two properties are analyzed subsequently.

2.1.1 Stress-Strain Curve

The maximum stress that a given isotropic material is able to withstand before fracturing is commonly determined by recording the occurring stress σ dependent on the strain ϵ during a tension test with applied uniaxial force F using a macroscopic specimen [44]. An exemplary stress-strain curve typical of steel is shown in Fig. 2.2(a). Initially, a linear elastic relation between the applied strain and the resulting stress in the material can be observed, where the stress-strain relationship is described

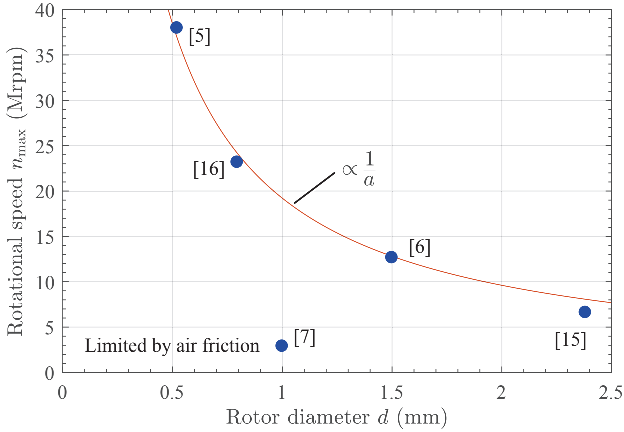

Figure 2.1: Overview of achieved maximum rotational speeds for mesoscale systems employing spherical steel rotors.

by the modulus of elasticity (Young's modulus) as

$$E = \frac{\sigma}{\epsilon} = \text{const} \tag{2.4}$$

up to the proportional limit stress. The elastic behavior often extends into a non-linear region up to the yield strength. Beyond this point, deformations are plastic and the specimen does not return to its original shape and size upon removal of the load. Strain hardening occurs in ductile materials, during which the stress and strain increase further. Plastic flow leads to a decrease of the cross-sectional area of the sample, which is referred to as necking. To assess the transverse strain ϵ_{t} (contraction) that occurs due to the axial strain ϵ (expansion) in the direction of the applied force, the Poisson's ratio defined as

$$\nu = -\frac{\mathrm{d}\epsilon_{\mathrm{t}}}{\mathrm{d}\epsilon} \tag{2.5}$$

is used. For the considered steels $\nu \approx 0.3$ holds and was used for the subsequent considerations unless otherwise noted. As the original cross-sectional area A_0 of the sample is commonly used in the engineering sciences, the apparent stress (F/A_0) decreases in a sufficiently ductile

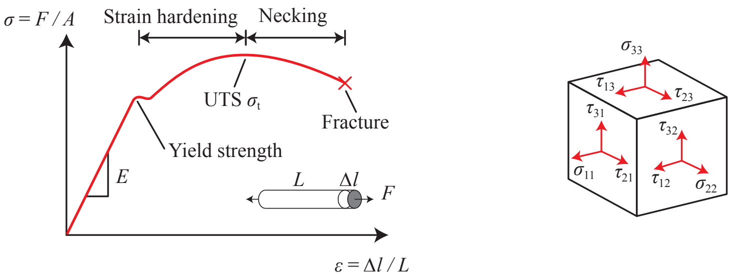

(a) (b)

Figure 2.2: (a) Qualitative stress-strain curve typical of steel including characteristic values and regions. (b) Cauchy stress tensor describing a general multiaxial state of stress.

material, where necking becomes substantial. However, the actual stress F/A in the material increases further, as A is decreased. The reversal point on the stress-strain curve used in engineering is the maximum stress that occurs in this curve and is referred to as the ultimate tensile strength (UTS).

Brittle materials, such as cast iron, carbon fiber, and ceramics, rupture without noticeable prior deformation. Failure occurs during linear elastic deformation.

For the considered uniaxial state of stress, the conditions under which fracture of the specimen occurs are directly obtained from the measurements. Tabulated values for the mechanical characteristics of materials are usually obtained from such tests.

2.1.2 Failure Criteria

Rotation leads to a centrifugal force acting on the rotor. This results in a multiaxial state of the mechanical stress inside the rotor material. Consequently, the state of stress at a point inside the rotor is expressed as a second-order tensor (Cauchy stress tensor). This is illustrated in Fig. 2.2(b), where all stress components that can occur on the faces of an elemental volume are shown. These components consist of normal stresses σ directed perpendicular to the faces of the cube and shear stresses τ that are parallel to the faces of the cube. The subscripts 1, 2, and 3 denote the unity vector directions of the employed coordinate system.

To obtain an estimate of the achievable rotational speed for a given rotor material, the multiaxial state of stress has to be compared to material properties obtained by uniaxial tensile testing. For this purpose, several combined stress theories exist in the literature that provide different measures based on which material failure is predicted [45]. Usually, a specific combination of the components from the general state of stress is used to provide a single stress value that can be compared to the uniaxial case.

An overview of commonly used failure criteria relevant for the materials considered in this work is provided below. For these criteria to be applicable, the rotor materials are assumed to be isotropic.

Maximum Normal Stress Theory (Rankine's Theory)

Failure in the multiaxial state of stress is predicted if any of the maximum principal normal stresses is equal to or exceeds the maximum normal stress at which failure occurs in an uniaxial test for the same material. Principal normal stresses occur on planes where the shear stresses are zero. For any given point inside the material, the principal normal stresses represent local extrema. Derivation of the principal stresses based on the corresponding principal planes yields the so-called general stress cubic equation

$$\sigma^3 - I_1\sigma^2 + I_2\sigma - I_3 = 0, \tag{2.6}$$

of which the principal normal stresses are the solutions. Here, I_1, I_2, and I_3 are referred to as stress invariants and are given by

$$I_1 = \sigma_{11} + \sigma_{22} + \sigma_{33} \tag{2.7}$$

$$I_2 = \sigma_{11}\sigma_{22} + \sigma_{22}\sigma_{33} + \sigma_{33}\sigma_{11} - \tau_{12}^2 - \tau_{23}^2 - \tau_{31}^2 \tag{2.8}$$

$$I_3 = \sigma_{11}\sigma_{22}\sigma_{33} + 2\tau_{12}\tau_{23}\tau_{31} + \sigma_{11}\tau_{23}^2 - \sigma_{22}\tau_{31}^2 - \sigma_{33}\tau_{12}^2. \tag{2.9}$$

The principal normal stresses σ_1, σ_2, and σ_3 correspond to the highest, lowest, and intermediate absolute value of the solutions to (2.6), respectively.

As the strength of the considered material might be different for tensile and compressive loading, the theory predicts failure if any of the following conditions is fulfilled for tensile loading

$$\sigma_1 \geq \sigma_\mathrm{t} \qquad \sigma_2 \geq \sigma_\mathrm{t} \qquad \sigma_3 \geq \sigma_\mathrm{t} \tag{2.10}$$

or

$$\sigma_1 \leq \sigma_\mathrm{c} \qquad \sigma_2 \leq \sigma_\mathrm{c} \qquad \sigma_3 \leq \sigma_\mathrm{c} \tag{2.11}$$

for compressive loading, where σ_t and σ_c denote the maximum tensile strength and compressive strength of the material for the uniaxial state of stress, respectively. This failure theory provides good estimates for materials that fail by brittle fracture, such as ceramics, cast iron, and some martensitic steels. For ductile materials, a theory based on the distortion energy inside the material is more suitable.

Distortion Energy Theory (von Mises Theory)

Rather than directly using the state of stress as a measure, this theory uses the distortion energy per unit volume inside the material. It predicts failure if the value of this energy in the multiaxial state of stress equals or exceeds that at which failure occurred for the same material in the uniaxial test. The theory was developed as an improvement to the total strain energy theory. It is based on the postulate that the total strain energy can be divided into two parts, namely the dilatation energy and the distortion energy. The former is associated solely with a change in volume. Contrarily, the distortion energy is associated only with a change in shape. It is assumed that failure in materials with ductile behavior is exclusively related to the distortion energy. A detailed derivation is provided in [45]. The von Mises stress is a measure for the distortion energy per unit volume in the multiaxial state of stress and is given in terms of the principal normal stresses as

$$\sigma_v = \sqrt{\frac{1}{2}\left[(\sigma_1 - \sigma_2)^2 + (\sigma_2 - \sigma_3)^2 + (\sigma_3 - \sigma_1)^2\right]}. \tag{2.12}$$

Failure is predicted if

$$\sigma_v^2 \geq \sigma_\mathrm{t}^2. \tag{2.13}$$

This theory was found to yield results that are in good agreement with experimental data for ductile materials, such as structural steel. Despite its derivation for the elastic range, an extension to the plastic range has been found to be valid.

2.2 Rotational Stability

Aside from the mechanical stability of the rotor, which is necessary for it to withstand high centrifugal forces, the rotor also has to be dynamically stable with regard to rotation around the desired axis. An arbitrary body features three distinct moments of inertia in the directions of its principal axes, referred to as principal moments I_1, I_2, and I_3. For the considered rotors with homogeneous density, the principal axes coincide with the axes of symmetry. The components of the angular momentum of a rotor about its center of rotation are governed by Euler's rotation equations. If the rotor is freely suspended without external torques acting on it, the magnitude of its angular momentum vector $\vec{L}$ has to be constant, while the direction of this vector may change. In addition, the kinetic energy has to remain constant. With the angular frequencies of rotation ω_1, ω_2, and ω_3 around the respective axes, this yields the two conditions

$$L^2 = I_1^2\omega_1^2 + I_2^2\omega_2^2 + I_3^2\omega_3^2 = \text{const} \tag{2.14}$$

$$W = \frac{1}{2}\left(I_1\omega_1^2 + I_2\omega_2^2 + I_3\omega_3^2\right) = \text{const}, \tag{2.15}$$

where (2.14) describes an angular momentum sphere and (2.15) represents an energy ellipsoid. During rotation of the body, the tip of the angular velocity vector has to inscribe a curve that represents the intersection of the sphere with the ellipsoid.

Rotational stability can be assessed by studying small perturbations of the axis of rotation. Such disturbances commonly occur in practical systems, e.g., through small imbalances. For a body with three distinct moments of inertia, it is found that rotations about the principal axes with the smallest and largest moments of inertia are stable, while rotation about the principal axis with the intermediate moment is unstable (exponential growth of small disturbances) [46]. For a body with a symmetry axis, $I_1 = I_2 \neq I_3$ holds, where I_3 is associated with the axis of symmetry. Rotation is only stable around the distinct axis of symmetry, while rotations about the other two principal axes are found to be (marginally) unstable. If $I_1 = I_2 = I_3$ holds exactly, no axis of rotation is stable. However, this exact case is usually not encountered in practice due to small asymmetries or material density variations.

Up to this point, it was assumed that energy is conserved. However, energy can be dissipated in practical systems by friction and other loss mechanisms. The only possibility for the rotational energy to decrease while maintaining the magnitude of $\vec{L}$ is to change the spin axis to one with a larger moment of inertia. For a rotor with $I_1 < I_2 < I_3$, initially spinning around the principal axis 1, the kinetic energy is given as $W = \frac{1}{2}L_1^2/I_1$. By changing its orientation to the principal axis 3, the energy is decreased to $W = \frac{1}{2}L_1^2/I_3$, as $I_3 > I_1$. Consequently, in practical systems where energy dissipation occurs, only rotation about the principal axis with the largest moment of inertia is permanently stable. This has been observed in [15], where rotors were bent and destroyed as they became rotationally unstable about their initial axis of rotation that featured a moment of inertia different from the maximum one. Therefore, the shape of the rotor needs to be chosen accordingly to prevent its premature failure before the mechanical strength limit is reached.

2.3 Material Selection

The actual density and tensile strength of a rotor depend on a variety of factors, such as the raw material, the use of additives, forming/sintering processes, heat treatment, and finishing techniques. To provide meaningful data for selecting a suitable rotor material, the relevant characteristic values were obtained from datasheets of small spheres in the millimeter and submillimeter range, which are commonly used in ball bearings. The results were used to calculate the strength to density ratio, referred to as the specific strength, which is shown in Figure 2.3. The listed steels exhibit the highest specific strength and are, therefore, most suitable for attaining high rotational speeds before mechanical failure occurs. Typical ceramics as employed in ceramic ball bearings exhibit very high compressive strengths. However, their tensile strength is significantly below that of steel due to their brittleness. Plastics feature a comparably low density, but their tensile strength is also much lower.

Several (fiber) composites exist that have much higher specific strengths

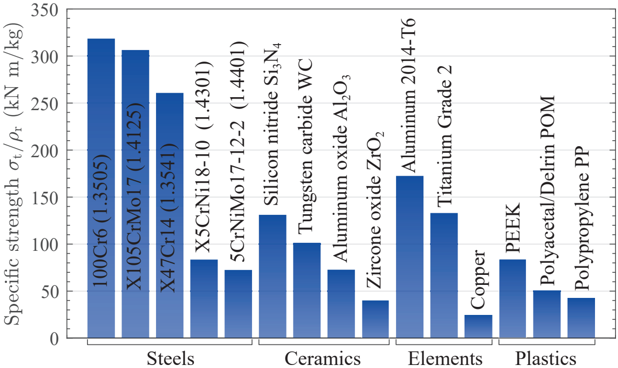

Figure 2.3: Specific strength of various materials.

than the listed materials, where the exact values depend on the used composition and manufacturing method. Due to the longitudinal shape of the raw material and the resulting anisotropy when processed into the desired shape, it is currently not easily possible to manufacture precise and well-balanced rotors, especially in the desired submillimeter-size range. Carbon-based atom structures, such as graphene, carbon nanotubes, and fullerenes, offer significantly higher specific strengths than conventional bulk materials. In fact, monolayer graphene has been tested to be the strongest material to date [47]. The three-dimensional assembly of such structures to form larger-scale objects is not yet easily possible and the attainable mechanical performance is significantly below that on the nanoscale [48]. For these reasons, neither fiber composites nor carbon-based atom structures are currently suitable as rotor materials for achieving ultra-high rotational speeds using a mesoscale system. However, especially carbon-based materials would offer the possibility to increase the achievable rotational speeds significantly if suitable synthesis methods become available in the future.

2.4 Stress Distributions and Moments of Inertia

To apply the failure criteria stated in Section 2.1.2, it is necessary to obtain the state of stress throughout the rotor that is caused by the centrifugal force. The absolute value of this stress depends on ρ_r, ν, as well as the shape and size of the rotor. The subsequent considerations will be used to determine rotor shapes that yield low mechanical stress for a given material and size. For this purpose, solutions for the stress distribution of different rotor shapes, namely thin disks, long cylinders, and ellipsoids, including detailed treatment of the particular case of a sphere, are provided. In the subsequent calculations, the rotor material is treated as homogeneous, isotropic, and elastic. The rotor is assumed to spin at constant angular frequency ω_r around the z axis. The corresponding field of the centrifugal body force is then given as $\rho_\mathrm{r}\omega_\mathrm{r}^2(x\vec{e}_x + y\vec{e}_y)$ or $\rho_\mathrm{r}\omega_\mathrm{r}^2 r\vec{e}_r$ in cylindrical coordinates. The rotational stability around this axis is assessed by means of the respective moment of inertia.

2.4.1 Thin Disk

A three-dimensional analytical solution for the stress distribution in a rotating solid disk with diameter a and height $h << a$ rotating about its symmetry axis is outlined in [49]. The stresses along the axes of a cylindrical coordinate systen are obtained to be

$$\sigma_r = \rho_\mathrm{r}\omega_\mathrm{r}^2\left[\frac{3+\nu}{8}(a^2-r^2) + \frac{\nu(1+\nu)}{6(1-\nu)}\left(\frac{h^2}{4} - 3z^2\right)\right] \tag{2.16}$$

$$\sigma_\varphi = \rho_\mathrm{r}\omega_\mathrm{r}^2\left[\frac{3+\nu}{8}a^2 - \frac{1+3\nu}{8}r^2 + \frac{\nu(1+\nu)}{6(1-\nu)}\left(\frac{h^2}{4} - 3z^2\right)\right] \tag{2.17}$$

$$\sigma_z = 0. \tag{2.18}$$

By letting $h \to 0$, the two-dimensional solution commonly used in the literature is obtained [50]. This shows that the occurring mechanical stress can be divided into two parts, namely the radial stress and the hoop stress, which represent principal normal stresses. Both stresses attain their maximum values, which are equal, at the center of the disk

$(r = z = 0)$

$$\sigma_1 = \sigma_v = \frac{3+\nu}{8}\rho_\mathrm{r}\omega_\mathrm{r}^2 a^2. \tag{2.19}$$

It can be shown that by introducing a hole of diameter b at the center of the disk and letting $b \to 0$ (pin hole), the maximum circumferential stress is doubled, while the radial stress remains the same. This stress concentration makes such rotor shapes unsuitable for ultra-high-speed rotation, as the lack of material at locations where the occurring stress would be maximum in a solid rotor significantly lowers the mechanical stability of the rotor.

For a solid disk or cylinder rotating about its symmetry axis, the moment of inertia is given as

$$I_\mathrm{s} = \frac{1}{2}ma^2 = \frac{1}{2}\rho_\mathrm{r}\pi a^4 h. \tag{2.20}$$

For rotation around its transverse axis

$$I_\mathrm{t} = \frac{1}{4}ma^2 + \frac{1}{12}mh = \rho_\mathrm{r}\pi a^2 h\left(\frac{a^2}{4} + \frac{h^2}{12}\right) \tag{2.21}$$

holds. From the rotational stability requirement $I_\mathrm{s} > I_\mathrm{t}$, it immediately follows that

$$h < \sqrt{3}a, \tag{2.22}$$

which is fulfilled for a disk.

2.4.2 Long Cylinder

A solution for the stresses in an elastic solid cylinder with free ends and $h >> a$ rotating about its symmetry axis is obtained as

$$\sigma_r = \rho_\mathrm{r}\omega_\mathrm{r}^2 \frac{3-2\nu}{8(1-\nu)}(a^2 - r^2) \tag{2.23}$$

$$\sigma_\varphi = \rho_\mathrm{r}\omega_\mathrm{r}^2 \frac{1}{8(1-\nu)}\left[(3-2\nu)a^2 - (1+2\nu)r^2\right] \tag{2.24}$$

$$\sigma_z = \frac{\nu}{4(1-\nu)}\rho_\mathrm{r}\omega_\mathrm{r}^2(a^2 - 2r^2). \tag{2.25}$$

The results are similar to that of a solid disk with the maximum stresses occurring at the center of the rotor ($r = 0$), yielding

$$\sigma_1 = \frac{3 - 2\nu}{8(1 - \nu)} \rho_\mathrm{r} \omega_\mathrm{r}^2 a^2 \tag{2.26}$$

and

$$\sigma_v = \frac{3 - 4\nu}{8(1 - \nu)} \rho_\mathrm{r} \omega_\mathrm{r}^2 a^2. \tag{2.27}$$

While the occurring von Mises stress is lower than that for a disk, rotational stability around the longitudinal axis by the criterion of (2.22) is not attained. Consequently, a long cylindrical rotor is unsuitable for reaching ultra-high rotational speeds, as it will change its axis of rotation or bend before the mechanical stress limit is reached [15, 33, 34].

2.4.3 Ellipsoid

The stress distribution in a rotating ellipsoid has been studied in [51] and [52]. The ellipsoid is described in Cartesian coordinates by its standard form

$$\frac{x^2}{r_x^2} + \frac{y^2}{r_y^2} + \frac{z^2}{r_z^2} = 1 \quad \text{with} \quad r_y \leq r_x, \tag{2.28}$$

where r_x, r_y, r_z describe the radii in the respective directions. The ellipsoid is assumed to rotate about the z axis. For the general case of $r_x \neq r_y \neq r_z$, it is cumbersome to obtain a closed-form analytic expression for the stress distribution [53]. Therefore, a semi-analytical approach with numerically computed scaling constants is used here. It can be shown that the occurring stresses due to rotation are of the form

$$\sigma_x = \sigma_0 \left[K_{1x} \left(1 - \frac{x^2}{r_x^2} \right) - K_{2x} \frac{y^2}{r_y^2} - K_{3x} \frac{z^2}{r_z^2} \right] \tag{2.29}$$

$$\sigma_y = \sigma_0 \left[K_{1y} \left(1 - \frac{y^2}{r_y^2} \right) - K_{2y} \frac{x^2}{r_x^2} - K_{3y} \frac{z^2}{r_z^2} \right] \tag{2.30}$$

$$\sigma_z = \sigma_0 \left[K_{1z} \left(1 - \frac{z^2}{r_z^2} \right) + K_{2z} \frac{x^2}{r_x^2} - K_{3z} \frac{y^2}{r_y^2} \right] \tag{2.31}$$

$$\tau_{xy} = -\sigma_0 \left[\frac{K_1}{2(1-\nu)} \frac{xy}{r_x^2} \right] \tag{2.32}$$

$$\tau_{yz} = -\sigma_0 \left[\frac{K_2}{2(1-\nu)} \frac{yz}{r_x^2} \right] \tag{2.33}$$

$$\tau_{xz} = -\sigma_0 \left[\frac{K_3}{2(1-\nu)} \frac{xz}{r_x^2} \right], \tag{2.34}$$

with

$$\sigma_0 = \frac{1}{4} \rho_{\mathrm{r}} \omega_{\mathrm{r}}^2 r_x, \tag{2.35}$$

which corresponds to the average value of σ_x on the central section $x = 0$ of the ellipsoid. Based on the necessary boundary conditions that the stresses vanish at the surface of the ellipsoid, the 12 coefficients in (2.29)–(2.34), which depend only on the two shape ratios

$$\delta_{yx} = \frac{r_y}{r_x} \qquad \text{and} \qquad \delta_{zx} = \frac{r_z}{r_x}, \tag{2.36}$$

can be solved for numerically [52]. To obtain the principal normal stress and the von Mises stress, (2.6) and (2.12) are used, respectively.

The moments of inertia around the principal axes of an ellipsoid of uniform density and mass m are given as

$$I_x = \frac{m}{5}(r_y^2 + r_z^2), \quad I_y = \frac{m}{5}(r_x^2 + r_z^2), \quad \text{and} \quad I_x = \frac{m}{5}(r_x^2 + r_y^2), \tag{2.37}$$

yielding the rotational stability conditions

$$\delta_{zx} < 1 \quad \text{and} \quad \delta_{yx} > \delta_{zx}, \tag{2.38}$$

which have to be fulfilled simultaneously.

2.4.4 Sphere

For the particular case of a sphere, which represents a subset of the solution for the ellipsoid ($r_x = r_y = r_z = a$), a closed-form analytic solution for the stresses can be obtained in cylindrical coordinates as

[54, 55]

$$\sigma_r = \rho_\mathrm{r}\omega_\mathrm{r}^2 \left[\frac{(5\nu^2 - \nu - 12)(a^2 - r^2) + (9 + 7\nu)z^2}{5(\nu - 1)(7 + 5\nu)}\right] \tag{2.39}$$

$$\sigma_\varphi = \rho_\mathrm{r}\omega_\mathrm{r}^2 \left[\frac{(5\nu^2 - \nu - 12)a^2 + (4 + 7\nu + 5\nu^2)r^2 + (9 + 7\nu)z^2}{5(\nu - 1)(7 + 5\nu)}\right] \tag{2.40}$$

$$\sigma_z = \rho_\mathrm{r}\omega_\mathrm{r}^2 \left[\frac{(3 - 6\nu - 5\nu^2)(a^2 - 2r^2 - z^2)}{5(\nu - 1)(7 + 5\nu)}\right] \tag{2.41}$$

$$\tau_{rz} = \rho_\mathrm{r}\omega_\mathrm{r}^2 \left[\frac{(3 - 6\nu - 5\nu^2)rz}{5(\nu - 1)(7 + 5\nu)}\right]. \tag{2.42}$$

The resulting maximum principal normal stress and the von Mises stress distributions on a vertical cross-sectional plane through the center of a sphere with radius $a = 0.25\,\mathrm{mm}$ rotating at $40\,\mathrm{Mrpm}$ are shown in Fig. 2.4. It can be seen that the stress reaches its maximum in the center of the sphere ($x = y = z = 0$) and decreases toward the outside. At the poles, the considered stresses are zero. The maximum von Mises stress is slightly higher than the maximum principal normal stress, which results in the prediction of failure at lower rotational speeds.

For a sphere $\delta_{yx} = \delta_{zx} = 1$ holds, which results in $I_1 = I_2 = I_3$. Therefore, no preferred stable axis of rotation exists in theory. In practice, slight deviations of the moments of inertia will exist due to imbalances and inhomogeneities of the material density. As a consequence, the rotational axis will self-align to the largest moment of inertia during spin up.

2.4.5 Comparison

A comparison of different rotor shapes is carried out based on the occurring maximum values of the principal normal stress and the von Mises stress. For each shape, the constant C_s as used in (2.1) was determined for the maximum normal stress (Rankine) and the distortion energy (von Mises) failure criteria. The results are provided in Table 2.1 with numerical values calculated for $\nu = 0.3$. To obtain high rotational speeds, the shape factor C_s should be as low as possible. The lowest shape factor for materials failing by brittle failure is obtained for a sphere followed by a thin disk. If ductile failure occurs, the lowest shape factor is attained by

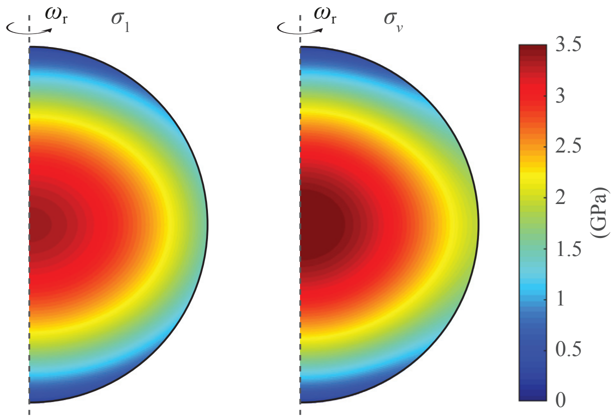

Figure 2.4: Maximum principal normal stress σ_1 (left) and von Mises stress σ_v (right) distributions on a vertical cross-sectional plane through the center of a sphere with radius $a = 0.25\,\mathrm{mm}$ made from 100Cr6 (1.3505) chrome steel and rotating at 40 Mrpm.

Table 2.1: Rotor shape factors for different failure criteria

Shape	C_s (Rankine)		C_s (von Mises)	
Thin disk	$\frac{3+\nu}{8}$	0.413	$\frac{3+\nu}{8}$	0.413
Thin disk w/ pinhole	$\frac{3+\nu}{4}$	0.825	$\frac{3+\nu}{4}$	0.825
Long cylinder	$\frac{3-2\nu}{8(1-\nu)}$	0.429	$\frac{3-4\nu}{8(1-\nu)}$	0.321
Sphere	$\frac{5\nu^2-\nu-12}{5(\nu-1)(7+5\nu)}$	0.398	$\frac{3+2\nu}{7+5\nu}$	0.424

a long cylinder. However, this shape is unsuitable for high-speed rotation as discussed in Section 2.4.2.

An optimization of the rotor shape can be performed using the equations presented in Section 2.4.3 and results in a prolate spheroid ($r_z > r_x = r_y$) that fulfills $r_z < \sqrt{3}r_x$. For the desired geometries with diameters of less than 1 mm, the complexity of the rotor shape is restricted by manufacturability. The symmetry and related balance of the rotor are important factors which are determined by the achievable tolerances and can cause premature failure of the rotor under centrifugal loading if not fulfilled to a lower limit. Consequently, the availability of manufacturing techniques for producing the desired rotor shape with high precision has to be considered in the selection process.

Spheres made from the steels with the highest specific strengths considered in Section 2.3 are readily available due to their use in ball bearings. Nominal diameters into the submillimeter range are available for miniature applications. The tolerances of such steel balls are classified in grades [56]. For the grade with the lowest tolerances (G3), the mean diameter of a single sphere is within ±5.3 µm of the nominal diameter. The diameter variation, referring to the difference between the largest and the smallest diameter of the same ball, is below 0.08 µm. The same value describes the deviation from an ideally spherical shape, which is obtained as the greatest radial distance between a sphere circumscribed around the ball surface and any point on the ball surface itself in all planes passing through the center of the sphere. Due to these low tolerances and their easy availability from materials with high specific strengths, such steel balls are mechanically well suited for use as rotors in the ultra-high-speed motor.

2.5 Magnetic Characterization of Steel Spheres

To achieve sufficiently low frictional torque at ultra-high rotational speeds, a magnetic suspension system for the rotor as described in detail in Chapter 3 is used. For this reason, the magnetic properties of the materials from which the steel balls are manufactured are of interest. While their mechanical characteristics and detailed material composition are usually documented in the literature [56], insufficient information is available regarding the magnetic properties. The latter are strongly dependent on the raw material and manufacturing techniques, similar to the mechanical attributes [57]. Consequently, magnetic characterization should be carried out using specimens that are of the same size as the employed rotors. This makes it impossible to use a closed magnetic circuit measurement, as commonly employed in magnetic characterization [58, 59]. Instead, open circuit measurements using a vibrating sample magnetometer (VSM) (PMC MicroMag 3900) have been carried out to record the magnetization curves of various materials. In this measurement technique, the sample is introduced into a homogeneous external magnetic field $\vec{H}$, of which the magnitude is slowly varied to cover the desired range. This external magnetic field causes the sample to attain a magnitude-dependent magnetic moment $\vec{m}$. By mechanically vibrating the sample in the direction perpendicular to its magnetization, a voltage is induced in stationary pick-up coils placed in its vicinity due to the relative movement. As the induced voltage is proportional to $\vec{m}$, the magnetic properties of the sample can be inferred from it [60]. Aside from the magnetic moment, the induced voltage also depends on the sample geometry as studied in [61, 62]. To eliminate the necessity of compensating this effect, and to obtain high accuracy, the instrument was calibrated with a spherical reference sample of similar dimensions to the rotors (chemically pure Ni $d = 1\,\mathrm{mm}$, cf. [63]).

The measurements were carried out with spherical samples of 0.5 to 1.4 mm in diameter. The tested materials were found to exhibit isotropic magnetic properties, which was verified by repeated measurements after rotation of the sample. For isotropic materials, the magnetization of the sample can be obtained from the measured magnetic moment as

$$M = \frac{m}{V}, \tag{2.43}$$

where V denotes the sample volume. The magnetization curve is obtained as

$$B = \mu_0(H + M), \tag{2.44}$$

of which the slope yields the local relative permeability μ_r as

$$\mu_r = \frac{\mathrm{d}M}{\mathrm{d}H} + 1. \tag{2.45}$$

The measured magnetization curves for several steels commonly employed for the spheres of ball bearings are shown in Fig. 2.5(a). These martensitic chrome steels, which are identified by the material numbers 100Cr6, X65Cr13, X47Cr14, X46Cr13, and X105CrMo17 exhibit almost identical characteristics regarding the initial value of μ_r. The narrow hysteresis loop, as shown in the inset, exhibits low remanence, which is favorable for usage in conjunction with the magnetic suspension and saturation occurs above 1 T. The initial relative permeability is ≈ 4 and is listed for

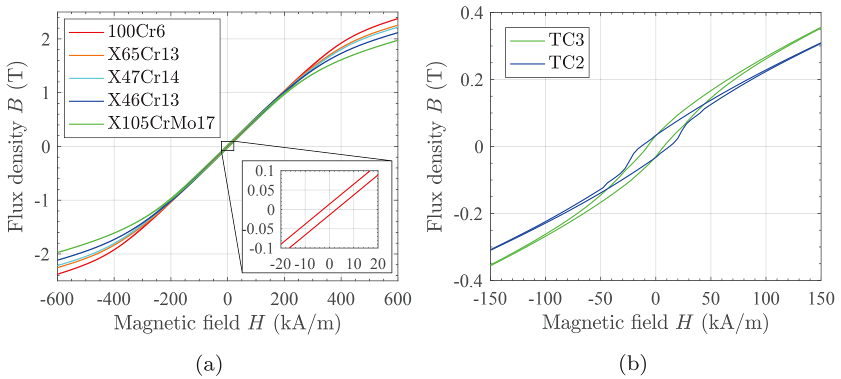

Figure 2.5: Measured magnetization curves of common ball bearing steels (a) and carbide balls (b).

the different materials in Table 2.2, where the stated conductivity values were taken from the respective datasheet if available.

In addition, the magnetization curves of two exemplary materials for carbide balls were recorded, for which the results are shown in Fig. 2.5(b). Such materials exhibit a significantly different magnetic behavior with wider hysteresis loops and lower values of the saturation flux density. This behavior is caused by their composition consisting of a crystal structure containing tungsten carbide and cobalt, which causes high hardness of these materials. Closer inspection shows that the overall magnetization curves consist of multiple smaller hysteresis loops, which correspond to the aforementioned composition elements. Due to the relatively high remanence and the low saturation flux density, these materials are less suitable for magnetic suspension.

Based on the analyses presented in this chapter, it can be concluded that steel spheres as intended for use in ball bearings can be used as rotors in the considered ultra-high-speed motor. The steels used for such balls exhibit high tensile strengths and linear magnetic properties with low hysteresis and high saturation flux densities. The employed manufacturing techniques result in low tolerances and high sphericity, which are both favorable properties for attaining ultra-high rotational speeds.

Table 2.2: Electromagnetic properties of different rotor materials

Material Number	σ (MS/m)	μ_r
100Cr6	~ 4.6	4.13
X65Cr13	~ 1.8	4.14
X47Cr14	~ 1.8	4.12
X46Cr13	~ 1.8	4.17
X105CrMo17	~ 1.3	4.09
TC3	-	3.46
TC2	-	4.47

The suspension and rotation of such spheres by means of electromagnetic forces is considered in the subsequent chapters.

Chapter 3

Magnetic Suspension

To achieve ultra-high rotational speeds, a submillimeter-size steel rotor has to be suspended and accelerated in vacuum. This chapter provides a short overview of suspension concepts commonly used for the rotors in electric machines along with a discussion of their limitations for application in this work. Subsequently, the concept of active magnetic levitation, which is found to have favorable properties at the desired rotational speeds, is analyzed in detail. This includes an analytical model for the generated force and the selection of a suitable topology for stabilization of the rotor in all translatory degrees of freedom. Moreover, an actuator design which allows for magnetic force coupling through a vacuum chamber wall is presented.

3.1 Concepts

Conventional electric machines employ ball bearings to fix the translatory degrees of freedom of the rotor, while allowing for its free rotation. Such bearings require mechanical contact between the rotor and the stator via a rolling element, which generates mechanical friction losses. These losses increase with the rotational speed and the loading of the bearing. Models for the different loss components in ball bearings are outlined in [56]. The highest rotational speed achieved with ball bearings is in the range of 1 Mrpm, which results in bearing losses in the range of 10 W with reduced lifetimes in the range of hours [33]. Consequently, ball bearings are unsuitable for the desired rotational speeds of several tens of million rpm due to excessive losses. Moreover, the use of oil or grease as a lubricant usually prevents their application in vacuum environments and a suspension of the rotor requiring mechanical contact would be difficult to manufacture due to the small geometry and extremely low tolerances.

Contactless gas bearings, in which the rotor is suspended on a gas cushion, allow significantly lower losses due to the absence of mechanical contact. Such bearings have already been employed during early high speed tests as discussed in Section 1.2 and are also being explored for electrical drive systems [35]. Models for the losses due to air friction in such bearings are provided in [64]. The loss power scales quadratically with the rotational speed under laminar conditions without slip and is inversely proportional to the bearing clearance between the rotor and the stator, which would have to be very small for the considered case due to the small rotor geometry. In addition, the bearing journal or bushing of gas bearings usually contains microstructure grooves to prevent whirl instability phenomena. Due to the small dimensions, the implementation of such structures is not feasible for the considered case. As the surrounding gas is used as an inherent part of this bearing type for lubrication and to provide load carrying capability, operation in vacuum is not possible. This prevents leveraging the advantages of spinning the rotor in vacuum as outlined in Section 4.4.

Suspension of the rotor by means of electromagnetic forces is the only contactless bearing technology that can be applied in vacuum or at low pressures. Magnetic bearings have been employed in electric machines of various sizes down to several millimeters and can also be integrated to employ the same magnetic circuit of the machine with either using separate dedicated bearing windings or combined windings for bearing force and torque generation [65, 66]. The former topology is commonly referred to as *self-bearing*, while the latter is commonly referred to as *bearingless*. Contrarily, the utilization of electrostatic forces has been favored for micromotors and MEMS devices [20, 67–69] due to available production techniques and the higher energy density limits for small air gaps.

As the steel rotor considered for obtaining high rotational speeds exhibits ferromagnetic properties, it can be levitated by means of magnetic forces as well as electrostatic forces. An electrostatic levitator that can be used to suspend conductive and insulating materials, independent of their ferromagnetic properties was presented in [70]. A comparison between the achievable energy density for an electric and a magnetic field can be used to assess which suspension technique is favorable at the considered scale (cf. [71]). In an electric field, the energy density in a linear isotropic region is given as

$$w_{\mathrm{el}} = \frac{1}{2}\epsilon E^2 \tag{3.1}$$

and that in a magnetic field as

$$w_{\mathrm{m}} = \frac{1}{2\mu}B^2, \tag{3.2}$$

where ϵ, μ, E, and B denote the electric permittivity, magnetic permeability, and the magnitudes of the electric field as well as the magnetic flux density, respectively. The maximum value of B in air gaps is limited by saturation of ferromagnetic materials and can be estimated to be in the range of 1 T. The maximum value of E is limited by the breakdown field strength, which is $E_{\mathrm{B}} \approx 3\,\mathrm{MV/m}$ for air at ambient pressure and large air gaps. Using these values in (3.1) and (3.2) yields energy densities of $40\,\mathrm{J/m^3}$ for electric fields and $400\,\mathrm{kJ/m^3}$ for magnetic fields, which illustrates the dominance of magnetic systems at the macroscopic scale. However, significantly higher energy densities can be attained in electric fields on the micro scale due to an increase of E_{B} as governed by Paschen's law [72]

$$E_{\mathrm{B}} = \frac{C_2 p}{\ln(pd) + k} \quad \text{with} \quad k = \ln\left[\frac{C_1}{\ln(1+\gamma^{-1})}\right], \tag{3.3}$$

where C_1, C_2, p, γ, and d denote two empirical constants, the gas pressure, the secondary ionization coefficient (Townsend coefficient) of the considered gas, and the air gap length, respectively. The values of C_1 and C_2 depend on the product pd and can be found in the literature [73]. For ambient pressure conditions, this results in an increase of the admissible breakdown electric field and, consequently, an increase of the electric field energy. Considering the aforementioned flux density of 1 T, the electric field energy density exceeds that of the magnetic field at a gap distance of $\approx 5\,\mu\mathrm{m}$. In a vacuum much higher electric fields can be attained in theory due to the lack of gas ionization. However, the applicable voltage is usually limited by practical constraints. Considering a maximum admissible voltage of 1 kV, which is rather high for small-scale systems, and reducing the maximum attainable magnetic flux density to

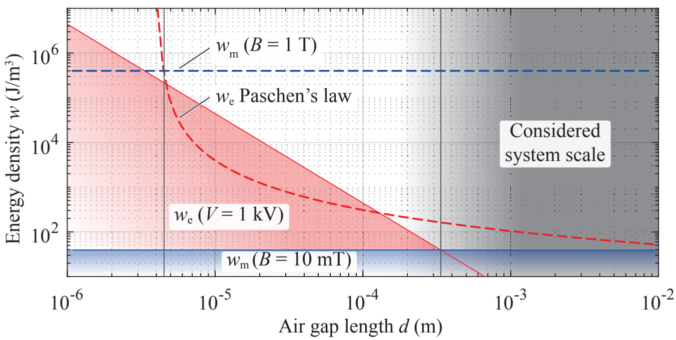

Figure 3.1: Electric energy density limits according to Paschen's law and for a fixed voltage (red) as well as magnetic energy density for different flux densities (blue).

10 mT, the electric energy density is only higher than the magnetic one for air gaps below 300 µm. These relations are illustrated in Fig. 3.1.

As these air gap dimensions are below those expected in the ultra-high-speed motor and because of the difficulties associated with handling voltages in the kilovolt range, while magnetic flux densities in the range of 10 mT can easily be attained, magnetic suspension is employed in this work.

In principle, reluctance forces and/or Lorentz forces can be used for magnetic suspension. A classification of magnetic bearings and magnetic levitation principles is provided in [65, 66, 74].

The magnetic reluctance force acts perpendicular to the surface of materials of different relative magnetic permeabilities μ_r. The rotor has to consist of a ferromagnetic material to achieve sufficiently high forces. In accordance with Earnshaw's theorem [75], it is not possible to obtain stable suspension of the rotor with a static magnetic field. Consequently, magnetic levitation by means of the reluctance force requires active control of the rotor position.

In contrast, passive electrodynamic levitation of the rotor is possible by using the Lorentz force, which acts perpendicular to the flux density. A force is only generated if the rotor consists of a conductive material. Eddy currents are induced inside the rotor by placing it into an alternating magnetic field. A repelling Lorentz force is generated from the interaction of the external magnetic field with these eddy currents. The magnitude of this force depends on the conductivity of the rotor material, its shape, as well as the magnitude and frequency of the external magnetic field [76–78]. If the rotor is made from a ferromagnetic material, an additional reluctance force, which counteracts the Lorentz force, is generated. For a rotor levitated above an actuator coil, the magnetic field and the eddy currents inside the rotor are increased if the rotor approaches the coil. This increases the repulsive force, which makes it possible to achieve passive suspension without the requirement for active control [79, 80]. However, translatory oscillations of the suspended object are weakly damped, resulting in stability issues. Moreover, for objects suspended against gravity, the entailed eddy current losses easily result in temperatures which cause the suspended objects to melt, especially under vacuum conditions. While this is beneficial for levitation melting applications [81], it is undesired for reaching ultra-high rotational speeds.

For these reasons, electrodynamic levitation is unsuitable for application in the ultra-high-speed motor and is not considered further. Instead, active magnetic suspension of the rotor is treated in detail in the remainder of this chapter.

3.2 Principle of Active Magnetic Levitation

Force generation by an active magnetic bearing (AMB) is based on the interaction between the external magnetic field generated by the bearing actuator (electromagnet) and the rotor field. The employed rotor can be a permanent magnet or consist of a ferromagnetic material that is magnetized by the external field. The magnetization stemming from an external magnetic field points into the same direction as the flux lines and causes a magnetic reluctance force F_m into the opposite direction. This force can be used to counteract the gravitational force F_g to levitate the rotor without mechanical contact as shown in Fig. 3.2 for a system with one degree of freedom.

The magnetic force is a function of the current flowing in the coil of the electromagnet, which is subsequently referred to as the bearing current i_b, and the distance z_b between the rotor and the actuator. The rotor position is continuously measured by a position sensor and fed into a controller that actively regulates the bearing current via a power ampli-

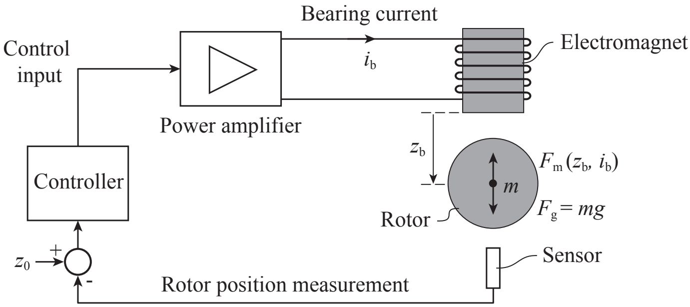

Figure 3.2: Functional principle of an AMB.

fier such that the rotor maintains its reference position z_0. If the rotor is a permanent magnet and is assumed to maintain its orientation, an attracting or repelling force can be generated by reversing the direction of the bearing current. For ferromagnetic rotors that are not permanent magnets, only attracting forces can be generated due to remagnetization of the rotor.

If the system is assumed to be linear, the reluctance force as generated by the electromagnet can be obtained by calculating the derivative of the magnetic energy

$$W_\mathrm{m}(z_\mathrm{b}, i_\mathrm{b}) = \frac{1}{2} L(z_\mathrm{b}) i_\mathrm{b}^2 \tag{3.4}$$

with respect to the rotor position z_b, resulting in

$$F_\mathrm{m}(z_\mathrm{b}, i_\mathrm{b}) = \frac{1}{2} \frac{\partial L(z_\mathrm{b})}{\partial z_\mathrm{b}} i_\mathrm{b}^2 \approx C \frac{i_\mathrm{b}^2}{z_\mathrm{b}^2}, \tag{3.5}$$

where the approximate relation $L(z) \propto 1/z$ has been employed and C denotes a constant.

Despite these nonlinearities, which are also affected by saturation for small air gaps and high currents, linear control schemes can usually be applied by linearization around an operating point as

$$\begin{aligned} f_\mathrm{m}(z, i) &= F_\mathrm{m}(z_\mathrm{b}, i_\mathrm{b}) - mg \\ i &= i_\mathrm{b} - i_0 \end{aligned} \tag{3.6}$$

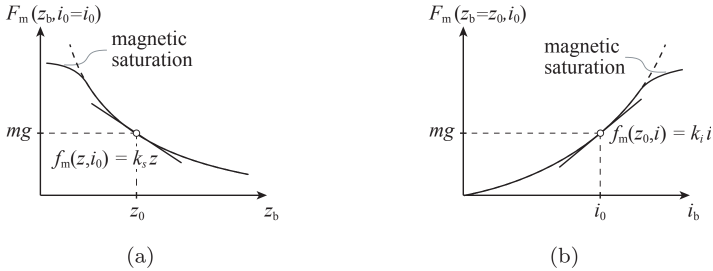

Figure 3.3: Linearization around the operating point: relationship between the magnetic force and displacement (a), and between the magnetic force and electromagnet current (b).

$$z = z_\mathrm{b} - z_0,$$

where i_0 denotes the bearing current at the desired rotor position z_0 and f_m, i, z denote deviations from the desired operating point as shown in Fig. 3.3. Using (3.6) in (3.5) yields

$$f_\mathrm{m}(z, i) = k_s z + k_i i, \tag{3.7}$$

where k_s, k_i denote the force per displacement and force per current constant, respectively. This linearization is illustrated in Fig. 3.3. It can be seen that k_s is negative, corresponding to a decreasing force for an increased distance between the rotor and the electromagnet. This shows that the system is passively unstable and requires active control of the electromagnet current, as described in detail in Chapter 7.

3.3 Force Calculation

Aside from calculating the magnetic force exerted on the rotor via the magnetic energy as outlined in (3.5), it can also be obtained by solving the underlying magnetic field problem. This offers the possibility to assess the influence of the magnetic properties of the rotor material on the bearing force generation.

Introducing the rotor into the external magnetic field $\vec{H}_\mathrm{ext}$ with magnetic induction $\vec{B}_\mathrm{ext} = \mu_0 \vec{H}_\mathrm{ext}$, as generated by the electromagnet, results in its magnetization $\vec{M}$. The latter depends on $\vec{H}_{\mathrm{ext}}$ and the magnetic properties of the rotor material as characterized by its B-H curve. To obtain the reluctance force, the calculations are separated into the four following steps:

1. The magnetic field due to the magnetized rotor is calculated without the presence of an external magnetic field. For this purpose, the rotor is treated as if it was a permanent magnet.
2. The solution for a magnetized sphere in an external field is obtained by superimposing the result from the previous step and the external magnetic field.
3. An expression for the magnetization $\vec{M}$ of the rotor dependent on the external field is obtained based on the magnetic material properties.
4. The reluctance force is calculated from the interaction between $\vec{B}_{\mathrm{ext}}$ and $\vec{M}$.

The field problem is solved based on Maxwell's equations

$$\vec{\nabla} \cdot \vec{B} = 0 \qquad \text{(Gauss's law)} \tag{3.8}$$

$$\vec{\nabla} \times \vec{H} = \frac{\partial \vec{D}}{\partial t} + \vec{J}, \qquad \text{(Ampère's law)} \tag{3.9}$$

where $\vec{D}$ denotes the electric displacement field. In addition, the material relation $\vec{B} = \mu \vec{H}$ is used. As the magnetic field varies slowly with time, displacement currents are negligible ($\partial \vec{D}/\partial t = 0$), and the principles of magnetostatics can be applied. Due to the absence of current carrying conductors in the region of interest ($\vec{J} = 0$), (3.9) becomes

$$\vec{\nabla} \times \vec{H} = 0. \tag{3.10}$$

Consequently, a magnetic scalar potential Φ_{m} can be introduced as

$$\vec{H} = -\vec{\nabla}\Phi_{\mathrm{m}}. \tag{3.11}$$

By treating the rotor as a permanent magnet with a given magnetization $\vec{M}$, (3.8) can be written as

$$\vec{\nabla} \cdot \vec{B} = \mu_0 \vec{\nabla} \cdot (\vec{H} + \vec{M}). \tag{3.12}$$

Using (3.11), this becomes a magnetostatic Poisson equation

$$\nabla^2\Phi_\mathrm{m} = -\rho_\mathrm{m}, \tag{3.13}$$

where

$$\rho_\mathrm{m} = -\vec{\nabla}\cdot\vec{M} \tag{3.14}$$

denotes the effective magnetic volume charge density, which is used as a mathematical analogy to the electrical volume charge density used in electrostatics. Similarly, the surface magnetic charge density is defined as

$$\sigma_\mathrm{m} = \vec{M}\cdot\vec{n}, \tag{3.15}$$

where $\vec{n}$ denotes the normal vector of the considered surface.

For a uniformly magnetized sphere with $\vec{M} = M_0\vec{e}_z$, a solution for Φ_m in spherical coordinates is found as [82]

$$\Phi_\mathrm{m}(r,\theta) = \begin{cases} \dfrac{1}{3}M_0 r\cos\theta & r \le a \qquad (3.16\mathrm{a}) \\[2ex] \dfrac{1}{3}M_0\dfrac{a^3}{r^2}\cos\theta & r > a. \qquad (3.16\mathrm{b}) \end{cases}$$

Consequently, the magnetic field and magnetic induction inside the sphere are

$$\vec{H}_\mathrm{in} = -\frac{1}{3}\vec{M} \tag{3.17}$$

$$\vec{B}_\mathrm{in} = \mu_0(\vec{H}_\mathrm{in} + \vec{M}) = \frac{2\mu_0}{3}\vec{M} \tag{3.18}$$

for a linear medium.

To obtain the field inside the sphere placed in an external magnetic field, the internal magnetization and the external flux density are superimposed, yielding

$$\vec{H}_\mathrm{in} = \frac{1}{\mu_0}\vec{B}_\mathrm{ext} - \frac{1}{3}\vec{M} \tag{3.19}$$

$$\vec{B}_\mathrm{in} = \vec{B}_\mathrm{ext} + \frac{2\mu_0}{3}\vec{M}. \tag{3.20}$$

By not treating the rotor as a permanent magnet any more and instead letting its magnetization result from the applied external magnetic field,

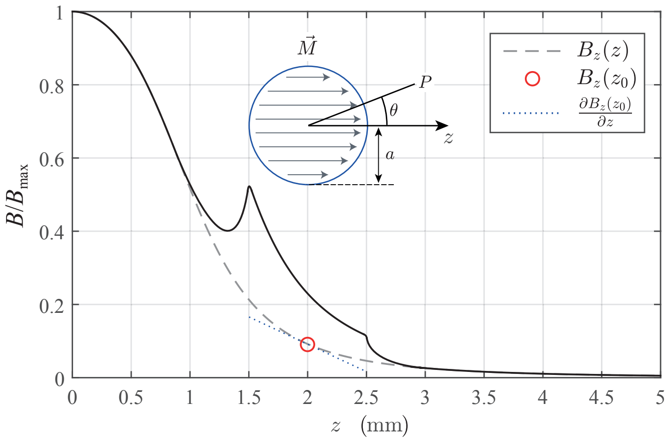

Figure 3.4: Normalized magnitude of the magnetic induction inside and outside of the sphere for varying distance from the actuator coil.

a general expression for the magnetic induction inside the sphere is found by eliminating $\vec{M}$ from (3.19) and (3.20) as

$$\vec{B}_{\text{in}} + 2\mu_0 \vec{H}_{\text{in}} = 3\vec{B}_{\text{ext}}, \tag{3.21}$$

where the B-H curve of the rotor material yields $\vec{B}_{\text{in}} = \mu(|\vec{H}_{\text{in}}|)\vec{H}_{\text{in}}$ for isotropic materials.

The resulting magnetic induction inside and outside the rotor is displayed qualitatively in Fig. 3.4, where the electromagnetic actuator was modeled as a solenoid. The amplification of the magnetic induction inside the rotor is clearly visible. If the rotor material is assumed to be isotropic and linear (no saturation and hysteresis), $\vec{M}$ can be obtained by using

$$\vec{B}_{\text{in}} = \mu_0 \mu_r \vec{H}_{\text{in}}, \tag{3.22}$$

where μ_r is the relative permeability of the rotor material. Using this relation in (3.19) and (3.20) and rearranging yields

$$\vec{M} = \frac{3}{\mu_0} \left(\frac{\mu_r - 1}{\mu_r + 2} \right) \vec{B}_{\text{ext}}. \tag{3.23}$$

This shows that for a given value of $\vec{B}_{\text{ext}}$, the magnetization increases rapidly for small values of μ_r and asymptotically approaches $3\vec{B}_{\text{ext}}/\mu_0$.

The total magnetic force acting on a body with magnetization $\vec{M}$, volume V, and bounding surface S can be obtained from the elementary force law as

$$\vec{F}_{\text{m}} = \int_V \rho_{\text{m}} \vec{B}_{\text{ext}} \mathrm{d}V + \int_S \sigma_{\text{m}} \vec{B}_{\text{ext}} \mathrm{d}S. \tag{3.24}$$

To obtain an analytic solution, two further simplifying assumptions are introduced, namely:

- The magnetization $\vec{M}$ of the rotor is uniform with magnitude M_0 and direction $\vec{e}_z$ and is caused by the magnitude of the external magnetic induction $|\vec{B}_{\text{ext}}|$ at the center of the rotor ($z = z_0$).
- The magnitude of the external magnetic induction varies linearly over the diameter of the sphere, with its gradient being determined by $\partial|\vec{B}_{\text{ext}}(z_0)|/\partial z$.

Geometrical representations of these simplifications have been added to Fig. 3.4. The smaller the sphere is with respect to the electromagnet used for its suspension, the better these assumptions are justified. Therefore, good agreement of the results obtained by using the actual and simplified problem statement is expected for the considered submillimeter-size rotors.

A uniform magnetization inside the sphere yields $\rho_{\text{m}} = 0$ and the magnetic surface charge is obtained as $\sigma_{\text{m}} = M_0 \cos(\theta)$. Due to symmetry, only the z component of $\vec{B}_{\text{ext}}$ is relevant for the force generation while the other components can be chosen arbitrarily. Incorporating the aforementioned simplifications, this is written as

$$\vec{B}_{\text{ext}} = \left(\frac{\partial B_z(z_0)}{\partial z} z + B_z(z_0) \right) \vec{e}_z. \tag{3.25}$$

The resulting force, including the magnetization determined by (3.23), is obtained as

$$\vec{F}_{\text{m}} = \frac{4\pi a^3}{\mu_0} \left(\frac{\mu_r - 1}{\mu_r + 2} \right) B_z(z_0) \frac{\partial B_z(z_0)}{\partial z} \vec{e}_z. \tag{3.26}$$

This shows that for given values of $B_z(z_0)$ and $\partial B_z(z_0)/\partial z$, the reluctance force levels off for high values of μ_r. For the considered rotor materials with $\mu_r \approx 4$, about 50 % of the maximum possible reluctance force is obtained. As the magnetization of the sphere is directed into the same direction as the external magnetic induction, the resulting force is always directed toward the bearing coil. In the case of vertical suspension of the rotor, this force is counteracted by the gravitational force

$$F_{\mathrm{g}} = mg = \frac{4}{3}\pi a^3 \rho_{\mathrm{r}} g, \tag{3.27}$$

where m denotes the rotor mass. The gravitational force exhibits the same dependency on a as the reluctance force. Consequently, the external magnetic field and, therefore, the current through the electromagnet are expected to be independent of the sphere radius for identical levitation heights z_0.

3.4 Topologies

Stabilization of the rotor in all translatory degrees of freedom requires multiple actuators. Consequently, an arrangement of electromagnets has to be used. If the reluctance force is used to counteract the gravitational force in order to levitate the rotor in the vertical (axial) direction, as shown in Fig. 3.2, the horizontal (radial) translatory degrees of freedom are generally passively unstable. Stabilization can be achieved by combining multiple AMBs or by a suitable design of the axial actuator.

An overview of possible topologies is provided in Fig. 3.5, where the actuators in the horizontal y-direction have been omitted for clarity purposes. The radially-placed actuators can be used to generate the motor torque (see Chapter 4) and magnetic suspension forces simultaneously, which is advantageous due to the confined space around the rotor.

The topology shown in Fig. 3.5(a) requires active stabilization of rotor movements in all translatory degrees of freedom. It is universally applicable to various rotor shapes, such as spheres, disks, and cylinders.

By shaping the tip of the axial actuator core such that the flux is concentrated at the desired horizontal equilibrium position of the rotor, passive radial centering can be achieved (Fig. 3.5(b)). The generated restoring force is proportional to the radial displacement of the rotor,

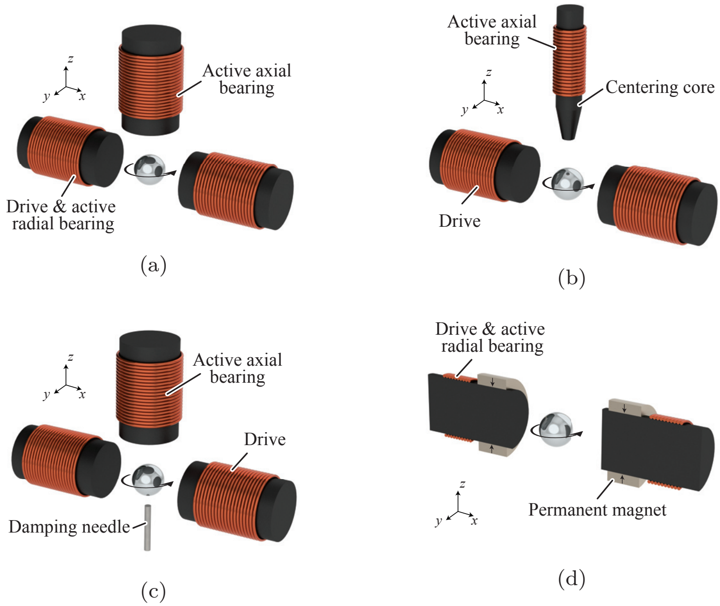

Figure 3.5: Overview of magnetic suspension topologies. (a) Topology for active control of all degrees of freedom. (b) Topology featuring passive radial stiffness of the rotor due to a centering core. (c) Topology featuring passive radial stiffness and damping of the rotor due to a damping needle. (d) Topology using permanent magnets to passively stabilize the rotor in the axial direction while active control in the radial direction is required to achieve levitation.

corresponding to a passive radial stiffness. However, no passive damping of rotor oscillations can be obtained. The setup is suitable for levitating spherical and cylindrical rotors. A disk-shaped rotor is prone to tilting around the horizontal axes and would require modification of its shape to be levitated in such a setup. Introducing a hump in its horizontal center would provide an attraction point for the reluctance force below the centering core. However, such modifications are not easily feasible due to the small overall dimensions of the rotor.

Figure 3.5(c) shows a topology in which a ferromagnetic damping needle with its lower end floating in a viscous fluid is placed below the rotor. The rotor and the needle are both magnetized by the electromagnet of the axial bearing. Consequently, the needle follows horizontal oscillations of the rotor due to magnetic coupling. The energy of the oscillation is dissipated by fluid drag at the lower end of the needle. Such an arrangement was used in the historical studies [6, 41] and works sufficiently well for rotors larger than $\sim 1\,\mathrm{mm}$. Contrarily, it was found to be unsuitable for the desired smaller rotor sizes [17] due to unreliable magnetic coupling between the damping needle and the rotor.

In the aforementioned topologies, the gravitational force was counteracted by an AMB. Another possibility is to use permanent magnets to achieve passive axial stabilization. A general overview of the stability of various permanent magnet levitation systems is provided in [83]. Figure 3.5(d) shows a topology in which passive axial stabilization is achieved by the bias flux of permanent magnets, which are used to magnetize the rotor. The setup can be used for disk-shaped and spherical rotors, while long cylinders cannot be stabilized as they are prone to tilting. Levitation of the rotor is passively unstable in the radial direction and requires active control. Further, axial damping of the rotor cannot be achieved passively and the setup is sensitive to the symmetry of the magnetic bias field. Asymmetries result in drag torques due to eddy currents, which are particularly problematic at ultra-high rotational speeds. Due to these unfavorable properties, this and other topologies employing magnetic bias fields generated by permanent magnets are not considered further in this work.

Instead, the setup of Fig. 3.5(b) combined with active magnetic damping in the radial direction is used in this work to fully stabilize the rotor. In order to provide design guidelines for the required actuators, system models for the translatory dynamics of the levitated rotor in the axial and radial directions are provided below. These models are also used to develop suitable control structures in Chapter 7.

3.5 System Model

The axial actuator of the topology shown in Fig. 3.5(b) with a centering core is considered, for which a schematic cross-sectional view is displayed in Fig. 3.6(a). The diameter of the centering core is considered to be in the same range as the rotor diameter. A dynamic model for the

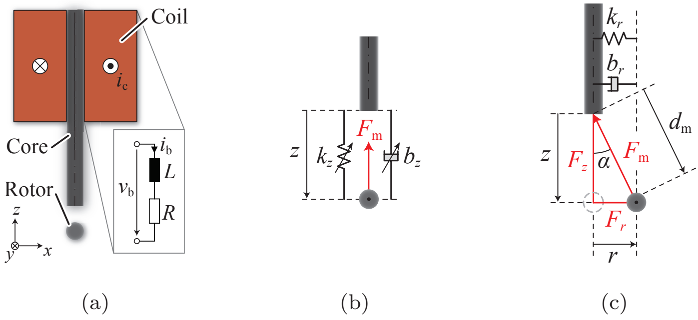

Figure 3.6: (a) Overview of the axial actuator and equivalent circuit of the coil (inset). Components of the dynamic system models in (b) the axial and (c) radial direction.

translatory behavior of the rotor in the axial and radial direction can be developed separately.

The rotor is stabilized actively in the axial direction (Fig. 3.6(b)) by means of closed-loop feedback control, which ensures that $F_\mathrm{m} = F_\mathrm{g}$ at the desired levitation height z_0. Consequently, the dynamic behavior of the rotor is determined by the controller parameters. If a proportional-integral-derivative (PID) feedback controller is used, the mechanical stiffness k_z and damping b_z can be adjusted by the proportional and differential part, respectively. The resulting closed-loop behavior is that of a damped spring-mass pendulum with two complex poles, which is described by the ordinary differential equation (ODE)

$$\ddot{z}(t) + \frac{b_z(z)}{m}\dot{z}(t) + \frac{k_z(z)}{m}z(t) = g - \frac{F_\mathrm{m}(i(t), z)}{m}. \tag{3.28}$$

F_m depends on the coil current i_b that is controlled by a power amplifier. The latter applies a voltage v_b across the terminals of the coil which introduces an additional dynamic behavior based on the rate at which i_b can be adjusted. Based on the equivalent circuit model of the electromagnet coil with inductance L and resistance R, as shown in the inset of Fig. 3.6(a), it is described as

$$\dot{i}_\mathrm{b}(t) + \frac{R}{L}i_\mathrm{b}(t) = \frac{1}{L}v_\mathrm{b}(t). \tag{3.29}$$

In order to stabilize the mechanical system of (3.28), the electrical time constant of the RL circuit $\tau_{\mathrm{el}} = L/R$ has to be much smaller than the period of oscillations of the mechanical system $T_{\mathrm{mech}} \approx 2\pi\sqrt{m/k_z}$, where k_z can be adjusted within a certain range by the controller. Despite the relatively small value of T_{mech} due to the low mass of the rotors in this work, the aforementioned condition can easily be satisfied by an appropriate coil design.

The rotor is passively stable in the radial direction (Fig. 3.6(c)) due to a concentration of the magnetic flux below the centering core. The translatory dynamics of the uncontrolled system in the radial direction with positional variable $r(t) = \sqrt{x^2(t) + y^2(t)}$ is described by a similar ODE as

$$\ddot{r}(t) + \frac{b_r}{m}\dot{r}(t) + \frac{k_r}{m}r(t) = 0, \tag{3.30}$$

where k_r and b_r denote the passive radial stiffness and passive radial damping, respectively.

The axial and radial forces due to a displacement of the rotor by an angle α are obtained as $F_r(\alpha) = F_{\mathrm{m}}(d_{\mathrm{m}}, i_{\mathrm{b}}) \cdot \sin\alpha$ and $F_z(\alpha) = F_{\mathrm{m}}(d_{\mathrm{m}}, i_{\mathrm{b}}) \cdot \cos\alpha$, respectively, where d_{m} denotes the mean geometric air gap length between the coil and the rotor as shown in Fig. 3.6(c). The radial stiffness is obtained as

$$k_r = \frac{\partial F_r(r=0)}{\partial r}. \tag{3.31}$$

A quantitative estimate of k_r can be obtained if a mathematical description for $\partial L(d_{\mathrm{m}})/\partial d_{\mathrm{m}}$ can be found (see (3.5)). In [7], the empirical expression

$$L(d_{\mathrm{m}}) = L_0 + \frac{\Delta L}{1 + c \cdot d_{\mathrm{m}}} \tag{3.32}$$

was used for the inductance of the electromagnet coil. The variables L_0, ΔL, and c denote the inductance of the coil without the rotor, the maximum variation of the coil inductance and a constant, respectively. These parameters can be obtained by measurements or electromagnetic finite element method (FEM) simulations. Due to the small influence of the rotor on the coil inductance, ΔL was found to be less than 1 % of L_0 for the considered geometries, which makes results obtained by

(3.32) prone to error. Instead, k_r was obtained directly from 3D FEM simulations as outlined in the next section.

Damping of translatory radial movements of the levitated rotor is solely caused by gas friction, which is proportional to the velocity $\dot{r}(t)$. Oscillations of the rotor are damped by converting the associated energy into frictional energy in the gas.

Under atmospheric pressure conditions, radial damping is due to laminar gas friction and is obtained as

$$b_{r,\mathrm{c}} = 6\pi\mu a, \tag{3.33}$$

where μ denotes the dynamic viscosity of the surrounding gas [84]. Values in the range of 10^{-7} Ns/m are expected for $b_{r,\mathrm{c}}$ based on the evaluation of (3.33) for submillimeter-size rotors. At pressures in the high vacuum range, free molecular flow conditions apply and the remaining damping can be expressed as

$$b_{r,\mathrm{fm}} = \left(\frac{4}{3} + \frac{\pi}{6}\right)\pi\rho a^2 \bar{c}, \tag{3.34}$$

where ρ and $\bar{c}$ denote the density and mean speed of molecules of the surrounding gas, respectively [85]. This yields values in the range of 10^{-9} Ns/m. Both of the aforementioned values of the damping coefficient are at such a low level that even small disturbances cause weakly damped oscillations of the rotor in the radial direction. If the occurring displacement from the equilibrium position becomes too large, the magnetic suspension becomes unstable. This underlines the requirement for additional radial damping, which is implemented by AMBs in this work.

3.6 Axial Actuator Design

Subsequently, the design of the axial actuator is outlined. The radial actuators are combined with the drive coils of the stator, for which design guidelines are presented in Chapter 5. Based on the aforementioned considerations, the following requirements for the axial actuator of the practical system can be derived:

1. A high magnetic force F_m per current i_b should be generated to

minimize ohmic losses $P_\mathrm{c} = Ri_\mathrm{b}^2$ in the coil. This can be achieved by using a ferromagnetic core to guide the magnetic flux toward the rotor.

2. For the same reason, the coil should have a low series resistance R.
3. The inductance L of the coil has to be sufficiently low, such that $\tau_\mathrm{el} << T_\mathrm{mech}$ is satisfied.

In addition, the actuator should allow for the integration of a vacuum system around the rotor, which is required to achieve ultra-high rotational speeds. Due to the absence of continuum gas flow convection, heat transfer rates in a vacuum are significantly lower than under atmospheric pressure conditions, which limits the cooling capability of the actuator coil. Specially sealed feedthroughs would be required to feed the lead wires for the actuator coil through the wall of the vacuum chamber. For these reasons, the electromagnet coil should not be placed inside the vacuum. Instead, an actuator using magnetic coupling though the chamber wall was developed as shown in Fig. 3.7(a). The centering core is placed inside the vacuum tube, while the coil and yoke are placed on the outside. As shown by the flux lines, the magnetic flux generated by the coil is initially guided by the yoke and then coupled across the air gap to the ferromagnetic centering core, which guides it toward the rotor. For this magnetic coupling to be feasible, the vacuum tube has to consist of a non-ferromagnetic material. As the magnetic field for the axial suspension of the rotor changes slowly and eddy current losses are negligible, the yoke and centering core can be manufactured from a solid ferromagnetic material. The characteristics of the magnetic suspension force in such a system are predominantly determined by the shape of the lower tip of the centering core close to the rotor and were studied using 3D magnetostatic FEM simulations. The resulting normalized forces in the axial and radial directions are shown in Fig. 3.7(b) for a flat as well as a semi-spherical tip of the core and the parameters given in the legend. The radial force is significantly lower than the axial force around the radial center and the expected $\cos(r)$ and $\sin(r)$ dependency can be observed for the axial and radial forces, respectively. The radial stiffness is determined as outlined in (3.31). A flat lower end of the core yields a higher axial force for a given current and a higher passive radial stiffness compared to the semi-spherical end. The latter has the only advantage that the axial force drops less rapidly for a radially displaced rotor, resulting in a more constant axial bearing current.

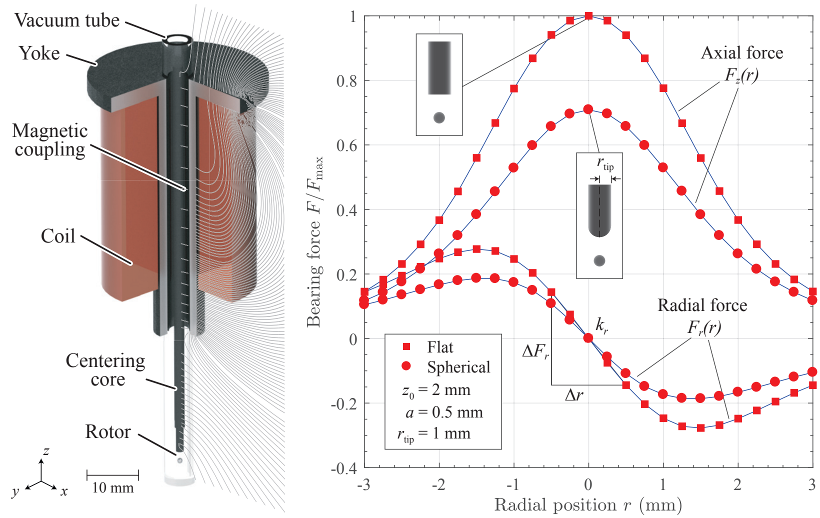

(a) (b)

Figure 3.7: (a) Setup of the axial actuator with an integrated vacuum system. The magnetic coupling is illustrated by the added flux lines. (b) Normalized force characteristics in the axial and radial directions for different tip shapes of the centering core.

While the radius r_{tip} of the centering core is limited to $\sim 1\,\text{mm}$ in the considered system to leave sufficient clearance to the inner wall of the vacuum tube, it can be designed to yield favorable magnetic force properties. Figures 3.8 and 3.9 show the values of k_i and k_r for varying values of r_{tip} as obtained by simulations for a rotor diameter of 1 mm and 0.5 mm, respectively. Again, it can be seen that a flat lower end of the core yields favorable properties for the entire range of the considered values. While k_i exhibits a rapid increase for small values of r_{tip}/a, which is due to the increased cross-sectional area for guiding the magnetic flux toward the rotor, it starts to level off at higher values. Contrarily, k_r shows a maximum at $r_{\text{tip}} \approx 0.8\,\text{mm}$ or 1.6 and 3.2 times the rotor radius for the rotor with $a = 0.5\,\text{mm}$ and $a = 0.25\,\text{mm}$, respectively. Below the maximum, the small size of the tip limits the flux density at the rotor, resulting in lower reluctance forces. This explains the approximately identical loca-

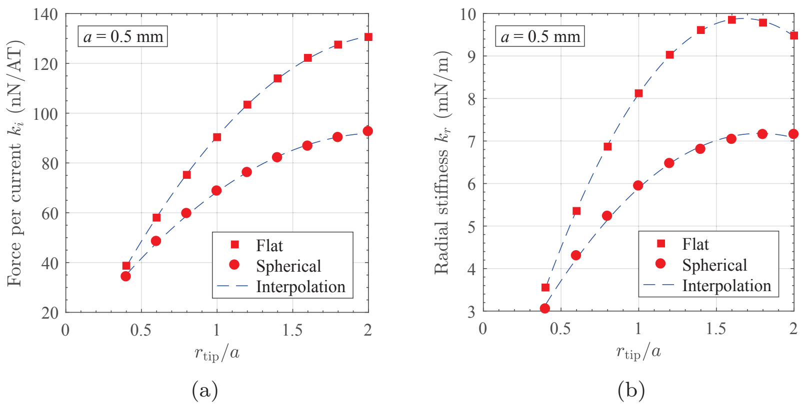

Figure 3.8: Force per current k_i (a) and passive radial stiffness k_r (b) for varying ratios of the tip diameter and the rotor diameter. Results are shown for a rotor with 1 mm in diameter.

tion of the maxima despite the different rotor radii. Above the maximum, the flux density around the horizontal equilibrium position of the rotor becomes more homogeneous, resulting in a decreased restoring force.

Consequently, $r_{\text{tip}} = 0.8\,\text{mm}$ was chosen for the implemented actuator design. To achieve a high magnetic force per coil current, the employed coil of the electromagnet consists of ~ 350 turns of copper wire, resulting in an inductance of several hundreds of µH.

If the generated magnetic field used for suspension and the rotor are ideally symmetrical around the vertical axis through its center of mass, rotation can be attained without hysteresis and eddy-current losses as the magnetization remains constant. In practice, asymmetries will cause periodical remagnetization of the rotor, which results in a residual drag torque. The latter has initially been quantified in [13] and is of high interest for the determination of spin down rates in magnetically suspended spinning rotor vacuum gauges [86], where effects caused by the rotation of the Earth's magnetic field (Coriolis effect) need to be compensated in order to obtain high precision results [87]. For the considered ultra-high-speed motor, the residual drag torques were found to be at

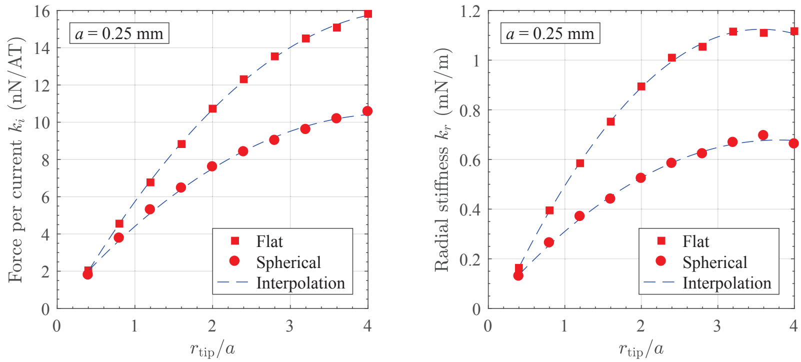

(a) (b)

Figure 3.9: Force per current k_i (a) and passive radial stiffness k_r (b) for varying ratios of the tip diameter and the rotor diameter. Results are shown for a rotor with 0.5 mm in diameter.

negligible levels comparable to those generated by gas friction drag at low pressures in the high vacuum range (see Chapter 4).

Chapter 4

Drive and Loss Models

The lack of direct mechanical contact to the rotor and operation in a vacuum limit the applicable physical principles for driving the rotor. In this chapter, possible concepts are briefly discussed, before a detailed model for driving the rotor by means of electromagnetic fields is provided.

Acceleration of magnetically suspended millimeter-scale rotors by light pressure was studied in [88]. Light directed tangentially at the periphery of the rotor was found to generate a torque. A different technique of using the spin angular momentum (SAM) of circularly polarized light is frequently employed in micro and nanoscale systems [22, 28]. A light-induced torque is generated by transfer of the SAM to an absorbing particle placed in the light beam. Other optical rotation techniques rely on specific rotor properties, such as a shape asymmetry or birefringence, which are not attainable or undesired for the considered rotors. While the achievable torques are sufficiently high to reach rotational speeds of several million rpm with rotors in the nanometer range, they are at a low absolute level. Moreover, absorption of the radiation power leads to significant heating of the rotor, which decreases its mechanical strength.

To overcome the aforementioned disadvantages, electromagnetic torque generation by the principle of a solid rotor induction machine is used in this study. A rotating magnetic field induces eddy currents inside the conductive rotor and a torque is generated based on the interaction between these eddy currents and the external magnetic field. A historically relevant work in this context is [89].

In the following sections, models for the torque and eddy current losses inside the rotor are presented based the analytical solution of the underlying electromagnetic field problem. Subsequent derivations closely follow and extend those presented in [90]. To obtain valid solutions for the

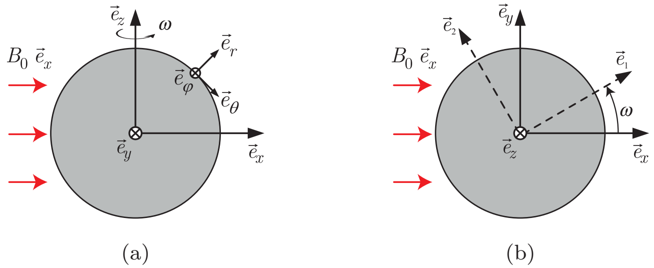

Figure 4.1: Stationary and rotating coordinate systems used for the calculations.

motor torque with the rotor materials used during experiments, the simplifications introduced in this reference have been omitted. Solutions for a similar field problem but with spatial stationarity are presented in [91].

4.1 Electromagnetic Field Problem

4.1.1 Setup and Coordinate Systems

The electromagnetic field problem is formulated for a solid spherical rotor with radius a, permeability μ, and conductivity σ located at the origin of a stationary Cartesian coordinate system with unit vectors $(\vec{e}_x, \vec{e}_y, \vec{e}_z)^T$. The sphere is assumed to rotate at constant angular velocity $\vec{\omega} = \omega_\mathrm{r}\vec{e}_z$ around the z axis in an orthogonally-directed, homogeneous, and time-invariant magnetic field with flux density

$$\vec{B}_0 = B_0\vec{e}_x. \tag{4.1}$$

This setup is shown in Fig. 4.1(a). It should be noted that only the difference between the mechanical rotational frequency of the rotor ω_r and that of the magnetic field ω_f is relevant for the solution of the field problem. This difference is subsequently referred to as the slip frequency ω, according to the naming conventions of induction machines.

A second Cartesian coordinate system with unit vectors $(\vec{e}_1, \vec{e}_2, \vec{e}_z)^T$ that is fixed to the sphere and rotates at the same angular velocity, as shown in Fig. 4.1(b), is introduced. With respect to this coordinate system, the external magnetic field rotates with angular velocity $-\omega$ around the z axis. Due to the shape of the rotor, it is convenient to further introduce a spherical coordinate system with unity vectors $(\vec{e}_r, \vec{e}_\theta, \vec{e}_\varphi)^T$ that is fixed to the rotating sphere. The magnetic flux density is transformed accordingly, yielding

$$\vec{B}_0 = \mathrm{Re}\{B_0 \vec{b} e^{j\omega t}\}, \tag{4.2}$$

with

$$\begin{aligned}\vec{b} &= \begin{pmatrix}1\\ j\\ 0\end{pmatrix} \cdot \begin{pmatrix}\vec{e}_x\\ \vec{e}_y\\ \vec{e}_z\end{pmatrix} e^{-j\omega t} = \begin{pmatrix}1\\ j\\ 0\end{pmatrix} \cdot \begin{pmatrix}\vec{e}_1\\ \vec{e}_2\\ \vec{e}_z\end{pmatrix}\\ &= \begin{pmatrix}\sin\theta(\cos\varphi + j\sin\varphi)\\ \cos\theta(\cos\varphi + j\sin\varphi)\\ j\cos\varphi - \sin\varphi\end{pmatrix} \cdot \begin{pmatrix}\vec{e}_r\\ \vec{e}_\theta\\ \vec{e}_\varphi\end{pmatrix}.\end{aligned} \tag{4.3}$$

The subsequent analyses are carried out in the rotating frame of reference fixed to the spinning sphere.

4.1.2 Basic Equations

The employed basic equations

$$\vec{\nabla} \cdot \vec{B} = 0 \qquad \text{(Gauss's law)} \tag{4.4}$$

$$\vec{\nabla} \times \vec{H} = \frac{\partial \vec{D}}{\partial t} + \vec{J} \qquad \text{(Ampère's law)} \tag{4.5}$$

$$\vec{\nabla} \times \vec{E} = -\frac{\partial \vec{B}}{\partial t}, \qquad \text{(Faraday's law)} \tag{4.6}$$

with material relations

$$\vec{D} = \epsilon \vec{E} \tag{4.7}$$

$$\vec{B} = \mu \vec{H} \tag{4.8}$$

$$\vec{J} = \sigma \vec{E} \tag{4.9}$$

are similar to those used in Section 3.3. However, the considered flux density varies with angular frequency ω. An assumed maximum frequency $f_{\text{max}} = 1\,\text{MHz} \mathrel{\widehat{=}} 60\,\text{Mrpm}$ corresponds to a wavelength in vacuum of $\lambda_{\text{min}} = c/f_{\text{max}} = 300\,\text{m}$, where $c \approx 3 \times 10^8\,\text{m/s}$ is the speed of light. As this is much larger than the considered geometries, wave propagation effects can be neglected and the field quantities can be considered to change simultaneously throughout the entire region of interest. As a result, the displacement current density $\partial\vec{D}/\partial t$ is negligible with respect to the conduction current density $\vec{J}$. This is verified by

$$\max|j\omega_{\text{max}}\epsilon\vec{E}| \ll \max|\sigma\vec{E}| \quad \Rightarrow \quad \frac{\omega_{\text{max}}\epsilon_0}{\sigma} \approx 1.2 \times 10^{-11} \ll 1, \quad (4.10)$$

where the transformation $\partial/\partial t \to j\omega$ and $\sigma = 4.55 \times 10^6\,\text{S/m}$, corresponding to the highest conductivity of the employed rotor materials (see Section 2.5), have been used. Consequently, the magnetoquasistatic approximation $\partial\vec{D}/\partial t = 0$ can be employed without introducing significant errors.

Since $\vec{J} \neq 0$ in the region of interest inside the sphere, the field problem is solved based on the magnetic vector potential $\vec{A}$, which is related to the flux density by

$$\vec{B} = \vec{\nabla} \times \vec{A}. \quad (4.11)$$

Moreover, the Coulomb gauge is used, yielding

$$\vec{\nabla} \cdot \vec{A} = 0. \quad (4.12)$$

From (4.6), the relation between the electric field and the magnetic vector potential results as

$$\vec{E} = -\frac{\partial\vec{A}}{\partial t} \quad (4.13)$$

and (4.9) can be rewritten as

$$\vec{J} = -\sigma\frac{\partial\vec{A}}{\partial t}. \quad (4.14)$$

Using $\partial\vec{D}/\partial t = 0$ in (4.5) in conjunction with (4.8) and (4.14) yields

$$\vec{\nabla}(\vec{\nabla} \times \vec{A}) + \mu_0\mu_r\sigma\frac{\partial\vec{A}}{\partial t} = 0, \quad (4.15)$$

which can be simplified to

$$-\Delta\vec{A} + \mu_0\mu_r\sigma\frac{\partial\vec{A}}{\partial t} = 0, \tag{4.16}$$

where Δ denotes the Laplace operator.

4.1.3 Solution for the Magnetic Vector Potential

A solution for the magnetic vector potential is obtained based on the boundary conditions of the magnetic field and magnetic flux density as well as asymptotic requirements for $\vec{A}$. A detailed account of these conditions is provided in Appendix A.1. Based on these considerations and (4.2), an ansatz according to

$$\vec{A} = \frac{1}{2}B_0\,\mathrm{Re}\{F(r)\vec{b}\times\vec{r}e^{j\omega t}\}, \tag{4.17}$$

with

$$\vec{r} = \begin{pmatrix} r \\ 0 \\ 0 \end{pmatrix} \cdot \begin{pmatrix} \vec{e}_r \\ \vec{e}_\theta \\ \vec{e}_\varphi \end{pmatrix} \tag{4.18}$$

can be used as a solution of (4.11) for the entire space, where $F(r)$ is a complex-valued function. This is equivalent to

$$\vec{A} = \frac{1}{2}B_0 r\,\mathrm{Re}\left\{F(r)\begin{pmatrix} 0 \\ j\cos\varphi - \sin\varphi \\ -\cos\theta(\cos\varphi + j\sin\varphi) \end{pmatrix} \cdot \begin{pmatrix} \vec{e}_r \\ \vec{e}_\theta \\ \vec{e}_\varphi \end{pmatrix} e^{j\omega t}\right\} \tag{4.19}$$

in spherical coordinates.

Detailed derivation steps for $F(r)$ are provided in Appendix A.2. Here, only the results that foster understanding of the subsequent solutions are provided.

The solution for $F(r)$ is separated based on the considered region and is obtained as

$$F(r) = \begin{cases} [1 + D(c_{\mathrm{ec}}a)] \dfrac{f(c_{\mathrm{ec}}r)}{f(c_{\mathrm{ec}}a)} & r \leq a \qquad (4.20a) \\[2ex] 1 + D(c_{\mathrm{ec}}a) \left(\dfrac{a}{r}\right)^3 & r > a, \qquad (4.20b) \end{cases}$$

with

$$D(c_{\mathrm{ec}}a) = \frac{(2\mu_r + 1)g(c_{\mathrm{ec}}a) - 1}{(\mu_r - 1)g(c_{\mathrm{ec}}a) + 1} \tag{4.21}$$

$$g(c_{\mathrm{ec}}a) = \frac{1 - (c_{\mathrm{ec}}a)\cot(c_{\mathrm{ec}}a)}{(c_{\mathrm{ec}}a)^2} \tag{4.22}$$

$$f(c_{\mathrm{ec}}r) = \frac{\sin(c_{\mathrm{ec}}r)}{(c_{\mathrm{ec}}r)^3} - \frac{\cos(c_{\mathrm{ec}}r)}{(c_{\mathrm{ec}}r)^2} \tag{4.23}$$

$$c_{\mathrm{ec}} = \sqrt{-j\mu\sigma\omega} = \frac{1-j}{\delta}, \tag{4.24}$$

where δ denotes the skin depth

$$\delta = \sqrt{\frac{2}{\sigma\omega\mu}}. \tag{4.25}$$

4.1.4 Magnetic Flux Density

Based on this solution, the magnetic flux density inside and outside the rotor can be calculated using (4.11). Inserting (4.19) yields

$$\begin{aligned} \vec{B} = & B_0 \operatorname{Re}\Bigg\{ \Bigg[F(r) \begin{pmatrix} \sin\theta(\cos\varphi + j\sin\varphi) \\ \cos\theta(\cos\varphi + j\sin\varphi) \\ j\cos\varphi - \sin\varphi \end{pmatrix} \\ & + \frac{r}{2}\frac{\partial F(r)}{\partial r} \begin{pmatrix} 0 \\ \cos\theta(\cos\varphi + j\sin\varphi) \\ j\cos\varphi - \sin\varphi \end{pmatrix} \Bigg] \cdot \begin{pmatrix} \vec{e}_r \\ \vec{e}_\theta \\ \vec{e}_\varphi \end{pmatrix} e^{j\omega t} \Bigg\}. \end{aligned} \tag{4.26}$$

This shows that the external flux density B_0 is scaled by the function $F(r)$ as well as $r/2 \cdot \partial F(r)/\partial r$. To analyze this and the subsequent

Table 4.1: Parameters used in the calculations

Rotor radius	a	0.25 mm
Flux density	B_0	1.5 mT
Conductivity of the rotor	σ	4.55 MS/m
Relative permeability of the rotor	μ_r	4
Conductivity of the environment	σ	0 S/m
Relative permeability of the environment	μ_r	1

results further, an exemplary set of system parameters, which are similar to those attained during experiments, is used. These parameters are listed in Table 4.1.

Figure 4.2 shows the aforementioned scaling functions for two exemplary slip frequencies. While the magnitude of the flux density is almost homogeneous throughout the rotor for $f = 100\,\mathrm{kHz}$, a reduction at the center of the rotor and amplification toward its surface can be observed for $f = 1\,\mathrm{MHz}$ due to the skin effect. This is also visible in the top row of Fig. 4.3, which shows the flux density distribution inside the sphere as obtained by (4.26). In the xy-plane, the flux density only features components in $\vec{e}_r$ and $\vec{e}_\varphi$ directions, while $B_\theta = 0$ due to $\cos\theta = 0$. Moreover, results from 3D FEM eddy current simulations using the parameters of Table 4.1 are shown in the bottom row of Fig. 4.3 to verify the presented model. Direct comparison shows an excellent agreement of the calculated and the simulated results. The field distribution for $f = 10\,\mathrm{MHz}$ illustrates that the validity of the model extends to higher field frequencies. At this frequency, the center of the rotor is field-free, while the flux density is concentrated at the surface. For rotor materials with higher values of μ_r and σ, this effect occurs already at lower slip frequencies (cf. [90]). The maximum flux density occurs at $r = a$ and is shown in Fig. 4.4 with respect to B_0 over a wide range of slip frequencies. For practically attainable values of f, the amplification is below a factor of three. This, together with the limitation of B_0 to a few millitesla by thermal constraints (see Section 4.6), prevents the occurrence of flux densities that would cause saturation of the rotor material. Consequently, the implicit assumption of a linear magnetic behavior of the material ($\mu_r = \mathrm{const}$) is well satisfied.

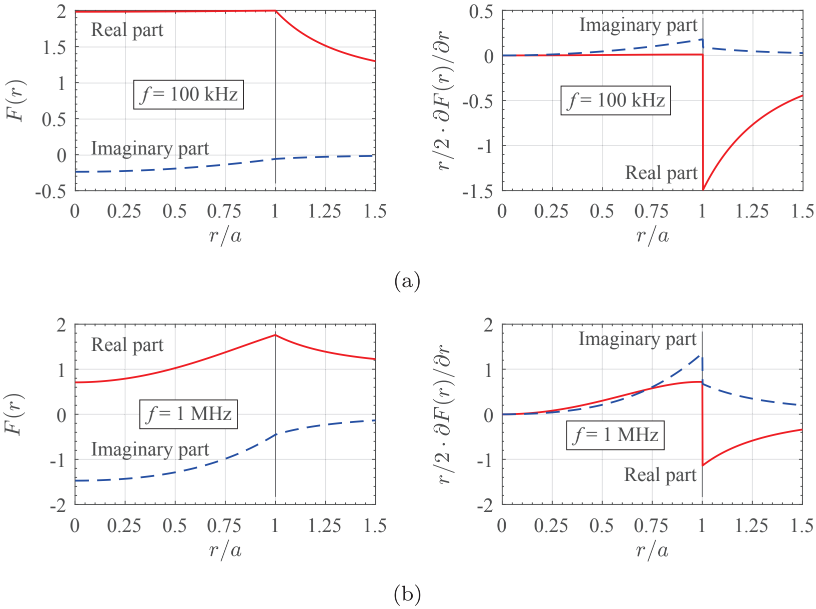

Figure 4.2: Real and imaginary parts of the scaling functions $F(r)$ and $r/2{\cdot}\partial F(r)/\partial r$ for a slip frequency of 100 kHz (a) and 1 MHz (b).

4.1.5 Current Density Inside the Rotor

Similar to the magnetic flux density, the current density inside the rotor can be obtained from the magnetic vector potential by using (4.14) as

$$\vec{J} = -\frac{1}{2} B_0 \sigma \omega r \,\mathrm{Re}\left\{ F(r) \begin{pmatrix} 0 \\ -\cos\varphi - \sin\varphi \\ -\cos\theta(j\cos\varphi - j\sin\varphi) \end{pmatrix} \cdot \begin{pmatrix} \vec{e}_r \\ \vec{e}_\theta \\ \vec{e}_\varphi \end{pmatrix} e^{j\omega t} \right\}. \tag{4.27}$$

The resulting current density distributions inside the rotor are shown in Fig. 4.5 for the same conditions as used in Fig. 4.3. The current densities describe current loops inside the rotor, for which $\vec{J}$ is directed perpendicular to the xy-plane. The direction of the current flow in these loops has been marked in the plots of the top row. Similar to the flux density, the current density is increasingly concentrated at the rotor surface for high

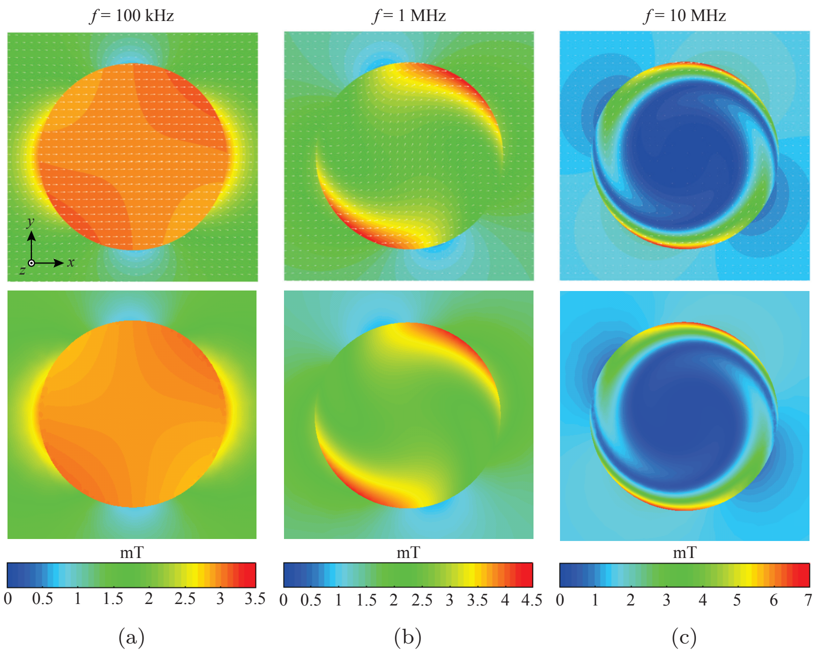

Figure 4.3: Magnitude of the magnetic flux density inside and in the vicinity of the rotor cut through the xy-plane ($z = 0$) at slip frequencies of 100 kHz (a), 1 MHz (b), and 10 MHz (c). Images in the top row were obtained by using the presented model, while those in the bottom row show results of 3D FEM eddy current simulations.

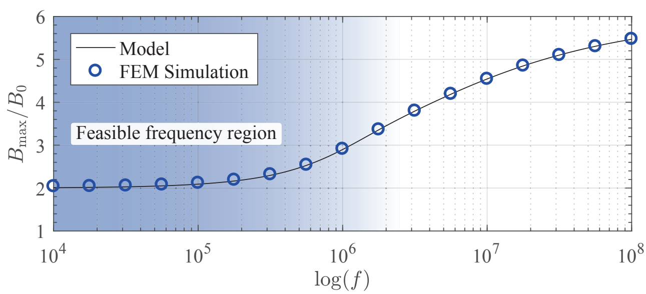

Figure 4.4: Ratio of the maximum occurring magnetic flux density inside the sphere and B_0 depending on the slip frequency.

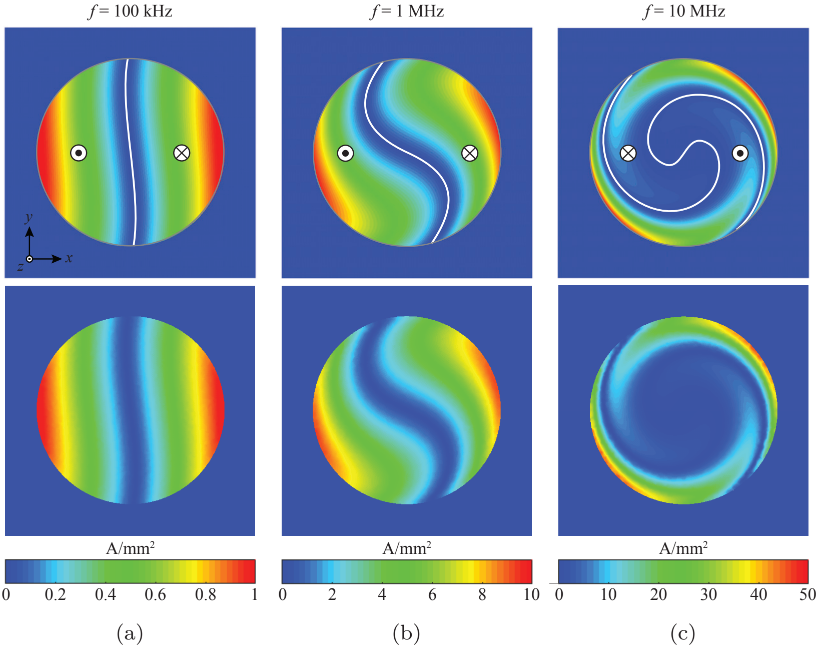

Figure 4.5: Magnitude of the current density inside the rotor cut through the xy-plane ($z = 0$) at slip frequencies of 100 kHz (a), 1 MHz (b), and 10 MHz (c). Images in the top row were obtained by using the presented model, while those in the bottom row show results of 3D FEM eddy current simulations. The direction of the current flow is marked in the plots of the top row.

slip frequencies. Again, comparison of the calculated results with those obtained by simulations shows an excellent agreement.

The flux density as well as the current density exhibit their maximum values along the circumference of the rotor at an azimuthal angle that increases with the slip frequency.

4.2 Motor Torque

The motor torque acting on the sphere originates from the interaction of the magnetic flux density with the eddy current density, which results in a Lorentz force $\vec{F} = \vec{J} \times \vec{B}$. The overall motor torque is obtained by integrating the torque per volume $d\vec{T} = \vec{r} \times (\vec{J} \times \vec{B})$ as

$$\vec{T}_\mathrm{m} = \int_0^{2\pi} \int_0^{\pi} \int_0^{a} \vec{r} \times \left(\vec{J} \times \vec{B} \right) r^2 \sin\theta \mathrm{d}r \mathrm{d}\theta \mathrm{d}\varphi. \tag{4.28}$$

Alternatively, the rotor can be treated as a magnetic dipole with moment $\vec{m}$, from which the torque is equivalently calculated as

$$\vec{T}_\mathrm{m} = \vec{m} \times \vec{B}_0. \tag{4.29}$$

The magnetic vector potential and the dipole moment are related by

$$\vec{A} = \frac{\mu_0}{4\pi} \frac{\vec{m} \times \vec{r}}{r^3}, \tag{4.30}$$

from which the magnetic dipole moment for the considered setup is obtained as (cf. [82])

$$\vec{m} = \frac{2\pi}{\mu_0} a^3 B_0 \mathrm{Re} \left\{ F(a) \begin{pmatrix} 1 \\ j \\ 0 \end{pmatrix} \cdot \begin{pmatrix} \vec{e}_x \\ \vec{e}_y \\ \vec{e}_z \end{pmatrix} \right\}, \tag{4.31}$$

with the resulting torque

$$\vec{T}_\mathrm{m} = -B_0 m_y \vec{e}_z. \tag{4.32}$$

The negative sign in (4.32) originates from the statement of the problem, which considered a sphere rotating with angular slip frequency ω with respect to a standing magnetic field (cf. Sec 4.1.1). Consequently, the resulting torque is a breaking torque, which is identical in magnitude to the drive torque that is obtained for a magnetic field exceeding the rotational frequency of the sphere by the same value. As a result, the motor torque is considered to have a positive value in the subsequent considerations, causing an acceleration of the rotor in the counterclockwise direction. The resulting torque characteristic for the parameters listed in Table 4.1 is shown in Fig. 4.6.

From (4.31) and (4.32), it can be seen that the motor torque scales quadratically with B_0 and cubically with a. Neglecting the occurring

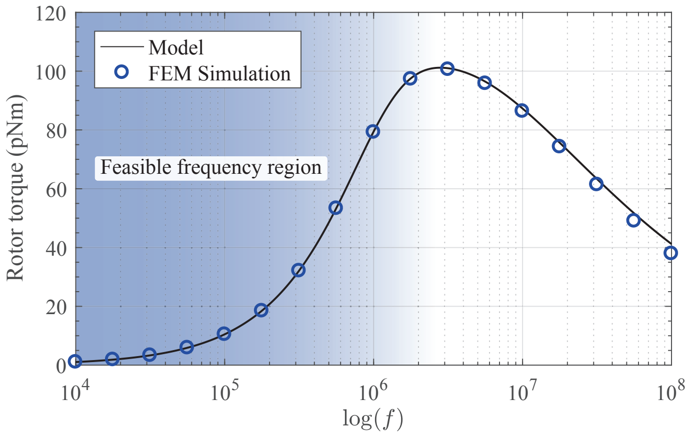

Figure 4.6: Torque characteristic depending on the slip frequency f as obtained by the presented model and 3D FEM simulations.

drag torques, the angular acceleration of the rotor is obtained as

$$\dot{\omega}_{\mathrm{r}} = \frac{T_{\mathrm{m}}}{I}, \tag{4.33}$$

where the moment of inertia I of a sphere is given as

$$I = \frac{2}{5} m a^2 = \frac{8}{15} \pi \rho a^5. \tag{4.34}$$

As this scales with the rotor radius to the power of five, the acceleration rate is expected to scale with $1/a^2$.

Interaction with Radial Magnetic Bearing

Based on the outlined model, it is possible to study the interaction of the drive and radial AMB discussed in Chapter 3. Due to this AMB, the magnetic field at the rotor consists of two components, namely, a rotating one for torque generation and a stationary one for bearing force generation. Aside from the desired reluctance force in the radial direction, the latter also results in an undesired breaking torque. The magnitude

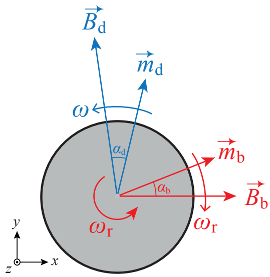

Figure 4.7: Flux density components and magnetic dipole moments as generated by the drive (blue) and radial magnetic bearing (red).

of this torque is obtained by considering the dipole moments as caused by the magnetic drive and bearing fields separately, as schematically illustrated in Fig. 4.7. The rotor is considered to rotate with mechanical angular frequency ω_r in the counterclockwise direction. With respect to the rotor, the spatially stationary magnetic flux density $\vec{B}_\text{b}$ as generated by the AMB rotates in the clockwise direction with the same angular frequency. Due to the mechanical rotation, the resulting magnetic dipole moment $\vec{m}_\text{b}$ leads $\vec{B}_\text{b}$ by a slip angle α_b. In addition, the magnetic flux density $\vec{B}_\text{d}$ of the drive spins with the angular slip frequency ω with respect to the rotor. As this field rotates faster than the sphere to generate a motor torque, the related magnetic dipole moment $\vec{m}_\text{d}$ lags the flux density by the slip angle α_d. Using (4.32), the resulting torques are obtained as

$$\vec{T}_\text{d} = B_\text{d} m_{\text{d},y} \vec{e}_z \tag{4.35}$$

and

$$\vec{T}_\text{b} = -B_\text{b} m_{\text{b},y} \vec{e}_z. \tag{4.36}$$

Aside from these torque components, two additional components exist due to the interaction of $\vec{m}_\text{d}$ with $\vec{B}_\text{b}$ and $\vec{m}_\text{b}$ with $\vec{B}_\text{d}$. As the vectors within these pairs rotate with different frequencies, the resulting torque components have zero average value and cause a pulsation of the torque with the angular frequency of the drive field $\omega_\text{d} = \omega_\text{r} + \omega$. The components can be written as

$$\vec{T}_\text{bd} = \vec{m}_\text{d} \times \vec{B}_\text{b} = B_\text{b} \left[m_{\text{d},x} \sin(\omega_\text{d} t) - m_{\text{d},y} \cos(\omega_\text{d} t) \right] \vec{e}_z \tag{4.37}$$

and

$$\vec{T}_{\mathrm{db}} = \vec{m}_{\mathrm{b}} \times \vec{B}_{\mathrm{d}} = B_{\mathrm{d}} \left[m_{\mathrm{b},x} \sin(\omega_{\mathrm{d}} t) - m_{\mathrm{b},y} \cos(\omega_{\mathrm{d}} t) \right] \vec{e}_z . \tag{4.38}$$

Due to the respective slip angles, a phase shift of these torque components exists, which is accounted for by considering the x and y components of the magnetic dipole moments separately. The overall torque acting on the rotor is calculated as the sum of all torque components. Due to the passively stable design in the axial direction, stabilization of the rotor by the radial AMB is only necessary for short time intervals during operation of the motor. Consequently, $\vec{B}_{\mathrm{b}}$ is only present during such instants under normal operating conditions, resulting in an uncritical temporary decrease of the acceleration rate of the rotor.

4.3 Rotor Losses

Ohmic eddy current losses occur inside the rotor, due to the finite conductivity of its material. The overall rotor losses are obtained by integrating the loss density $p_{\mathrm{ec}} = \vec{J}^2/\sigma$ over the volume of the sphere as

$$P_{\mathrm{ec}} = \int_0^{2\pi} \int_0^{\pi} \int_0^{a} p_{\mathrm{ec}} \; r^2 \sin\theta \mathrm{d}r \mathrm{d}\theta \mathrm{d}\varphi . \tag{4.39}$$

These losses rise quadratically with the slip frequency in the region of its feasible values (cf. (4.27)) and are shown in Fig. 4.8. For the considered spherical rotors, the losses scale with the the radius to the power of five. However, the amount of energy that can be dissipated from the rotor scales with its surface area and, therefore, only quadratically with the radius. The resulting thermal limit constrains the attainable motor torque and rate of acceleration, especially for larger rotors.

4.4 Windage Losses

Windage losses due to the relative velocity between the spinning rotor and the stationary medium (gas) in its surroundings generate a drag torque that counteracts the motor torque obtained in Section 4.2. Other

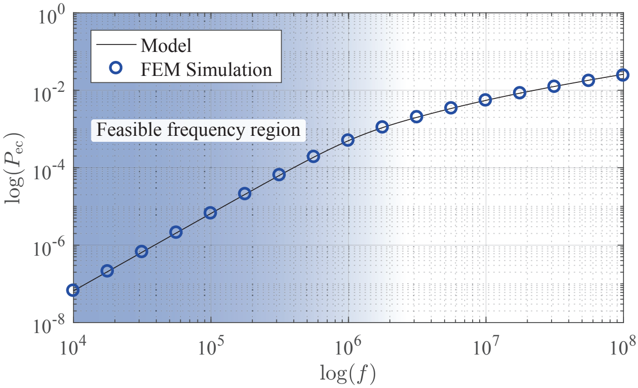

Figure 4.8: Ohmic eddy current losses inside the rotor depending on the slip frequency.

losses, such as bearing friction, are at very low levels due to magnetic suspension of the rotor. Consequently, the minimum motor torque has to be high enough to overcome the windage losses at the desired rotational speed. For a detailed assessment, models for the drag torques under various pressure conditions are required and presented in this section.

4.4.1 Gas Flow Regimes

The physical mechanisms governing drag torque generation due to windage losses depend on the considered gas flow regime. To determine the prevalent nature of the gas, the mean free path is used as a characteristic value. It represents the average distance a gas particle travels between two successive collisions and depends on the statistical motion of the particles. Its value is calculated as

$$\lambda = \frac{k_{\mathrm{B}}\vartheta}{\sqrt{2}\pi p d_{\mathrm{m}}^2}, \tag{4.40}$$

where k_{B}, ϑ, p, and d_{m} denote the Boltzmann constant, the absolute temperature in Kelvin, the pressure, and the molecular diameter, respectively. The corresponding flow regime is obtained by relating the mean free path to the size of the considered geometries. This ratio is referred

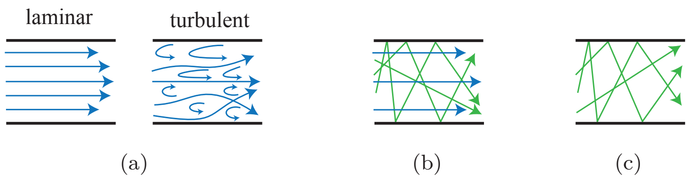

Figure 4.9: Overview of gas flow regimes, (a) continuum flow, (b) slip flow, and (c) free molecular flow.

to as the Knudsen number

$$\mathrm{Kn} = \frac{\lambda}{l} = \frac{\lambda}{a}, \tag{4.41}$$

where the radius of the spherical rotor serves as the characteristic dimension l of the considered system [92]. Under atmospheric pressure conditions (1.01×10^5 Pa) at room temperature, λ is in the range of 10^{-8} m, which is much smaller than the dimensions of the considered geometries, resulting in $\mathrm{Kn} < 0.01$. Consequently, the occurring gas flow is characterized by collisions of gas molecules among each other. This flow is referred to as continuum flow and is modeled using a continuum mechanical approach. It can be subdivided into being fully laminar, fully turbulent, or in an intermediate state. As the pressure is lowered (medium vacuum range), λ increases and the nature of the gas becomes more and more ambiguously determined by a combination of gas-to-gas and gas-to-wall interactions. The flow in this transition regime is commonly referred to as slip flow for $0.01 < \mathrm{Kn} < 0.1$ and transition or Knudsen flow for $0.1 < \mathrm{Kn} < 10$ ($\lambda \approx l$) in the literature [93, 94]. Modeling of drag torques in this region is difficult due to the indefinite nature of the gas flow and a common approach is to use interpolated models from other flow regimes. At low pressures in the high vacuum range, the mean free path becomes large compared to the size of the considered geometry and the nature of the gas is determined by gas-to-wall interactions. This situation is referred to as free molecular flow and is treated by means of statistical mechanics. An overview of the considered gas flow regimes is provided in Fig. 4.9. To provide a point of reference for the prevalent nature of the gas flow for a submillimeter-size rotor ($a \leq 0.5$ mm) over a wide range of gas pressures, air ($d_\mathrm{m} \approx 3.87 \times 10^{-10}$ m) is considered as the surround-

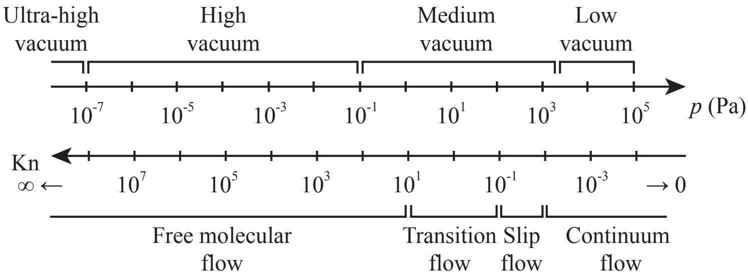

Figure 4.10: Vacuum qualities and Knudsen numbers with associated flow regimes for submillimeter-size rotors.

ing medium at a temperature of 25 °C (298.15 K). The resulting vacuum conditions, Knudsen numbers, and flow regimes are shown in Fig. 4.10. It can be seen that a pressure of $\sim 10^{-1}$ Pa is sufficiently low to attain free molecular flow conditions, due to the small rotor size.

4.4.2 Drag Torques

Subsequently, analytical models for the occurring drag torques in the various gas flow regimes are presented. Together with the heat transfer considerations presented in Section 4.5, the most suitable flow regime for attaining ultra-high rotational speeds is identified.

Continuum Flow

In this regime, further subdivision of the nature of the gas flow is necessary to obtain a solution for the drag torque. To determine whether the flow is laminar viscous or turbulent (cf. Fig. 4.9(a)), the Reynolds number

$$\mathrm{Re} = \frac{\rho v l}{\mu} = \frac{\rho a^2 \omega}{\mu} \tag{4.42}$$

is used, where ρ, v, and μ denote the density of the fluid, its relative velocity to the object, and its dynamic viscosity, respectively. The latter is given as

$$\mu = \frac{1}{2}\rho\bar{c}\lambda, \tag{4.43}$$

where $\overline{c}$ is the mean thermal molecular speed of the gas, which is obtained based on the Maxwell-Boltzmann distribution [93] as

$$\overline{c} = \sqrt{\frac{8k_{\mathrm{B}}T}{\pi m}}, \tag{4.44}$$

where $m = M/N_{\mathrm{A}}$ is the mass of a single molecule, which is obtained by dividing the molar mass M by the Avogadro constant N_{A}. For air at $25\,^{\circ}\mathrm{C}$, this yields a value of $\overline{c} = 466.9\,\mathrm{m/s}$. The value of Re at which the transition from laminar to turbulent flow occurs depends on the geometry and nature of relative motion (linear, rotating) and is often determined experimentally. In addition, the Mach number

$$\mathrm{Ma} = a\omega/c, \tag{4.45}$$

which relates the obtained circumferential speed to the speed of sound c in the medium, has to be considered to obtain a model for the drag torque.

The windage losses occurring for a sphere with smooth surface rotating at constant angular velocity was analyzed over a wide range of Reynolds numbers in [95]. The investigations in this study are based on the following assumptions:

(a) The fluid is incompressible with constant density ρ, which usually necessitates $\mathrm{Ma} << 1$

(b) The viscosity μ is constant

(c) The considered fluid is a Newtonian fluid, yielding a linear proportionality of the viscous stress to the strain rate.

Due to the small rotor radii, the occurring Reynolds numbers are limited to values below $\sim 30\,000$, which suggests that a laminar boundary layer around the sphere exists for all attainable rotational speeds based on the mechanical strength of the rotor. Up to these Reynolds numbers, the nature of the flow can be subdivided into three regions.

For $0 < \mathrm{Re} \lesssim 10$, laminar creeping flow conditions apply. The solution of the Navier-Stokes equation [96] for this case yields an angular velocity for the fluid at a distance r from the center of the sphere of

$$\omega_{\mathrm{f}} = \frac{a^3\omega}{r^3} \tag{4.46}$$

and a drag torque of

$$T_1 = 8\pi\mu a^3\omega. \tag{4.47}$$

For $10 < \mathrm{Re} < 1\,000$, the transition from an entirely laminar creeping flow to a laminar boundary layer flow occurs. Over this range, the laminar flow region is restricted to a layer of decreasing thickness δ around the surface of the sphere. Several solutions have been proposed in the literature specifically for this region. It was found in [95] that the drag torques obtained by (4.47) are in good agreement with experimental results up to $\mathrm{Re} \approx 50$. Above this value, a corrected version of the solution for the subsequent region as obtained in [97] can be used, yielding

$$T_{1\to 2} = 3.27(\rho\mu)^{\frac{1}{2}} a^4 \omega^{\frac{3}{2}} + \frac{8}{3}\pi\mu a^3\omega. \tag{4.48}$$

In the region $1\,000 < \mathrm{Re} < 40\,000$, a laminar boundary layer around the sphere is present and governs the generation of the drag torque, while turbulent flow occurs further away. The solution for the drag torque

$$T_2 = 3.27(\rho\mu)^{\frac{1}{2}} a^4 \omega^{\frac{3}{2}} \tag{4.49}$$

as obtained in [97], which takes into account that δ varies across the degree of latitude of the sphere, can be used.

The outlined models for the various regions were found to be within 4 % of measured values, except for small regions of intermediate Reynold numbers [95]. In theory, Mach numbers > 1 could be obtained at the desired rotational speeds, for which assumption (a) would no longer be valid. This was analyzed in [98], suggesting that the general form of the drag torque

$$T = A(\rho\mu)^{\frac{1}{2}} a^4 \omega^{\frac{3}{2}} \tag{4.50}$$

(cf. (4.49)) as obtained in [99], where A is an empirical constant, may be extended to the case of a compressible fluid.

It should be noted that the presented results assume a sphere rotating in an infinite fluid. In experiments, the fluid is usually bounded by a container that affects the flow. However, as the drag torque only depends on the flow in the boundary layer immediately in contact with the rotor surface, for which $\delta << a$ holds, a containment is expected to have a negligible effect as long as it is sufficiently far away from the rotor. This

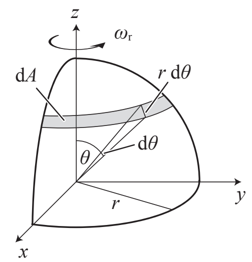

Figure 4.11: Geometry used for analytical calculation of the drag torque under free molecular flow conditions.

was experimentally verified in [98]. Effects related to static walls in the vicinity of the rotor have been analyzed in [100, 101] for some particular geometries.

Free Molecular Flow

In contrast to continuum flow conditions, no further subdivision of this regime is necessary and a model for the drag torque can be obtained from analytical considerations [94]. Due to the large mean free path compared to the dimensions of the considered geometries, molecules moving away after contact with the rotating sphere do not interact with incoming molecules.

A visualization of the following derivations is provided in Fig. 4.11. For a gas of pressure $p = nk_\mathrm{B}\vartheta$ with particle number density n, the particle flow onto each surface area element $\mathrm{d}A$ of the rotor is given as

$$\mathrm{d}q_N = \frac{n\bar{c}}{4}\mathrm{d}A. \tag{4.51}$$

Upon contact with the rotor, a gas particle receives the linear momentum $\sigma_\mathrm{t} m v_\mathrm{t}$, where σ_t denotes the tangential-momentum accommodation coefficient (see below). The tangential velocity of the surface element $\mathrm{d}A$ of the sphere is given as $v_\mathrm{t} = \omega_\mathrm{r} a \sin\theta$. Based on the law of the conservation of momentum, the retarding force acting on the surface element is obtained as

$$\mathrm{d}F = \frac{1}{4}\rho\bar{c}\sigma_\mathrm{t}\omega_\mathrm{r} a \sin\theta \mathrm{d}A. \tag{4.52}$$

Using $\mathrm{d}T = a \sin\theta \mathrm{d}F$ and $\mathrm{d}A = 2\pi a^2 \sin\theta \mathrm{d}\theta$, the overall drag torque acting on the rotor is obtained by integration as

$$T_{\mathrm{fm}} = \int_0^{\pi} \frac{1}{2} \rho \bar{c} \sigma_{\mathrm{t}} \omega_{\mathrm{r}} \pi a^4 \sin^3\theta \mathrm{d}\theta = \frac{2}{3} \rho \bar{c} \sigma_{\mathrm{t}} \omega_{\mathrm{r}} \pi a^4. \tag{4.53}$$

This can equivalently be written in terms of the pressure as

$$T_{\mathrm{fm}} = \frac{16}{3\bar{c}} \sigma_{\mathrm{t}} a^4 \omega_{\mathrm{r}} p. \tag{4.54}$$

As $T_{\mathrm{fm}} \propto p$, the deceleration rate of a spinning sphere that is suspended with low frictional torque can be used for pressure measurements. Such a setup is referred to as a spinning rotor pressure gauge [86, 94, 102, 103].

The dimensionless tangential-momentum accommodation coefficient σ_{t} used in the previous equations represents a measure for how close scattering of gas molecules at the rotor surface is to the case of ideally diffuse scattering governed by the cosine law [104]. For the technically smooth surfaces of the considered spheres, the value of σ_{t} has been found to be ≈ 1. Detailed models for determining σ_{t} are provided in [94, 105–107], and need to be taken into account in case of a rough rotor surface or if high precision of the results is required, such as in vacuum gauge devices.

Slip and Transition Flow

Due to the indefinite nature of the gas flow in this region, the formulation of an analytical model for the drag torque based on first principles is difficult. An approximate method for obtaining a solution for the transition regime is described in [108]. The approach is based on the assumption that (4.46) and (4.47) are valid in this regime with altered boundary conditions, such that the angular velocity of the gas $\omega_{\mathrm{f}}(r)$ at radius a does not have to be equal to that of the rotor surface ω_{r} to allow for slip. As the gas molecules approach the surface of the sphere from different parts of the flow field, they exhibit variable characteristics. It is supposed that a fraction

$$\mathrm{d}N = \frac{1}{\lambda} e^{(a-r)/\lambda} \mathrm{d}r \tag{4.55}$$

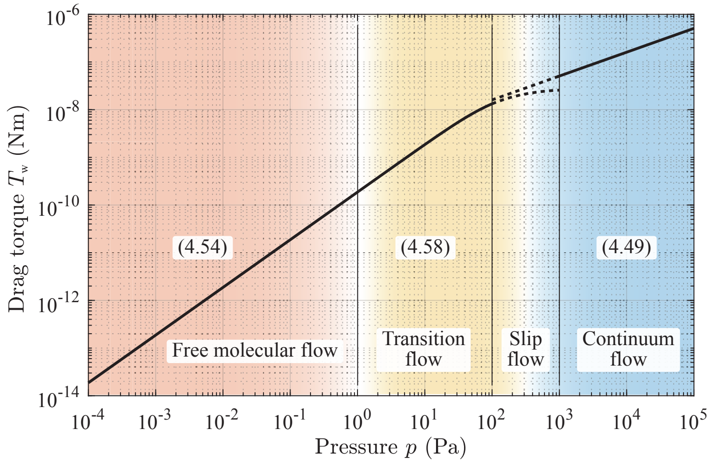

Figure 4.12: Drag torque for a spherical rotor with radius $a = 0.25\,\mathrm{mm}$ rotating at $n = 40\,\mathrm{Mrpm}$ surrounded by air at various pressures.

of the molecules had its last collision with another gas molecule within the spherical shell with inner radius r and outer radius $r + \mathrm{d}r$ [109]. Based on (4.53), the drag torque resulting from these molecules is obtained as

$$\mathrm{d}T = \frac{2}{3}\rho\bar{c}\sigma_{\mathrm{t}}\pi a^4[\omega_{\mathrm{r}} - \omega_{\mathrm{f}}(r)]\mathrm{d}N. \tag{4.56}$$

The overall torque is calculated by integration as

$$T = \int_{r=a}^{\infty} \mathrm{d}T = \frac{2}{3\lambda}\rho\bar{c}\sigma_{\mathrm{t}}\pi a^4 \int_a^{\infty} [\omega_{\mathrm{r}} - \omega_{\mathrm{f}}(r)]e^{(a-r)\lambda}\mathrm{d}r, \tag{4.57}$$

which is conveniently expressed as the ratio

$$\frac{T_{\mathrm{fm}}}{T} = \frac{1}{\sigma_{\mathrm{t}}} + \frac{a}{6\lambda}G_3\left(\frac{a}{\lambda}\right) \quad \text{with} \quad G_3(x) = x^3 e^x \int_x^{\infty} \frac{1}{t^3}e^{-t}\mathrm{d}t, \tag{4.58}$$

where a/λ can be replaced by the reciprocal of the Knudsen number according to (4.41).

To compare the drag torque across the various regimes, numerical values are calculated from the presented models for a sphere with $a =$

0.25 mm rotating at $n = 40$ Mrpm in air at variable pressure. The result is shown in Fig. 4.12. The drag torque T_w can be reduced from the range of µNm at atmospheric pressure and low vacuum conditions to well below pNm under high vacuum conditions. The minimum required motor torque is expected to be of the same order of magnitude, based on which the entailed rotor loss power can be obtained (see Section 4.3). The associated windage loss power is given as

$$P_\mathrm{w} = T_\mathrm{w}\omega_\mathrm{r}, \tag{4.59}$$

which is in the range of watts for atmospheric pressure conditions and below the µW range for high vacuum conditions. To assess the resulting rotor temperature, the heat transfer between the rotor and its surroundings needs to be studied as it limits the dissipation of losses.

4.5 Heat Transfer

Heat transfer between the rotor and its environment takes place by convection, conduction, and radiation. Convective heat transfer is closely related to the flow condition as assessed in the previous section and the same division based on the nature of the surrounding gas flow is applicable.

The subsequently presented heat transfer models consider the spherical rotor to have a uniform temperature distribution. This assumption is well justified due to the small size of the rotor and the low thermal resistance of its material with respect to the thermal resistance between the rotor surface and its surroundings.

4.5.1 Convection and Conduction

Continuum Flow

In the case of continuum flow, the heat transfer between the sphere and the surrounding fluid is mainly caused by convection, for which the general heat transfer rate is given as

$$\dot{Q}_\mathrm{conv} = \bar{h}_\mathrm{c} A_\mathrm{r}(\vartheta_\mathrm{r} - \vartheta_\mathrm{a}), \tag{4.60}$$

where $\bar{h}_\mathrm{c}$, A_r, ϑ_r, and ϑ_a denote the average heat transfer coefficient, the surface area of the rotor, the rotor temperature, and the ambient temperature, respectively. The value of $\bar{h}_\mathrm{c}$ depends on Re and is commonly substituted by the dimensionless Nusselt number

$$\mathrm{Nu} = \frac{2ah_\mathrm{c}}{k_\mathrm{f}}, \tag{4.61}$$

where h_c and k_f denote the unit surface convective heat transfer coefficient of the rotating sphere and the thermal conductivity of the fluid, respectively. Here, the diameter of the sphere ($2a$) has been used as the characteristic length of the considered geometry. Therefore, the Nusselt number expresses the ratio of heat transfer due to convection and the hypothetical heat transfer due to conduction that would occur in a resting fluid. Due to the curved surface of the sphere and the resulting variation of the fluid boundary layer thickness, h_c depends on the considered surface element. Consequently, (4.61) provides a value for the local Nusselt number. To obtain the overall heat transfer between the sphere and the environment, the average heat transfer coefficient is calculated as

$$\bar{h}_\mathrm{c} = \frac{1}{A_\mathrm{r}} \iint\limits_{A} h_\mathrm{c}(\theta, \varphi)\mathrm{d}A. \tag{4.62}$$

Using this value in (4.61) yields the average Nusselt number $\overline{\mathrm{Nu}}$.

Besides the considered geometry, the convective heat transfer rate also depends on the characteristics of the surrounding fluid, which are assessed by the Prandtl number

$$\mathrm{Pr} = \frac{c_p \mu}{k_\mathrm{f}}, \tag{4.63}$$

where c_p is the specific heat at constant pressure. The Prandtl number represents the ratio of the viscous diffusion rate and the thermal diffusion rate of a fluid, which is ≈ 0.71 for air under atmospheric pressure conditions.

Due to the rotation, the heat transfer is determined by forced convection while free convection effects are negligible [110]. Therefore, it is possible to express the average Nusselt number as a function of Re and Pr. Such a function was obtained empirically for a rotating sphere in

[110]. For the aforementioned value of Pr, it was found that

$$\overline{\mathrm{Nu}} = \begin{cases} 0.43\,\mathrm{Re}^{0.5}\,\mathrm{Pr}^{0.4} & \text{for } \mathrm{Re} \leq 5 \times 10^5 \\ 0.066\,\mathrm{Re}^{0.67}\,\mathrm{Pr}^{0.4} & \text{for } 5 \times 10^5 < \mathrm{Re} < 7 \times 10^6. \end{cases} \tag{4.64}$$

Free Molecular Flow

For the free molecular flow region, a similar derivation as carried out in Section 4.4.2 yields

$$\dot{Q}_{\mathrm{fm}} = \frac{1}{2} p \bar{c} \alpha_{\mathrm{th}} \pi a^2 \frac{\gamma + 1}{\gamma - 1} \left(\frac{\vartheta_{\mathrm{r}}}{\vartheta_{\mathrm{a}}} - 1 \right), \tag{4.65}$$

which is referred to as the free molecular heat conduction, where γ denotes the heat capacity ratio $\gamma = c_p/c_v$ and c_v is the specific heat at constant volume [111, 112]. The thermal accommodation coefficient α_{th} is a measure for the energy carried away by gas molecules leaving the rotor surface. Values of $\alpha_{\mathrm{th}} = 0.87 - 0.95$ are found in the literature for polished metal surfaces and air as a gas [113].

Slip and Transition Flow

Similar to the drag torque, an expression for the heat transfer in this region can be obtained by interpolation between the continuum and the free molecular limit. To obtain the continuum limit, the heat transfer by conduction between two concentric spheres is used, where the radius of the outer sphere is chosen to go to infinity, yielding

$$\dot{Q}_{\mathrm{c}} = 4\pi k_{\mathrm{f}} a \vartheta_{\mathrm{r}}. \tag{4.66}$$

Based on this result, the heat transfer rate in the slip and transition regime is found as [108]

$$\frac{\dot{Q}_{\mathrm{fm}}}{\dot{Q}} = \frac{1}{\alpha_{\mathrm{th}}} + \frac{a}{2\lambda^*} G_1\left(\frac{a}{\lambda^*}\right) \quad \text{with} \quad G_1(x) = xe \int_x^\infty \frac{1}{t} e^{-t} \mathrm{d}t, \tag{4.67}$$

where λ^* is the heat-conduction mean free path defined as

$$\lambda^* = \frac{4k_\mathrm{f}}{(\gamma+1)c_v\rho\bar{c}}. \tag{4.68}$$

4.5.2 Radiation

Besides the aforementioned heat transfer mechanisms of conduction and convection, heat is also transferred between the rotor and its surroundings by means of thermal radiation, independent of the flow regime. The rate of radiation from a surface with temperature ϑ_r is given by the Stefan-Boltzmann law as

$$\dot{Q}_\mathrm{rad} = \epsilon_\mathrm{r}\sigma_\mathrm{B}A_\mathrm{r}\vartheta_\mathrm{r}^4, \tag{4.69}$$

where ϵ_r denotes its emissivity and σ_B is the Stefan-Boltzmann constant. For a polished steel surface such as that of the rotor $\epsilon \approx 0.1$ holds. The net radiative heat transfer between the rotor surface and its surroundings is obtained by considering the difference between the radiation leaving the rotor surface and that arriving from the environment. The resulting heat transfer is obtained as

$$\dot{Q}_\mathrm{rad} = \frac{\sigma_\mathrm{B}\left(\vartheta_\mathrm{r}^4 - \vartheta_\mathrm{a}^4\right)}{\frac{1-\epsilon_\mathrm{r}}{A_\mathrm{r}\epsilon_\mathrm{r}} + \frac{1}{A_\mathrm{r}F_{r\to a}} + \frac{1-\epsilon_\mathrm{a}}{A_\mathrm{a}\epsilon_\mathrm{a}}}, \tag{4.70}$$

where ϵ_a and A_a denote the emissivity and surface area of the surroundings, respectively [114]. $F_{r\to a}$ denotes the view factor from the rotor surface to its ambient surfaces. As the rotor is fully enclosed by the vacuum tube, the view factor is equal to one. Moreover, $A_\mathrm{a} >> A_\mathrm{r}$ holds, for which (4.70) simplifies to

$$\dot{Q}_\mathrm{rad} = \epsilon_\mathrm{r}\sigma_\mathrm{B}A_\mathrm{r}\left(\vartheta_\mathrm{r}^4 - \vartheta_\mathrm{a}^4\right). \tag{4.71}$$

The total heat transfer from the rotor is given as

$$\dot{Q} = \dot{Q}_\mathrm{conv} + \dot{Q}_\mathrm{rad}. \tag{4.72}$$

While convective heat transfer dominates at high pressures, the majority of heat is transferred by radiation at pressures in the high vacuum range.

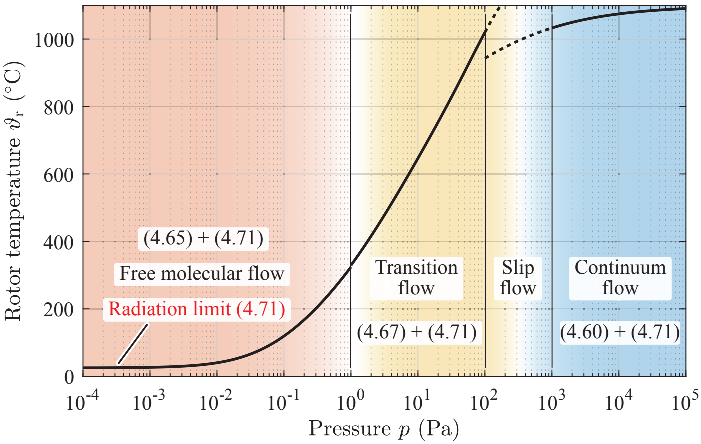

Figure 4.13: Calculated rotor temperature for $T_m = T_w$ and a spherical rotor with radius $a = 0.25$ mm rotating at $n = 40$ Mrpm surrounded by air at various pressures.

Radiative heat transfer increases rapidly for high rotor temperatures due to its biquadratic dependency.

4.6 Rotor Temperature

Using the presented heat transfer models, the expected rotor temperature can be obtained based on the power balance

$$P_{ec} = \dot{Q}_{fm} + \dot{Q}_{rad}. \tag{4.73}$$

Setting $T_m = T_w$ corresponds to the case for which the windage losses are exactly compensated by the motor power and yields $P_{ec} = P_w$, if other losses are neglected. Using the windage loss power from Section 4.4.2, the expected rotor temperature can be obtained as shown in Fig. 4.13. Despite a high rate of energy transfer, this temperature would exceed 1000 °C under atmospheric pressure conditions, due to the high required motor torque. This is not attainable in practice, as the UTS of the rotor material would be significantly lowered by the high temperature, as discussed in Chapter 2. As the required motor torque drops significantly at lower pressures, the expected rotor temperature decreases, despite a lowered heat transfer rate. The latter drops less rapidly than the drag torque because of the pressure-independent heat transfer by thermal radiation. The lowest rotor temperatures are, therefore, expected at pressures in the range of $\leq 10^{-2}$ Pa, where most of the heat transfer is due to radiation. Consequently, operation of the motor under such pressure conditions is necessary to achieve ultra-high rotational speeds.

The estimated rotor temperatures have to be considered as a lower limit, as all drag torques aside from that caused by gas friction have been neglected. In practice, the rotor temperature can be significantly higher, especially for high motor torques (high acceleration rates). Based on (4.39) and (4.71), an admissible operating range of f and B_0 for a defined maximum rotor temperature can be obtained. For the considered materials, the rotor temperature should be limited to below 150 °C at high rotational speeds to prevent weakening of the material. The rotor temperature is shown in Fig. 4.14 for different operating points and the admissible operating range has been marked. Only thermal radiation has been considered for the heat transfer between the rotor and its surroundings. Within this range, it is desirable to obtain as much torque as possible per temperature increase of the rotor. Therefore, the torque-to-temperature ratio

$$TTR = \frac{T_\mathrm{m}}{\vartheta_\mathrm{r}} \tag{4.74}$$

is introduced to determine the slip frequency $f_{TTR,\mathrm{max}}$ at which the highest motor torque per temperature increase of the rotor is generated. The results are displayed in Fig. 4.15 for a maximum rotor temperature of 150 °C and show that $f_{TTR,\mathrm{max}}$ rapidly decreases for an increase of B_0 and is mostly bound to values below 200 kHz. The TTR scales approximately linearly with B_0 in the considered region. This means that high torques are preferably attained by using a low current density inside the rotor and a high external magnetic flux density. For such operating conditions, losses mostly occur in the stator for which cooling is less critical. Based on the presented findings, the operating conditions can be chosen such that a high acceleration rate is attained while not exceeding a critical rotor temperature.

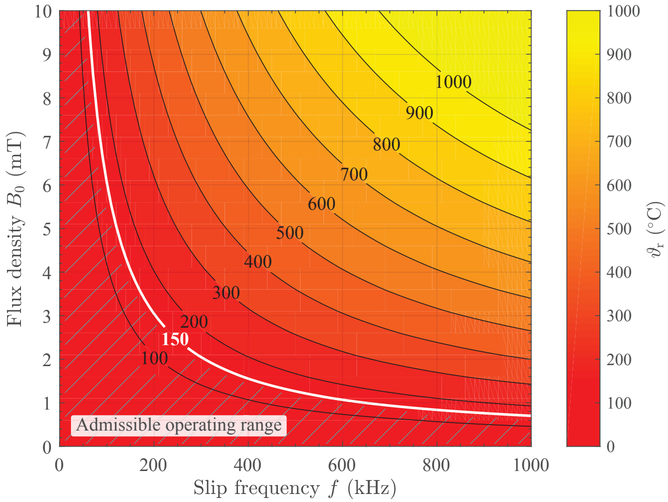

Figure 4.14: Rotor temperature depending on the slip frequency and external magnetic flux density (system parameters as listed in Table 4.1).

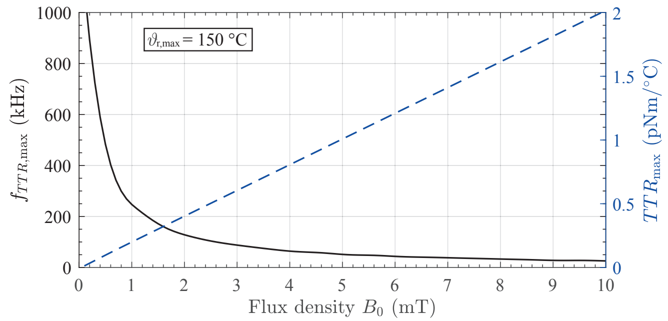

Figure 4.15: Slip frequency $f_{TTR,\max}$ and torque-to-temperature ratio depending on the external magnetic flux density B_0 for a maximum admissible rotor temperature of 150 °C (system parameters as listed in Table 4.1).

Chapter 5

Stator Design

To generate the magnetic field for driving the rotor, a suitable machine stator is necessary. The latter has to be designed for field frequencies in the megahertz range, which is significantly higher than the frequencies occurring in conventional electric machines.

At least two coils that are placed along two linearly-independent horizontal axes are required for generating a rotating magnetic field in the horizontal plane. However, such an arrangement results in additional undesired magnetic forces. These forces can be eliminated by using three coils, which are placed radially around the rotor at an angle of 120 ° apart. A rotating magnetic field is generated by shifting the phase of the impressed drive currents in the coils by 0 °, 120 °, and 240 °. To measure the position of the rotor in all translatory degrees of freedom, a sensor system consisting of multiple sensors is required. Preferably, these sensors

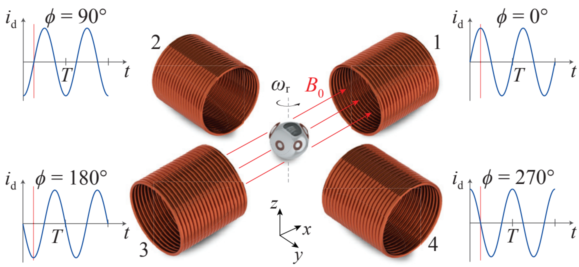

Figure 5.1: Generation of the rotating magnetic field for driving the rotor by four radially placed coils. The magnetic field is shown for the instant at which i_1 and i_3 reach their maximum and minimum values, respectively, while $i_2 = i_4 = 0$ as marked by the red line in the corresponding current waveforms.

should be placed apart by an angle of 90 °. However, this is impossible when using a stator consisting of three coils, as the desired space is occupied by windings. Consequently, an arrangement of four coils as show in Fig. 5.1 is used, which offers sufficient space for the sensors between the coils. The rotating magnetic field is generated by phase shifting the drive currents in the coils denoted by 1, 2, 3, and 4 by 0°, 90°, 180°, and 270°, respectively. In this chapter, possible stator designs are presented and analyzed. Based on the findings, a design consisting of four separate coils with ferromagnetic cores to guide the magnetic flux is chosen.

5.1 Drive Current Modulation

Due to the limited space around the rotor, a combined usage of the stator for drive torque and radial bearing force generation is desirable. This makes it necessary to superimpose the drive and bearing currents in the stator coils. To reach the desired ultra-high rotational speeds, field frequencies in the megahertz range are required. Due to these high frequencies, the generation of sinusoidal drive currents, e.g., by pulse-width modulation (PWM) [115], is not easily possible, as such modulation schemes require a significantly higher switching frequency of the employed power electronic converter. Generating a sinusoidal drive current by using a resonant coupling circuit consisting of the stator winding and a capacitor would be possible in principle. However, the drive frequency has to be adjustable over a wide range and the coil also has to carry the bearing current, which is in the range of several tens of hertz, depending on the rotor dynamics. Due to these large differences and variations of the frequency contents of the coil currents, an approach based on resonant coupling is not suitable. Instead, fundamental frequency modulation of the coil voltages is used (see Chapter 7).

Figure 5.2 shows the resulting voltage and current waveforms, which feature a rectangular and trapezoidal shape, respectively. The obtainable discrete voltage levels across the coils are $+V_{\mathrm{dc}}$, $-V_{\mathrm{dc}}$, and 0 V, where V_{dc} denotes the dc-link voltage. The coil current is directly related to the voltage across its terminals by

$$i_{\mathrm{c}}(t) = \frac{1}{L} \int v_{\mathrm{c}}(t)\mathrm{d}t, \tag{5.1}$$

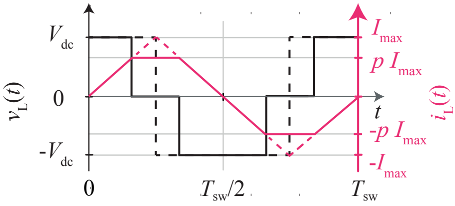

Figure 5.2: Output voltage (black) and current (red) for a full-bridge inverter using block commutation.

where the wire resistance has been neglected. Consequently, the achievable peak current magnitude is given as

$$I_{\mathrm{max}} = \frac{V_{\mathrm{dc}}}{4Lf_{\mathrm{sw}}}, \tag{5.2}$$

where f_{sw} denotes the switching frequency. By setting $v_{\mathrm{c}} = 0$ during intermediate time intervals between commutation from $+V_{\mathrm{dc}}$ to $-V_{\mathrm{dc}}$ and vice versa, the shape of the inductor current is altered such that the tip of the triangular current waveform is cut off and the maximum drive current is reduced to pI_{max}.

The model for the motor torque, which is presented in Section 4.2, is based on the assumption of an external magnetic flux density $\vec{B}_0$ rotating with a single angular frequency ω_0, which corresponds to purely sinusoidal drive currents. In order to employ the model in conjunction with the obtained non-sinusoidal drive currents, a Fourier series-based analysis is performed by individually assessing the contribution of each harmonic component to the torque generation. The waveform of the current is given in the normalized time domain as

$$i_{\mathrm{c}}(t) = \begin{cases} \frac{2I_{\mathrm{max}}}{\pi} t & t \in \left[0, p\frac{\pi}{2}\right] \\ pI_{\mathrm{max}} & t \in \left[p\frac{\pi}{2}, \left(1-\frac{p}{2}\right)\pi\right] \\ pI_{\mathrm{max}} - \frac{2I_{\mathrm{max}}}{\pi}\left[t - \left(1-\frac{p}{2}\right)\pi\right] & t \in \left[\left(1-\frac{p}{2}\right)\pi, \pi\right], \end{cases} \tag{5.3}$$

where $p \in (0, 1]$. This is equivalently represented by the Fourier series

$$x(t) = \frac{a_0}{2} + \sum_{k=1}^{\infty} \left[a_k \cos(k(\omega_0 t - \phi_0)) + b_k \sin(k(\omega_0 t - \phi_0)) \right], \tag{5.4}$$

where k, ω_0, and ϕ_0 denote the harmonic order, the fundamental angular frequency corresponding to $2\pi f_{\mathrm{sw}}$, and a phase shift angle, respectively. The current waveform has zero average value and is odd, resulting in $a_0 = 0$ and $a_k = 0$, respectively. The coefficients b_k are given as

$$b_k = \frac{4 I_{\max}}{(\pi k)^2} \left[\sin\left(kp \frac{\pi}{2} \right) - \sin(k\pi) - \sin\left(n(p-2) \frac{\pi}{2} \right) \right]. \tag{5.5}$$

A positive contribution of the k^{th} harmonic component to the overall torque is obtained if $b_k > 0$, corresponding to $\vec{B}_0$ rotating in the counterclockwise direction. Contrarily, components with $b_k < 0$ generate a decelerating torque. Considering $B \propto I$ yields

$$T_{\mathrm{m}} \propto \sum_{k=1}^{\infty} \mathrm{sgn}(b_k) \cdot b_k^2. \tag{5.6}$$

Altering the value of p by controlling the modulation accordingly (see Section 7.2.2) can, therefore, be used to control the motor torque and the occurring losses in the system within a certain region, as shown below.

5.2 Losses

Aside from losses in the actuator of the axial magnetic suspension system and eddy current losses inside the rotor, additional losses occur in the stator. The latter can be subdivided into coil and core losses. Subsequently, the respective loss models are discussed to provide a benchmark for the comparison of different stator topologies and to identify the most suitable one for the ultra-high-speed motor.

5.2.1 Copper Losses

Ohmic losses originate from the resistance R_c of the coil and can be obtained as

$$P_\mathrm{r} = \overline{p_\mathrm{r}(t)} = \frac{R_\mathrm{c}}{T_\mathrm{sw}} \int\limits_{t_0}^{t_0+T_\mathrm{sw}} i_\mathrm{c}^2(t)\mathrm{d}t. \tag{5.7}$$

These losses can equivalently be calculated based on the provided harmonic analysis as

$$P_\mathrm{r} = R_\mathrm{c} \cdot \sum_{k=1}^{\infty} \frac{b_k^2}{2}, \tag{5.8}$$

which makes it possible to analyze the contribution of each harmonic component.

The overall resistance R_c of the drive coil is comprised of its dc resistance R_dc and its ac resistance R_ac, where the latter is caused by the skin and proximity effects

$$R_\mathrm{c} = R_\mathrm{dc} + R_\mathrm{ac,skin} + R_\mathrm{ac,prox}. \tag{5.9}$$

R_dc is calculated as

$$R_\mathrm{dc} = \frac{4l}{\sigma_\mathrm{w} \pi d_\mathrm{w}^2}, \tag{5.10}$$

with l, σ_w, and d_w denoting the wire length, its conductivity, and its diameter, respectively. Detailed models for estimating the ac losses can be found in the literature [116–118]. At a frequency of 1 MHz, the skin depth is $\approx 6.6 \times 10^{-5}\,\mathrm{m}$ ($\sigma_\mathrm{Cu} = 58\,\mathrm{MS/m}$, $\mu = \mu_0$). For maximum utilization of the available copper area, litz wire consisting of 35 twisted strands with a diameter of 0.1 mm each is used. Compared to a single solid wire of equal outer diameter, it features a higher dc resistance but effectively minimizes the contribution of the ac resistances. As a first simplifying approximation, which is expected to yield fair results,

$$R_\mathrm{c} \approx R_\mathrm{dc} \tag{5.11}$$

can be used. A more detailed analysis requires the knowledge of the magnetic field distribution in each winding to asses the contributions of skin- and proximity losses. While analytical expressions can be found for the subsequently presented air coil design [91], this is not possible without further simplifications for designs employing ferromagnetic cores. Therefore, these losses were determined using 3D FEM simulations.

5.2.2 Core Losses

A stator core made from ferromagnetic material can be used to guide the magnetic flux that is generated by the stator coils toward the rotor and to reduce stray fields. Magnetic cores made from laminated silicon steel are commonly employed in conventional electric machines. Sheet thicknesses of several tenths of millimeters with intermediate insulation are used to reduce eddy current losses. While such materials have favorable magnetic properties, such as high relative permeability and saturation flux density, the occurring eddy current and hysteresis losses in the core rise rapidly with the field frequency, making them unsuitable for applications above a few kilohertz. Amorphous alloys, such as Metglas 2605SA1 [119], feature a significantly decreased sheet thickness (25 µm) and, therefore, decreased high frequency losses. Such materials have been used for the design of high speed machines [33–35] in the past. While favorable properties are attained up to $\approx 100\,\mathrm{kHz}$, the occurring core losses are still relatively high in the megahertz range. Therefore, a power ferrite material, which allows operation up to several megahertz, is used for the stator core in this work. Such materials usually have a lower saturation flux density than the aforementioned ones. However, this is uncritical for their application in the ultra-high-speed motor, as the occurring flux densities are limited to well below 100 mT by the rotor losses (see Section 4.3).

In the subsequent analyses, the material Ferroxcube 3C90 [120] is considered. Other ferrite materials with similar properties can be selected, where the decision criteria should be based on the occurring field frequencies, magnitude of the magnetic flux density, and temperature of the core.

The overall core losses can be modeled by the Steinmetz equation

$$P_{\mathrm{c,SE}} = V_{\mathrm{c}} C f_{\mathrm{s}}^{\alpha} B_{\mathrm{s,pk}}^{\beta}, \tag{5.12}$$

where V_{c}, f_{s}, and $B_{\mathrm{s,pk}}$ denote the core volume, the field frequency, and the peak value of the flux density, respectively. C, α, and β are material-dependent Steinmetz parameters. These parameters were cal-

Table 5.1: Ferrite 3C90 material characteristics

Parameter	μ_i	C	α	β
Value	≈ 2300	0.94	1.52	2.68

culated from the material datasheet [120] and are listed in Table 5.1, where μ_i denotes the initial relative permeability. The magnetic flux density varies throughout the core volume and its distribution has to be obtained prior to loss calculation.

The relation of (5.12) is only valid for sinusoidal variations of the magnetic flux density and excitation currents. As the currents are non-sinusoidal in the considered case, a generalized model for the core loss has to be used. The improved general Steinmetz equation (iGSE) considers arbitrary variations of the flux and is given as

$$P_\mathrm{c,iGSE} = V_\mathrm{c} C_\mathrm{i} f_\mathrm{s} (\Delta B)^{\beta-\alpha} \cdot \int_0^{T_\mathrm{s}} \left| \frac{\mathrm{d}B}{\mathrm{d}t} \right|^\alpha \mathrm{d}t, \tag{5.13}$$

where ΔB denotes the peak-to-peak variation of the magnetic flux density and T_s is the period of its variation [121]. The absolute value of the derivative $|\mathrm{d}B/\mathrm{d}t|$ is used to account for increased core losses due to high slew rates. The constant C_i is related to the previously considered Steinmetz parameters by

$$C_\mathrm{i} = \frac{C\sqrt{\pi}}{(2\pi)^\alpha \cdot 2^{\beta-\alpha}} \cdot \frac{\Gamma\left(\frac{2+\alpha}{2}\right)}{\Gamma\left(\frac{1+\alpha}{2}\right)}, \tag{5.14}$$

where Γ denotes the gamma function. For the trapezoidal current and flux waveforms, as discussed in Section 5.1, this yields

$$P_\mathrm{c,iGSE} = V_\mathrm{c} C_\mathrm{i} p (2B_\mathrm{t,pk})^{\beta-\alpha} \left(\frac{4 f_\mathrm{s} B_\mathrm{t,pk}}{p} \right)^\alpha, \tag{5.15}$$

where $B_\mathrm{t,pk}$ denotes the peak value of the trapezoidal waveform. To assess the influence of the non-sinusoidal excitation on the overall core

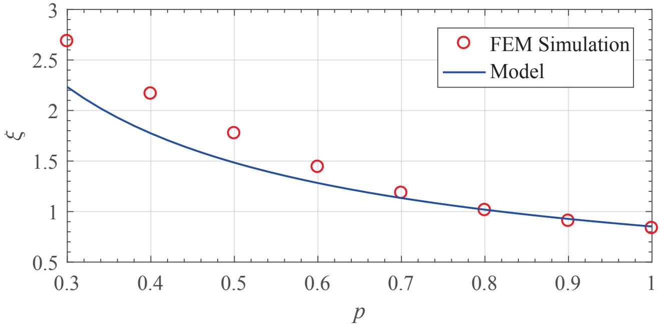

Figure 5.3: Ratio of $P_{\mathrm{c,iGSE}}$ to $P_{\mathrm{c,SE}}$ (see text for explanation) as obtained by the presented model and by simulations.

losses, the ratio

$$\xi = \frac{P_{\mathrm{c,iGSE}}}{P_{\mathrm{c,SE}}} \tag{5.16}$$

has been calculated for $B_{\mathrm{t,pk}} = B_{\mathrm{s,pk}}$. By using ξ as a correction factor, the core losses can be obtained for the occurring waveforms based on the well-documented material properties for a sinusoidal excitation. It is displayed in Fig. 5.3 for different values of p. It can be observed that the core losses are higher for the trapezoidal waveform than for a sinusoidal waveform with identical peak magnitude for most values of p. The calculations are in good agreement with values that were obtained by transient 3D FEM electromagnetic simulations for values of p close to unity. The deviations at low values of p result from an underestimation of the losses by the iGSE, as it neglects losses due to dc bias and relaxation effects. Analytic models for taking these losses into account have been presented in the literature [122, 123] but require additional modeling complexity.

5.3 Topologies

Various stator topologies can be used for the ultra-high-speed motor. The most simple one is a stator consisting of air coils and was used in similar experiments [6, 41]. In addition, a ferromagnetic core can be used

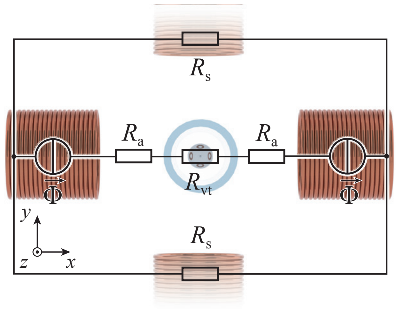

Figure 5.4: Magnetic circuit of a stator consisting of air coils.

[7]. The primary goal is to design a stator that yields a high magnetic flux density at the rotor while generating low losses. Subsequently, three possible topologies, one consisting of air coils and two featuring ferrite cores, are analyzed and compared.

5.3.1 Air Coils

The magnetic circuit of a stator consisting of air coils is illustrated in Fig. 5.4 for the same instant as considered in Fig. 5.1 at which the current in two of the coils is zero. The flux Φ as generated by the coils has to pass through the surrounding air, which is modeled by the magnetic reluctance R_a, to reach the vacuum tube and the rotor. The reluctance of the vacuum tube, which consists of a series of reluctances (glass, air, rotor), is modeled by R_{vt} and remains constant, independent of the stator design. The flux lines are closed through the ambient air, resulting in a large leakage flux due to the high reluctance R_s.

To achieve a high flux density at the rotor, the coil design has to be optimized to yield a minimum distance between the individual turns and the rotor. As the maximum current is constricted by (5.2), the inductance of the coil should be as low as possible. This is illustrated by considering the magnetic energy in a volume V, which can generally be expressed as

$$W_m = \frac{1}{2} \int \vec{H} \cdot \vec{B} \mathrm{d}V. \tag{5.17}$$

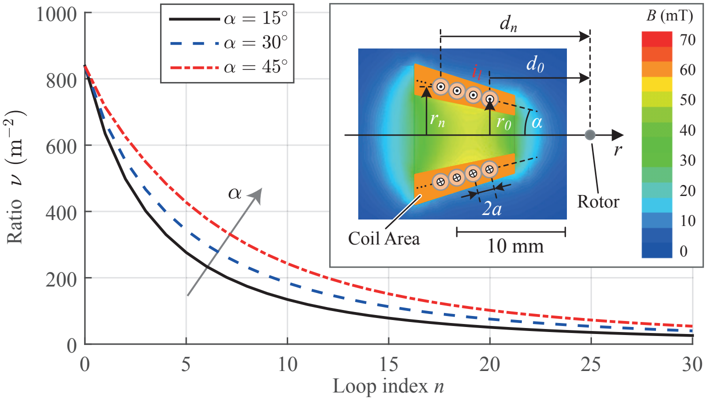

Figure 5.5: Ratio ν for the n^{th} winding and geometrical parameters for a conical air coil design with magnetic flux density density (inset).

Assuming constant magnitudes of H and B throughout the considered volume, using $H = B/\mu_0$ in the absence of ferromagnetic materials, and equivalently writing the magnetic energy using the coil inductance yields

$$W_{\mathrm{m}} = \frac{B^2}{2\mu_0}V = \frac{1}{2}LI^2. \tag{5.18}$$

By inserting (5.2) in (5.18) it follows that $B \propto \sqrt{1/L}$.

These requirements result in a conical coil shape, such as displayed in the inset of Fig. 5.5, for which the individual turns are located closer to the rotor than for a cylindrical coil. Yet, the increased radii of the turns which are located further away from the rotor also increase their inductance values. Exact analytical solutions for the magnetic field as generated by conical helix coils have been presented in [79]. By approximating the coil as multiple separated concentric loops, the influence of each winding can be assessed.

The magnitude of the flux density along the axis of the coil as generated by a single loop can be calculated by the Biot-Savart law as

$$B_n = \frac{\mu_0 \cdot i_{\mathrm{c}} \cdot r_n^2}{2(d_n + r_n^2)^{3/2}}, \tag{5.19}$$

where i_c, r_n, and d_n denote the current flowing in the loop, the radius of the loop, and the distance from the center of the loop to the center of the rotor for the n^th loop, respectively. The corresponding inductance can be approximated by

$$L_n \approx \mu_0 r_n \left[\ln\left(\frac{8r_n}{r_\mathrm{w}}\right) - 2 \right], \tag{5.20}$$

where r_w denotes the wire radius [124]. If multiple loops are combined to a conical coil, the distances to the center of the sphere and the radii of the individual loops are obtained as

$$r_n = r_0 + 2a \cdot n \cdot \sin(\alpha) \tag{5.21}$$

and

$$d_n = d_0 + 2a \cdot n \cdot \cos(\alpha), \tag{5.22}$$

respectively. Here, r_0 and d_0 denote the radius and distance of the first loop, respectively, and α is the semiangle of the cone. The minimum distance d_0 is determined by the requirements of the setup, such as the geometry of the optical path for the position sensors and the vacuum system, and should be as small as possible. For each loop, the ratio $\nu = B_n/(i_\mathrm{c}L_n)$, which relates the generated flux density at the rotor per current to the inductance of the winding, has been calculated for different values of α. The results are shown in Fig. 5.5 and illustrate that ν decreases for windings which are further away from the rotor, as expected. This occurs less rapidly for coil designs with a larger semiangle α.

For the practical implementation, a high flux density at the rotor and a low coil inductance were obtained by choosing a semiangle of 15 ° and three layers of 15 turns each (see Section 5.4). The resulting flux density distribution was obtained by 3D FEM simulation for a magnitude of $B_0 = 5$ mT at the center of the motor without the rotor in place and is displayed in the inset of Fig. 5.5. A rotor with a diameter of 1 mm has been added to the figure as a dimensional reference.

5.3.2 Ferrite Core Designs

By inserting a ferrite core along the axis of symmetry of the stator coils, the inductance is increased due to the high relative permeability μ_r of the core material. This decreases the achievable peak value of the drive current for a given dc-link voltage, but a significantly better guidance of the magnetic flux toward the rotor is achieved. The equivalent magnetic circuit of such a system with four individual ferrite cores is shown in Fig. 5.6. While R_{vt} remains the same, the magnetic reluctance R_{a} is decreased due to the smaller distance between the the vacuum tube and the tip of the ferrite core. The core features a low reluctance R_{c}. Due to the presence of the other ferrite cores in the vicinity of the vacuum tube, additional undesired bypass reluctances R_{b} are introduced, which model the tendency of the flux lines to close through an adjacent ferrite core instead of being guided through the vacuum tube to the opposite core. Based on the magnetic circuit, the condition

$$R_{\mathrm{b}} > R_{\mathrm{s}} + 4R_{\mathrm{a}} + 2R_{\mathrm{vt}} + R_{\mathrm{c}} \tag{5.23}$$

for the flux to be guided through the vacuum tube can be formulated. As a consequence, R_{b} should have a high value, which can be achieved by a suitable design of the ferrite core tips that maximizes the distance to an adjacent core. Moreover, as for the air coils, R_{a} should be made small by placing the ferrite cores as close as possible to the rotor. The stray reluctance R_{s} can be significantly reduced by using a ferrite yoke.

These considerations result in various possible stator designs of which three are displayed in Fig. 5.7. A spherical rotor of 1 mm in diameter has been added to the figures as a dimensional reference. The design shown in (a) consists of four individual ferrite cores and is equivalent to that discussed above. In (b), a ferrite yoke has been added to decrease R_{s}. As a consequence, the available space for a sensor system is limited to that between the coils and constricted by the yoke in the outward direction. Other topologies, such as the one displayed in (c) mitigate this problem by placing the yoke at a different vertical level than the rotor. However, such a design yields an increased core volume, which results in additional losses as outlined in (5.12) and (5.13). Therefore, the core volume should be kept small in order to limit the core losses. However, it has to be sufficiently large to prevent saturation and excessive local concentrations of the flux density. Moreover, a lower limit on the core volume is also

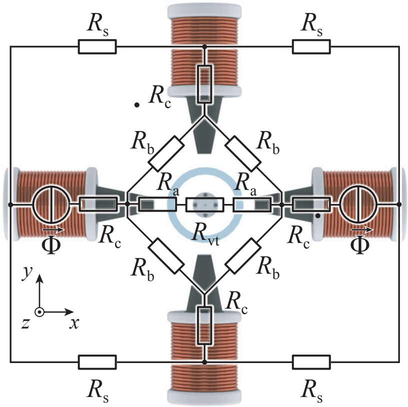

Figure 5.6: Magnetic circuit of a stator consisting of four coils with individual ferrite cores.

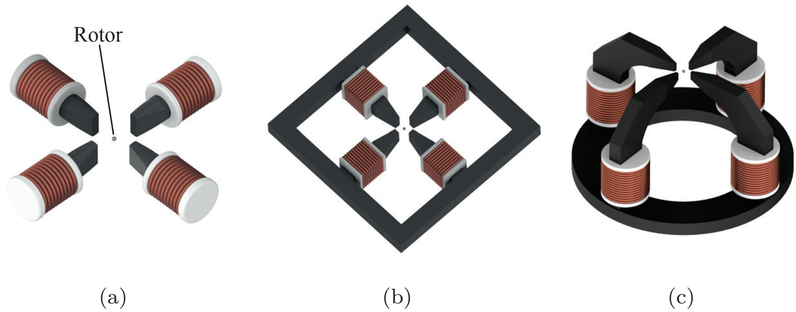

Figure 5.7: Exemplary stator designs employing ferrite cores: (a) four individual cylindrical ferrite rods, (b) an additional yoke is used to reduce the stray flux, and (c) a design to yield increased radial space in the vicinity of the rotor by placing the yoke at a different vertical level.

imposed by the requirement for mechanical stability. Furthermore, the design flexibility is significantly restricted by manufacturing constraints, as discussed below.

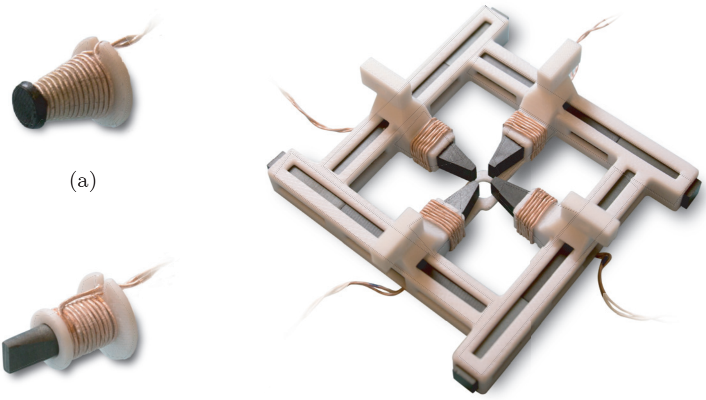

(a) (b) (c)

Figure 5.8: Photographs of the implemented stator designs: (a) conical air coils, (b) individual coils comprising a ferromagnetic core, and (c) coils with ferromagnetic cores and an additional yoke to decrease the stray flux.

5.4 Implementation and Comparison

Ferrite materials are highly brittle, which prevents the use of common machining techniques, such as milling. Due to their low conductivity, wire cutting usually cannot be applied. Instead, sintering is commonly used to attain the desired shape. The associated high tooling costs make this process unsuitable for a prototype implementation as considered here. As a result, the possible core shapes are limited by commercially available geometries for the desired ferrite material. The presented designs were manufactured from these geometries by using a grinding and polishing process.

Photographs of the implemented designs are shown in Fig. 5.8. The air coil shown in (a) was designed according to the guidelines of Section 5.3.1 with three winding layers consisting of 15 turns each. The windings were manufactured using litz wire (35 twisted strands with a diameter of 0.1 mm each). Four of these coils are mounted on a 3D-printed support each and placed at an angle of 90 ° apart around the rotor.

The design employing individual ferrite cores is shown in (b). The ferrite cores are manufactured from commercially available ferrite rods with a diameter of 6 mm and a length of 25 mm, which are inserted into cylindrical coils. A flat area was ground to the sides of the rods, yielding a width of the stator teeth facing the rotor of 2 mm. This concentrates the magnetic field close to the rotor and increases the air gap between adjacent cores, thus increasing the bypass reluctance R_b, as discussed above. The cores feature a height of 6 mm facing the rotor, which ensures a constant torque and radial bearing force for different axial rotor positions. The distance between two opposite core tips is chosen such that sufficient space for the vacuum tube and the sensors is provided. The windings consist of a single layer with 11 turns of litz wire and were designed to yield a high drive current for the employed inverter and dc-link voltage (see Chapter 7).

The design shown in (c) additionally features a yoke to decrease the stray reluctance R_s, which further increases the flux density at the rotor. It is based on ferrite cuboids with a square cross-section of $6 \times 6\,\mathrm{mm}^2$ and a length of 25 mm. The poles have the same geometry as before and the yoke is assembled by stacking multiple cuboids. Due to their fixed length, some additional material overlap at the corners exists. The individual cores should be strung together without unnecessary intermediate air gaps, as the latter would increase the reluctance. Therefore, the cuboids are held in place by a 3D-printed frame. The windings consist of 7 turns of the same litz wire that was used for the other designs.

A design as shown in Fig. 5.7(c) was not implemented due to manufacturing constraints. However, the performance of such a design is expected to be similar to that of a flat design comprising a yoke (see below).

In order to select the most suitable stator design for the ultra-high-speed motor, a comparative analysis of the presented implementations was carried out. The assessment was performed based on the achievable magnitude of the magnetic flux density at the rotor per required coil current and the occurring stator losses.

As the magnetic flux density varies inside and outside the cores, its distribution was obtained using 3D FEM simulations. The magnitude of the flux density per stator current in ampere-turns (AT) at the center of the motor was obtained as listed in Table 5.2. The results are shown without the rotor in place to exclude its influence on the flux density. It

Table 5.2: Comparative analysis of the achievable flux density per coil current for the presented designs

Air coils	Ferrite cores	Ferrite cores with yoke
9.17 µT/AT	73.6 µT/AT	255.7 µT/AT

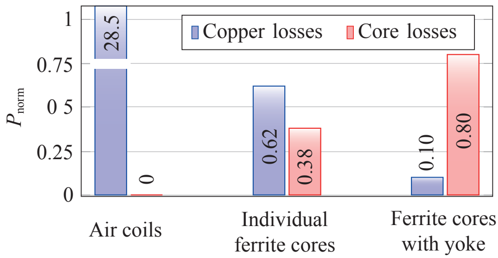

Figure 5.9: Comparison of occurring losses for the presented stator designs.

can be seen that the lowest flux density magnitude per AT is generated by the air coil design, while significantly higher values can be achieved by using ferrite cores.

The occurring stator losses were studied using eddy current simulations at a frequency of 500 kHz. The simulations were carried out for a flux density magnitude of $B_0 = 5\,\text{mT}$ at the center of the motor for all designs. For easy comparability of the results, the losses were normalized to the overall losses occurring in the design with individual ferrite cores. The results are shown in Fig. 5.9. While there are no core losses for the air coil design, the resulting conduction losses are excessively high. It is apparent that the overall losses can be significantly reduced with the ferrite core designs. The overall losses are similar for both designs with increased core losses for the design featuring a yoke, due to the higher core volume. For the chosen operating conditions, the absolute losses for the designs employing ferrite cores are in the range of a few watts, while those of the air coils easily reach several tens of watts. Therefore, the thermal limit of this design is reached even for low flux densities. Contrarily, the ferrite core designs are thermally uncritical and additional cooling can easily be provided by a regular fan, if required.

As the design comprising a yoke does not yield significantly lower losses and the achievable torque is limited by the rotor temperature, the stator featuring individual ferrite cores was used during most of the experiments (see Chapter 8). This yields the additional benefit of a more flexible adjustment of the individual components in the vicinity of the rotor.

Chapter 6

Sensor Systems

Closed-loop control of the rotor position in the axial and radial direction requires suitable sensors to provide the inputs for the controllers. An additional sensor system is required for measuring the rotational speed of the spinning ball. Both measurements have to be performed without mechanical contact through the wall of the vacuum tube. An evaluation of physical principles for contactless measurement of the rotor position in the ultra-high-speed motor is provided in this chapter. Subsequently, the design and implementation of a position sensor system based on optical transmission and a rotational speed sensor based on reflection are presented.

6.1 Principles

Various physical principles, such as inductive, capacitive, magnetic, acoustic, and optical sensing, offer the possibility to measure the rotor position without mechanical contact. However, their applicability is restricted by the considered application. Subsequently, the suitability of each principle is discussed.

Eddy current sensors are commonly used for inductive position sensing in bearingless machines and magnetic bearings [65, 66, 125]. In these sensors, eddy currents are induced in a conductive measurement target by an excitation coil. These eddy currents generate a secondary magnetic field that can be picked up by a sensing coil. A displacement of the measurement target results in a change of the coupling factors between the excitation coil and the target, as well as the target and the sensing coil. As a result, the information about the position of the target can be extracted from the induced voltage and current flow in the sensing coil. By using suitable modulation and demodulation schemes, excitation and sensing can be performed using the same coil. Various methods that use the inductance, resistance, or a combination of both to extract the positional information exist. For measuring the position of submillimeter-size spheres, the employed sensing (and excitation) coils should be of the same dimensions as the rotor to yield sufficient sensitivity [126]. The radius of a circular coil provides a good estimate for the maximum distance over which measurements can be carried out with sufficient sensitivity. Consequently, the distance between the sensing coil and the rotor would have to be in the submillimeter range. For the considered setup, this is not feasible due to the wall of the vacuum tube. Furthermore, eddy current sensors are based on the same physical principles as the drive system of the rotor considered in Chapter 4, and similar field frequencies in the range of several hundreds of kilohertz are commonly used. Therefore, interferences between the two systems are likely to occur, which would require additional effort regarding the necessary filtering and signal processing. In [86], the rotational speed of a steel sphere during rundown experiments was measured by an inductive pick-up coil. This was possible due to the absence of an external drive field, which would otherwise have been significantly larger than the rotor field. The employed principle relied on the existence of a radial component of the rotor magnetization to induce an alternating voltage with the same frequency as that of the mechanical rotation in the sensing coil. The rotors considered in this work consist of soft magnetic materials with a low remanence (see Section 2.5). Consequently, a remaining magnetization due to the drive system after it has been shut off cannot be guaranteed. Instead, a radial component generated by the axial magnetic bearing would have to be used. However, such a component generates undesired drag torques and should, therefore, be minimized by design. For the aforementioned reasons, eddy current sensors are unsuitable for obtaining reliable measurements of the position or rotational speed of the rotor in the ultra-high-speed motor and are not treated further.

Capacitive sensors use the dependency of the capacitance between a target and the sensing device to obtain a positional information. This requires a defined electrical potential of the sensing device and the target. As the rotor is levitated without contact, its electrical potential cannot

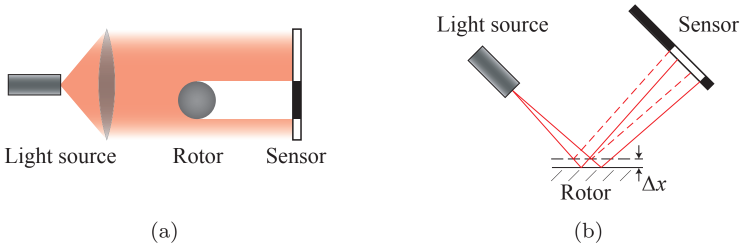

Figure 6.1: Principles of (a) transmission and (b) reflection for optical position sensing.

be held at a defined value, which makes capacitive sensing unsuitable for the considered application.

The flux density in electric machines is commonly measured using Hall effect sensors to determine the rotor angle. In bearingless machines and magnetic bearings, this principle can also be used to determine the translatory position of the rotor. The measured magnetic field consists of the combination of the magnetic field generated by the rotor and that of the stator. Measuring the position of the rotor requires that its field component can reliably be separated from the overall field. This is possible if the stator field can be compensated for or if the rotor field dominates. The latter is usually the case for permanent magnet rotors and suitable sensor placement. However, due to the low remanence of the rotors considered in this work, this condition is not fulfilled and the measured magnetic field would mainly consist of that generated by the stator, which makes application of this principle unsuitable.

Acoustic displacement sensors can be used over relatively large distances of several meters, but the spatial resolution is usually limited to the centimeter range [125]. Moreover, they cannot be used to measure the rotor position through the wall of the vacuum tube or in vacuum.

These considerations leave optical displacement sensing as the most suitable option for measuring the rotor position. It does not interfere with the magnetic field of the motor and is, therefore, expected to yield a high signal quality. While it is not influenced by the vacuum and can operate over relatively wide distances with high spatial resolution, optical sensing requires a transparent vacuum chamber around the rotor.

Two different methods for determining the rotor position are shown in Fig. 6.1. The rotor can be used to obstruct the transmissive path of light between a source and an optical sensor and its position can be inferred from the position of the shadow that is cast onto the sensor. In a different approach, light from a source is reflected at the rotor and captured by an optical sensor. The position at which the reflected light strikes the sensor depends on the position of the rotor. This principle is commonly referred to as triangulation and works most reliably if the target surface is flat or features a curvature with a large radius. As this is not the case for the considered spherical rotors, reliable position measurements can only be obtained using the transmission principle.

6.2 Optical Position Sensors

In order to use a sensor system based on optical transmission, a glass tube with an inner and outer diameter of 4 mm and 6 mm, respectively, is used as a vacuum chamber around the rotor. Such tubes are commercially available and feature a high surface quality and favorable optical properties. While a cylindrical shape results in optical distortions of the projected image of the rotor shadow, it features higher mechanical stability for withstanding the area forces due to the vacuum compared to shapes exhibiting flat surfaces and sharp corners.

A variety of sensors is suitable for use in an optical transmission system, for which an overview is provided in [127]. Segmented photodiodes, which produce an analog photocurrent proportional to the amount of incident light, can be used to infer the position of the rotor from the position of its shadow. At least two segments are required to measure the rotor position in a single axis and photodiodes with four segments can be used to measure the rotor position in two degrees of freedom. The sensitivity of such sensors is determined by the ratio of the area of the rotor shadow and the overall sensor area. Consequently, if the same sensor is used for various rotor diameters, the sensitivity decreases for smaller rotors. This problem can be mitigated by employing a charge-coupled device (CCD) or a complementary metal-oxide-semiconductor (CMOS) sensor, as commonly used in various imaging systems. Such sensors feature a discrete pixel structure, where the size of a pixel is much smaller than the considered rotors. Both sensor types are available with linear or areal pixel arrangements, allowing for the one- or two-dimensional determination of the rotor position. Data processing for these sensors is significantly more complicated than for the aforementioned analog sensors. For a sensor with a square-shaped active area, the illumination values of n^2 pixels, where n is the number of pixels per row and column, have to be sampled and processed. This, in conjunction with the required exposure time, usually limits the achievable frame rates to a few hundred frames per second (fps) for commonly available sensors and reasonable data processing complexity. These issues are addressed by sensors that are specifically designed for the acquisition of projection data, referred to as profile sensors [128, 129]. Instead of providing the light intensity for each pixel individually, the light intensity is integrated over each row and column. This reduces the number of required readout procedures to $2n$ and frame rates of several thousand fps can be achieved. However, acquisition and processing of the output signals is still significantly more complicated than for analog sensors.

6.2.1 Position Sensitive Device

For the selection of a suitable sensor for measuring the rotor position in the ultra-high-speed motor based on the optical transmission principle, the availability and electrical package of the device played an important role. A two-dimensional position sensitive device (PSD) sensor based on the photoelectric effect was chosen (Hamamatsu S5990-01) [130] due to its ease of use regarding the signal acquisition. The device features an active area of $4 \times 4\,\mathrm{mm}^2$ in a compact package that allows for placement of the sensor in close proximity to the rotor. The schematic structure and equivalent circuit of the sensor are displayed in Fig. 6.2(a) and Fig. 6.2(b), respectively. The *pn*-junction of the device is modeled as an ideal diode with parallel junction capacitance C_j and shunt resistance R_sh. The generated photocurrent is represented by a current source and the value of R_p depends on the centroid position of the incident light (see below). Details regarding the semiconductor-level implementation of the sensor and its noise characteristics can be found in [131, 132]. A light spot shining onto the active area (*p*-doped layer) of the PSD generates an electric charge at its incident position that is proportional to the light intensity. This charge is driven through a high resistivity layer of the semiconductor to the output electrodes located at the boundary of the

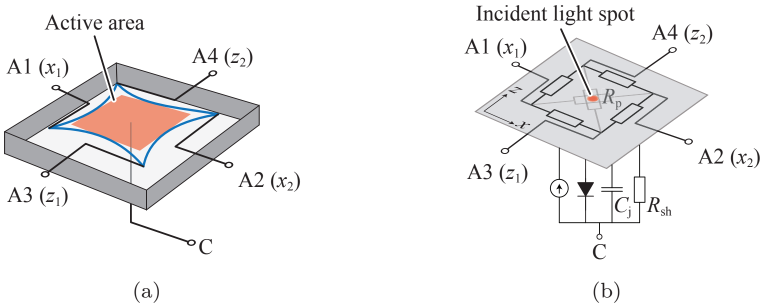

Figure 6.2: (a) Schematic structure and (b) equivalent circuit model of the employed position sensitive device (PSD) sensor.

active area, which results in measurable photocurrents. The employed two-dimensional PSD features two orthogonally-placed pairs of output electrodes. These electrodes (anodes) are connected to the terminals A1 and A2 as well as A3 and A4 for the x and z direction, respectively. The device features a common cathode C which is connected to an n-doped layer on the opposite side of the resistive layer. As shown in Fig. 6.2(a), the electrodes (blue lines) are not implemented as straight structures. Instead, they are dragged out toward the corners of the active area. Such a structure is chosen to reduce interaction between the electrodes near the corners, thereby increasing the output linearity of the sensor for incident light close to the circumference. This arrangement is referred to as a pin-cushion type PSD.

The chosen sensor features a spectral response range from $\lambda = 320 - 1100\,\text{nm}$ with the peak sensitivity occurring at $\lambda_\text{p} = 960\,\text{nm}$ in the near infrared (NIR) range. In order to generate high photocurrents and obtain a high sensitivity, operation close to this wavelength is necessary. Light emitting diodes (LEDs) with a housing diameter of 5 mm, half-angle $\phi = \pm 10\,°$ (angle at which the radiation intensity is halved with respect to frontal incidence), and a wavelength at peak emission of 950 nm (Osram LD 274) were used as light sources. This provides good optical matching with the sensor. To eliminate optical disturbances from external sources, particluary from those in the visible range, optical longpass edge filters with a cut-on wavelength of $\approx 700\,\text{nm}$ were mounted in front of the active sensor area.

A relation between the centroid position of the incident light and the photocurrents measured at the electrodes can be derived by considering the resistance R_p as symbolized in the equivalent circuit representation of the sensor (Fig. 6.2(b)). It is determined by the distance between the incident light spot and the considered electrode as well as the resistive layer of the sensor. Generally, R_p is different for each electrode (except for incident light exactly at the center of the active area), and can be obtained from the general formula

$$R_\mathrm{p} = \rho \frac{l}{A}, \tag{6.1}$$

where l, ρ, and A denote the distance between the incident light spot and the considered electrode, the resistivity of the sensor layer, and the cross-sectional area over which the photocurrent is conducted, respectively. As ρ and A are constant over the entire active area of the sensor, $R_\mathrm{p} \propto l$ holds. Therefore, the position of the light spot can directly be obtained from the ratio of the currents. For an incident light spot as shown in Fig. 6.3(a), the position is calculated as

$$x_\mathrm{l} = \frac{l_x}{2} \frac{(i_{x2} + i_{z1}) - (i_{x1} + i_{z2})}{i_{x1} + i_{x2} + i_{z1} + i_{z2}} \tag{6.2}$$

$$z_\mathrm{l} = \frac{l_z}{2} \frac{(i_{x2} + i_{z2}) - (i_{x1} + i_{z1})}{i_{x1} + i_{x2} + i_{z1} + i_{z2}}, \tag{6.3}$$

where l_x and l_z denote the distance between the corners of the electrodes in the x and z direction, respectively. The calculated position corresponds to the centroid of the incident light. As long as the light spot is entirely projected onto the active area, the sensor currents are linearly dependent on its position. A position detection error occurs if part of the light spot is projected outside of the active area. Rather than detecting the position of an incident light spot, the sensor is used to detect the position of the projected rotor shadow in this work. The sensor is fully illuminated with the exception of the shadow area as shown in Fig. 6.3(b). The centroid of the light is obtained from geometrical considerations as

$$x_\mathrm{l} = -\frac{A_\mathrm{s}}{A_0 - A_\mathrm{s}} \cdot x_\mathrm{s} \quad \text{and} \quad z_\mathrm{l} = -\frac{A_\mathrm{s}}{A_0 - A_\mathrm{s}} \cdot z_\mathrm{s}, \tag{6.4}$$

where $A_0 = l_x l_z$ and $A_\mathrm{s} = \pi r_\mathrm{s}^2$ denote the active sensor area and the area

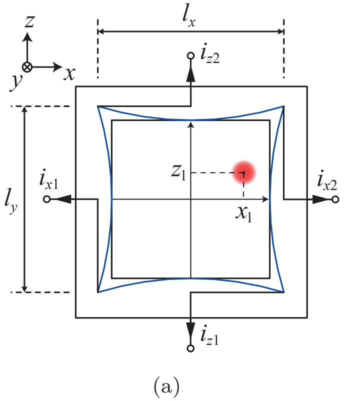

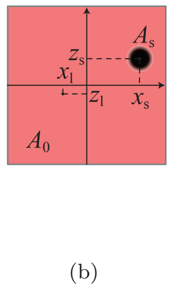

Figure 6.3: (a) Front view of the employed pin-cushion type PSD sensor with incident light spot. (b) Determination of the centroid of the incident light from the rotor shadow projected onto the active area.

of the rotor shadow, respectively. The position of the rotor is obtained by using (6.2) and (6.3) in (6.4) and rearranging for x_s and z_s. The radius of the shadow r_s is proportional, but not necessarily equal, to the rotor radius a. The shadow of the rotor is usually larger than the rotor, due to the projection with diverting light rays from the optical source. Moreover, distortion of the shadow occurs due to the curved surfaces of the glass cylinder used as a vacuum chamber. It can be observed from (6.4) that the sensitivity of the centroid position with regard to the position of the rotor shadow decreases quadratically with a due to the scaling with the ratio of A_s and A_0. This means that in order to achieve high sensitivity for small rotors, a sensor with a small active area has to be used or part of the area near the circumference should be masked to prevent illumination.

In order to measure the rotor position in all translatory degrees of freedom, two sensors are arranged around the vacuum tube at an angle of 90° apart as shown in Fig. 6.4. The combined drive and radial bearing coils (see Chapter 5) are placed along the axes denoted by x' and y'. As both sensors measure the rotor position in two dimensions, the z direction is measured twice. Averaging of the two sensor values can be applied to reduce the noise of the signal in this direction.

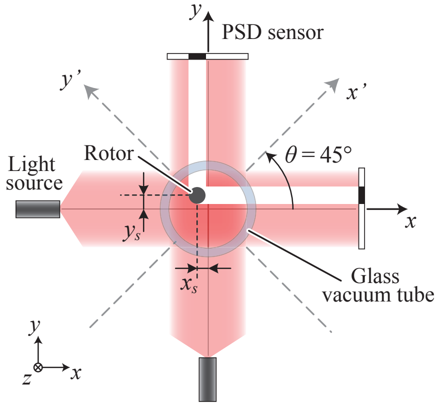

Figure 6.4: Cross-sectional view of the motor setup including the two position sensors and corresponding light sources.

6.2.2 Signal Conditioning

A signal conditioning circuit that converts the photocurrents into suitable signals for the digital controller is required. The corresponding circuit diagram is provided in Fig. 6.5, where three of the identical channels have been omitted for clarity. The anodes of the reverse-biased PSD sensors are each connected to separate analog operational amplifier (opamp) stages. The first stage consists of a transimpedance amplifier that converts the photocurrent into a voltage. The gain of this stage is set by the feedback resistor R_f as

$$V_\mathrm{out} = -R_\mathrm{f} I_\mathrm{in} \tag{6.5}$$

and was set to 120 000 in this particular case. To ensure stability of the circuit, a capacitor C_f is added in parallel to the resistor, which yields a lowpass filter characteristic of the circuit with cutoff frequency

$$f_\mathrm{3dB} = \frac{1}{2\pi R_\mathrm{f} C_\mathrm{f}}. \tag{6.6}$$

This frequency has to be sufficiently high to yield the desired bandwidth of the system. By considering the poles and zeros of the amplifier circuit in the frequency domain, a minimum value for C_f that guarantees

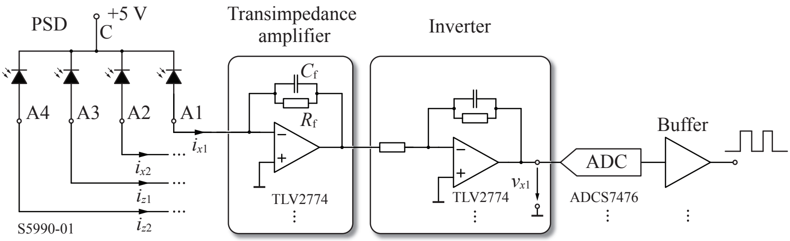

Figure 6.5: Signal conditioning circuit for one channel. The same circuit is used four times per sensor.

stability of the circuit can be derived [133]. This value is obtained as

$$C_\mathrm{f} = \sqrt{\frac{C_\mathrm{j} + C_\mathrm{cm}}{2\sqrt{2}\pi f_\mathrm{GBW} R_\mathrm{f}}}. \tag{6.7}$$

Here, C_j and C_cm denote the junction capacitance of the sensor (see above) and the common mode input capacitance of the opamp, respectively. The sum of these two capacitances form the overall input capacitance of the amplifier circuit. C_cm and the gain-bandwidth product, which is denoted by f_GBW, are determined by the chosen opamp. Due to the negative output voltage of this stage, a subsequent inverting amplifier with unity gain, which also implements additional lowpass filtering, is used. The combined cutoff frequency of both stages is chosen in the range of a few kilohertz to yield sufficient dynamics. Both stages are implemented using a high slew rate rail-to-rail amplifier (TI TLV2774). The output voltage at the second stage is sampled by a 12-bit analog-to-digital converter (ADC), which features a sampling rate of up to 1 megasamples per second (MSPS) (ADCS7476). The digital signal is buffered, level-shifted (MC74VHC1G125), and transmitted to an FPGA for further processing. The necessary clock (CLK) and chip select (CS) signals for controlling the ADCs are supplied by the FPGA. The aforementioned circuit stages are implemented four times per sensor to process each photocurrent separately. Calculation of the position of the rotor shadow according to (6.4) is carried out digitally by the controller.

An annotated photograph of the implemented sensor hardware is shown in Fig. 6.6. The main printed circuit board (PCB) contains the aforemen-

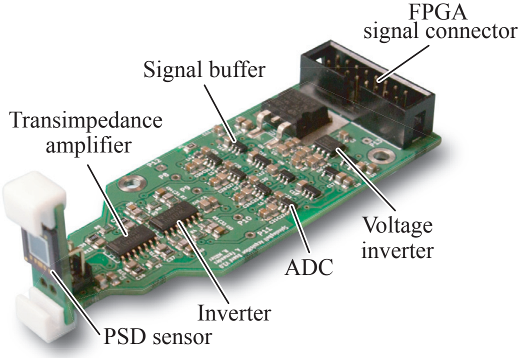

Figure 6.6: Annotated photograph of the designed sensor hardware.

tioned circuit components. In addition, a voltage regulator and charge pump inverter (Sipex SP6661), including the necessary filters, are implemented on the board to generate symmetrical supply voltages of ±5 V for the transimpedance amplifiers. A vertically attached PCB contains the PSD sensor facing toward the rotor. The visible white plastic parts are used to mount the aforementioned NIR filters. The system was designed to feature a narrow shape close to the sensor in order to fit the confined space around the rotor.

To validate the functionality of the designed system, a rotor was fixed to a copper wire with a diameter of 40 µm and suspended inside a glass tube. A high precision optical positioning table was used to displace the rotor horizontally inside the glass tube in front of the sensor. The voltage v_x was calculated from the four conditioned output signals of the sensor as

$$v_x = (v_{x1} + v_{z2}) - (v_{x2} + v_{z1}). \tag{6.8}$$

A linear dependency between the radial position of the rotor and the output signal is obtained for rotor displacements of up to ≈ 0.8 mm from the equilibrium position ($x_\mathrm{s} = 0$) as shown in Fig. 6.7. As the horizontal position of the sphere approaches the inner wall of the glass tube and the edges of the active sensor area, a nonlinear behavior can be observed due to optical effects. However, the obtained linear range is larger than the rotor diameter and, therefore, sufficient for obtaining

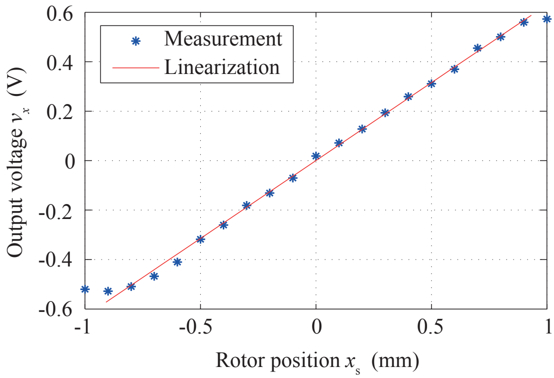

Figure 6.7: Measured sensor output for varying radial rotor displacement.

reliable measurements of the rotor position that can be used as inputs for the controller.

6.3 Rotational Speed Sensor

The rotational speed of the rotor is measured using the optical reflection method. As stated above, measuring the rotor position based on this method would require detection of the position or incident angle of light reflected by the rotor, which is difficult due to its spherical shape. Compared to this case, measuring the rotational speed is less critical as the reflective properties of the rotor surface can be used. As a consequence, only the light intensity has to be measured. If part of the rotor surface is marked to yield different reflective properties, modulation of the light scattered from the rotor with the rotational frequency occurs. In this work, the rotor was prepared prior to an experiment by putting a single black mark on its surface. This was achieved by placing the rotor onto a relatively rigid sponge and pushing a black permanent marker against the upward facing part of the rotor surface. As a result, the part of the rotor facing the sponge remains unmarked. Despite the high rotational speeds and centrifugal forces, the applied mark was found to remain on the surface. Moreover, the applied layer of paint did not result in any critical imbalances of the rotor.

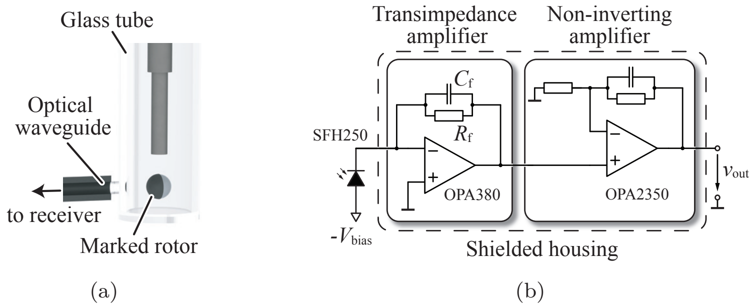

Figure 6.8: (a) Concept for measuring the rotational speed based on the reflected light of the marked rotor. (b) Circuit of the employed signal amplifier.

The two LEDs used for the position sensor system also serve as light sources for the speed sensor. Due to the confined space around the rotor, the reflected light is captured by an optical waveguide with an active diameter of 1000 µm and guided toward a receiver, as shown in Fig. 6.8(a). The chosen photodiode (Avago SFH250) is intended for use in high-speed optical communication systems, features rise and fall times in the range of 10 ns, and reaches $\approx$ 80 % of its peak spectral sensitivity at the used wavelength of 950 nm. The employed amplifier circuit for signal conditioning is similar to that of the position sensors and is displayed in Fig. 6.8(b). The diode is used in the photoconductive mode with a negative bias voltage to decrease its junction capacitance, thereby, increasing its speed. The first stage consists of a high gain transimpedance amplifier (TI OPA380) that was designed to yield a stable transimpedance bandwidth of 1 MHz, which is equivalent to a rotational speed of 60 Mrpm. Due to this high bandwidth requirement, attaining a high cutoff frequency (see (6.6)) and ensuring stability of the circuit based on the condition of (6.7) is more difficult than for the position sensor system. As a consequence, the gain of the first stage was limited and a second non-inverting stage was added to achieve additional amplification (TI OPA2350). Due to its high overall gain, the circuit is highly sensitive to noise and was, therefore, placed in a shielded metal housing. A laboratory supply with additional filters consisting of common mode chokes as well as LC lowpass stages was used to provide the necessary symmetrical supply voltages. The output signal of the circuit was measured by an oscilloscope which calculates its fast

Fourier transform (FFT) in real time. The result shows a distinct peak at the rotational frequency. Harmonic components could be observed but are much smaller in magnitude and can, therefore, clearly be separated from the desired signal. This yields a reliable method for obtaining the rotational frequency over the entire speed range.

To minimize the effect of constant ambient illumination, which yields a dc offset of the signal, ac-coupling is used. For the same reason, and to prevent saturation of the circuit output, the waveguide should be placed such that it faces into the same direction as one of the LEDs. This yields low ambient illumination and high intensity of the reflected light.

Chapter 7

Control and Power Electronics

This chapter provides an overview of the employed control structures and power electronic circuits for generating the necessary coil currents. Moreover, the corresponding hardware implementations are presented. Figure 7.1 provides an overview of the structure consisting of a cascaded control system for stabilizing the rotor in the axial direction as well as a position controller for each horizontal axis. All currents have to be controlled individually, requiring a separate power amplifier for each coil.

7.1 Control

Due to the different plant and actuator characteristics, control of the axial and radial translatory degrees of freedom are considered separately. Suspension of the rotor in the axial direction is passively unstable and the employed actuator coil has an inductance of several hundreds of microhenries, which limits the achievable dynamics of the bearing current. Contrarily, radial magnetic suspension of the rotor is passively stable and requires additional damping. The employed coils have an inductance of a few microhenries, thus, not imposing any relevant constraints on the current dynamics.

7.1.1 Axial Suspension

Recalling the linearized magnetic force of the actuator around the desired operating point (z_0, i_0) from (3.7) and using $f = m\ddot{z}(t)$ yields

$$m\ddot{z}(t) = k_s z(t) + k_i i. \tag{7.1}$$

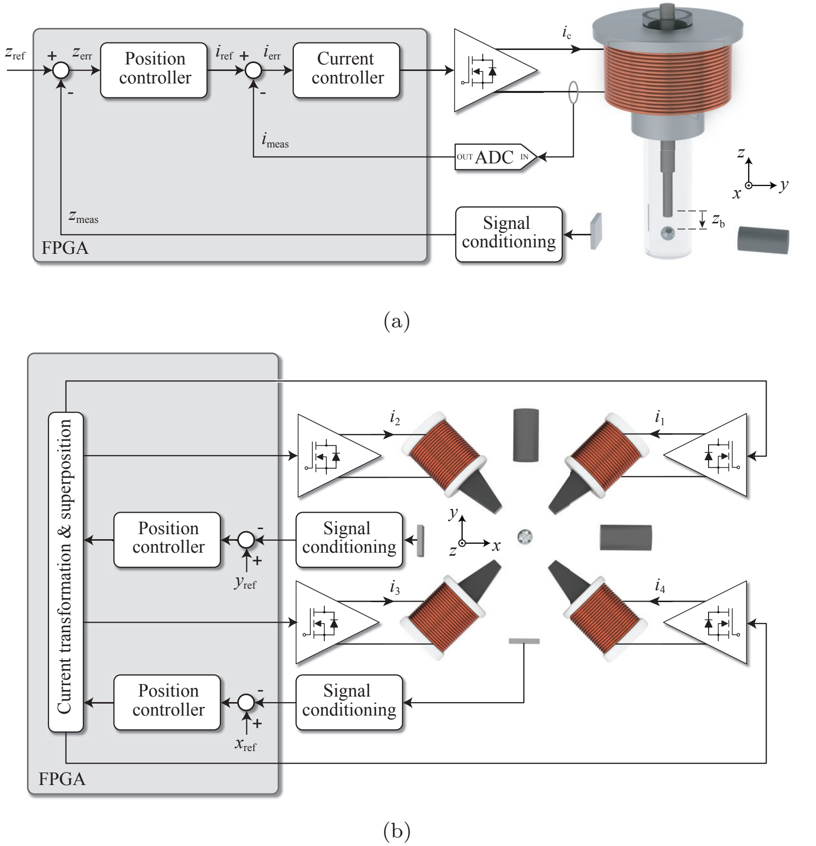

Figure 7.1: Overview of the (a) axial and (b) radial control structures including the necessary power amplifiers.

For the open loop system, only the offset current i_0 at the desired operating point will flow in the coil. Contrarily, the deviation i (see (3.6)), which is used to dynamically control the generated magnetic force, is zero. A solution to (7.1) is $z(t) = \exp^{\lambda t}$, which results in the characteristic polynomial

$$m\lambda^2 + k_s = 0 \tag{7.2}$$

with eigenvalues $\lambda_{1,2} = \pm\sqrt{|k_s|/m}$. This shows that the open loop system is unstable, as λ_1 is located in the right half of the complex plane. Consequently, active control is mandatory.

Many possibilities of varying complexity exist for the design of a suitable control law [134, 135]. As rotors of various sizes and dynamics have to be stabilized in this work, a robust control scheme independent of an accurate model of the mechanical plant is required. Moreover, the control parameters should be easily adjustable for different rotors. Therefore, a PID feedback control structure is used in this work.

According to Fig. 3.6(b), the closed-loop behavior of the suspension system is desired to be similar to that of a damped spring-mass oscillator. As a consequence, the linearized magnetic bearing force around the chosen operating point should exhibit a behavior described by

$$f_{\mathrm{m}} = k_z z + b_z \dot{z}. \tag{7.3}$$

In conjunction with (3.7), this yields the required bearing current as

$$i(z) = \frac{(k_z + k_s)z + b_z \dot{z}}{k_i}. \tag{7.4}$$

The resulting differential equation of the closed-loop system (cf. (3.28)) yields the characteristic polynomial

$$m\lambda^2 + b_z\lambda + k_z = 0 \tag{7.5}$$

with eigenvalues

$$\lambda_1 = -\sigma + j\omega \qquad \text{and} \qquad \lambda_1 = -\sigma - j\omega, \tag{7.6}$$

where σ and ω are given as

$$\sigma = \frac{b_z}{2m} \qquad \text{and} \qquad \omega = \sqrt{\frac{k_z}{m} - \frac{b_z^2}{4m^2}}, \tag{7.7}$$

respectively. Both conjugate complex eigenvalues are located in the left half of the complex plane, which shows that the system is stable. For $b_z = 0$ (zero damping), the system is limit-stable. The displacement-proportional (P) and velocity-proportional differential (D) feedback parts

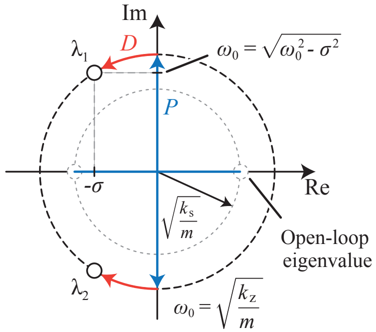

Figure 7.2: Closed-loop eigenvalues of the magnetic suspension system in the axial direction depending on P and D.

of the control can directly be identified from (7.4) as

$$P = \frac{k_z + k_s}{k_i} \qquad \text{and} \qquad D = \frac{b_z}{k_i}. \tag{7.8}$$

In magnetic suspension systems, P is usually chosen to yield a stiffness k_z that is in the same range as the bearing stiffness k_s [65]. The differential part is chosen to yield sufficient damping without decreasing the system dynamics. Therefore, the critically-damped case represents an upper useful limit, resulting in $0 < b_z < 2\sqrt{mk_z}$. The position of the eigenvalues of the closed-loop system are moved along circles with radius $\sqrt{k_z/m}$ as shown in Fig. 7.2. The position controller uses the desired levitation height of the rotor as a reference input. In order for the controller to adjust the current in the bearing coil such that this value is reached as a stationary operating point, an additional integral (I) feedback part of the control is used to reach stationary accuracy of the system.

Up to this point, the dynamics of the bearing coil have been neglected and it was assumed that the coil current follows the voltage that is applied across its terminals by the power amplifier without delay. This assumption is well satisfied for coils with a small inductance. However, for larger inductances, the dynamic behavior of the current as outlined in (3.29) has to be taken into account. To obtain increased dynamics of the coil current based on the applied voltage, an additional controller can be used in a cascaded control structure. Instead of feeding the output of the position controller to the input of the power amplifier directly, it is used as the reference input to a current controller. This controller requires a sensing circuit for the coil current and is usually implemented with PD feedback parts. Stationary accuracy of this controller is not required, as it is obtained by the outer position control loop. The overall system dynamics are increased as only the closed-loop eigenvalues of the inner control loop are relevant for the position controller. Moreover, no detailed model of the suspension coil is required. For such a structure to operate properly, the inner current control loop has to be executed significantly faster (> 10 times for the given system) than the outer position control loop. Besides a sufficiently fast controller implementation, this also requires high bandwidth current sensing.

The resulting overall control structure is provided in Fig. 7.3. The sensors were assumed as ideal with unity transfer function. In the practical system, additional digital lowpass filters are implemented for the position signal to reduce signal noise. This yields favorable damping behavior of the closed-loop system, as the high frequency noise would otherwise be amplified significantly by the D-part of the controller.

With the illustrated structure, it was possible to levitate rotors with diameters of 0.5 – 2 mm with the same actuator and only minor adjustment to the control parameters.

7.1.2 Radial Stabilization

Due to the ferromagnetic centering core, the rotor has a preferred equilibrium position that is imposed by the setup. The dynamic behavior of the magnetically suspended rotor in the radial direction is described by (3.30). This open-loop system is passively stable as both eigenvalues are located in the left half of the complex plane. However, they are located close to the imaginary axis, corresponding to a low damping factor d_r. As a result, slight disturbances of the rotor position cause oscillations, which are weakly damped and result in the axial magnetic suspension to become unstable if displacements become too large. Therefore, the main requirement for the radial position control is to implement a differential feedback part in order to achieve additional damping. An optional P-part can be used to adjust the dynamics of the radial system.

The overall control structure is shown in Fig. 7.4 for which an explana-

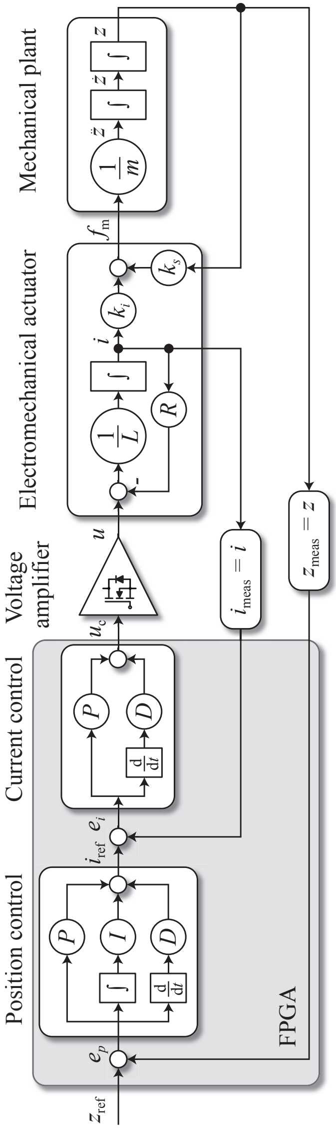

Figure 7.3: Detailed structure of the control system for axial suspension of the rotor.

tion is provided subsequently. Only one power amplifier and electromechanical actuator model are shown, while the remaining three have been omitted for clarity.

As rotation around a radial position that is different from the passive equilibrium would result in eddy current losses, an integral part of the controller is not required and would yield undesirable results. Instead, the rotor is allowed to rotate around its principal axis of inertia to eliminate dynamic forces due to potential small imbalances. This is achieved by a dead band around the equilibrium position in which no control action occurs. The threshold values for this dead band (x_t, y_t) can be adjusted depending on the rotor size and expected imbalances. For the implementation of such as dead band as well as the P-part of the controller, knowledge of the equilibrium position is required. The latter is obtained from slow moving-average steady state filters. The outputs of these filters are used as reference inputs for the controllers. Due to the low inductance of the radial bearing coils, no additional inner current control loop is required. Two separate identical position controllers are implemented for the x and the y axis. As the radial bearing coils are rotated by an angle of 45 ° with respect to the position sensors, a transformation of the controller outputs $u_{\mathrm{c},x}$ and $u_{\mathrm{c},y}$ equivalent to the Givens rotation

$$\begin{pmatrix} x' \\ y' \end{pmatrix} = \begin{pmatrix} \cos\varphi & -\sin\varphi \\ \sin\varphi & \cos\varphi \end{pmatrix} \begin{pmatrix} x \\ y \end{pmatrix} \overset{\varphi=45^\circ}{=} \frac{1}{\sqrt{2}} \begin{pmatrix} x-y \\ x+y \end{pmatrix} \tag{7.9}$$

has to be carried out. This part of the control also takes into account that only attracting bearing forces can be generated by a single coil, as the rotor is not a permanent magnet. The controller outputs are routed to different coils on opposing sides of the rotor according to their signs, resulting in the signals $u_{\mathrm{c},1}$ to $u_{\mathrm{c},4}$. The signals $u_{\mathrm{d},1}$, $u_{\mathrm{d},2}$, $u_{\mathrm{d},3}$, and $u_{\mathrm{d},4}$, which are necessary for generating the drive currents, feature phase shifts of 0 °, 90 °, 180 °, and 270 °, respectively. They are superimposed onto the aforementioned signals before being passed on to the power amplifier. The control structure was found to yield robust stabilization of the rotor in the radial direction as demonstrated in Chapter 8.

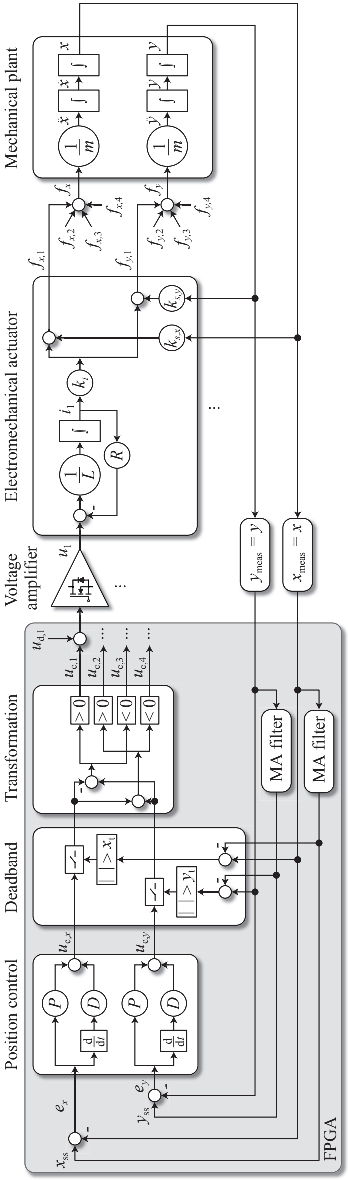

Figure 7.4: Detailed structure of the control system for active radial stabilization of the rotor.

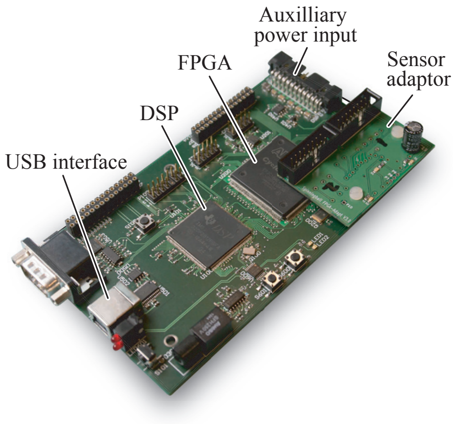

Figure 7.5: Implemented control hardware consisting of an FPGA and a DSP.

7.1.3 Implementation

The controllers, as shown in Figs. 7.3 and 7.4, have to be executed simultaneously to achieve stabilization of the rotor in all translatory degrees of freedom. Therefore, all controllers, the generation of the switching signals for the power amplifiers, and the control of the sensor ADCs are implemented digitally using a field programmable gate array (FPGA) (Altera EP3C16), which was programmed in VHDL. This allows for fast and accurately timed execution of all processes. Execution frequencies for the current controller in the range of the switching frequency can be reached. The control parameters and characteristics of the employed digital filters can be adjusted online via a USB interface to a PC. To implement this communication and other protocol-based sequential tasks, which would be inefficiently implemented on the FPGA, an additional digital signal processor (DSP) (TI TMS320F2810) is used. Communication between the DSP and the FPGA is realized via a memory interface. An annotated photograph of the implemented PCB containing the control hardware is shown in Fig. 7.5. The connection to the two position sensors is established via shielded ribbon cables to ensure signal integrity. The interface to the power electronics PCB (described below) for switching and ADC signals is provided using a flexible flat cable (FFC).

7.2 Power Electronics

Power electronic circuits are used to generate the bearing currents for magnetic suspension of the rotor, as well as the drive currents for its acceleration. These purposes impose different requirements on the converter system, which are discussed below.

7.2.1 Topology Selection

Several circuit topologies can be used to generate the required currents in the drive and bearing coils. In general, these topologies can be divided into analog and switching amplifiers. The former employ linear output drivers in which the coil voltage v_{c} is regulated by adjusting the voltage drop over a transistor. One of the most simple circuits is the complementary emitter follower as displayed in Fig. 7.6(a). An input voltage v_{in} is amplified by a pair of npn- and pnp-transistors. By using a symmetrical supply voltage V_{dc}, positive and negative coil currents can be obtained. Several alterations and improvements of this circuit featuring improved output linearity and biasing of the transistors exist [133]. Analog circuits employing operational amplifiers, such as the Howland current pump, are treated in detail in [136, 137] and have been applied in several magnetic bearing applications [7, 65]. As the difference between the supply voltage and the voltage applied across the coil has to be dissipated in the employed semiconductors, these circuits suffer from high power losses, regardless of their particular implementation. This disadvantage is overcome by switching power amplifiers, such as the H-bridge topology shown in Fig. 7.6(b). Bidirectional current flow in the coil can be achieved with a single positive supply voltage and regulation is obtained by PWM of the switching signals [115]. Switching results in a triangular ripple of the bearing current. In order to prevent negative effects on the stability of the magnetic suspension, the switching frequency has to be sufficiently high. Moreover, the dead time, which is required to prevent short circuits in the bridge legs, results in a nonlinear dependency of the output voltage and current of the bridge on the modulation duty cycle, as shown in Fig. 7.6(c). As long as a minimum duty cycle is not reached to overcome the dead time, the output voltage remains small before rising linearly as desired.

To overcome this disadvantage, several adapted circuit topologies, such

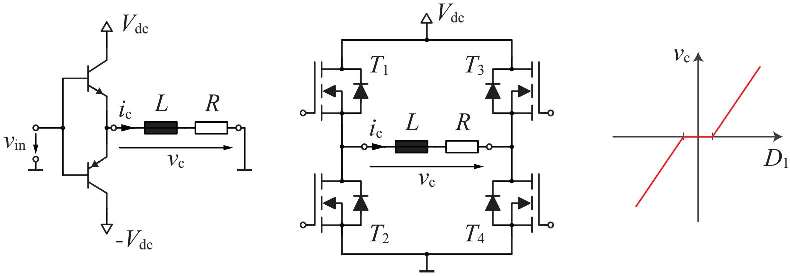

(a) (b) (c)

Figure 7.6: (a) Emitter follower as an example for a linear power amplifier circuit, (b) H-bridge switching converter, and (c) nonlinearity of the output voltage at small duty cycles due to the required dead time.

as the opposed current converter or dual-buck, have been proposed in the literature [138–140]. These amplifiers employ biasing to overcome the aforementioned zero-crossing distortion, which results in improved linearity but also generates additional losses. This could beneficially be applied to supply the actuator for axial suspension of the rotor (see Chapter 3). However, due to the relatively low required output currents, the losses caused by biasing were found to be in the same range as those of an analog amplifier. Instead, an H-bridge converter is used and the nonlinearity due to dead time is compensated for by the digital control.

The same topology is used for generating the currents in the radial coils. The drive currents feature a high frequency up to the megahertz range, while the superimposed bearing currents are in the range of 10 Hz. Due to the high drive frequencies, the H-bridge converter is controlled by a modified fundamental frequency switching scheme as explained below.

7.2.2 Modulation Scheme

Pulse-width modulation requires a switching frequency that is significantly higher than the desired output frequency. This is easily obtained for the axial bearing current and such a modulation scheme is used. Only attractive bearing forces can be generated, independent of the direction of the bearing current. Therefore, negative bearing currents are eliminated by the control as they would render the system unstable. Instead, the current is set to zero until the gravitational force has caused the rotor to fall back to its reference position. As a consequence, the corresponding H-bridge is operated similar to a buck converter by permanently switching T_3 off and T_4 on (see Fig. 7.6(b)), while modulating the switching signals of the left half-bridge.

As the frequency of the drive currents ranges from several hundreds of kilohertz to a few megahertz, PWM is no longer applicable. Instead, a fundamental frequency switching scheme, as illustrated in Fig. 7.7, is used. A symmetrical triangular counter is implemented on the FPGA that allows for the adjustment of the switching and the drive frequency by adjusting its maximum value C_{max}. A separate compare value is used for the left (red) and right (blue) half bridge to obtain the respective switching signals. If both compare values are set to $C_{\mathrm{max}}/2$ (dashed lines), the coil voltage is switched to alternate between $+V_{\mathrm{dc}}$ and $-V_{\mathrm{dc}}$ without any intermediate phases, resulting in a triangular coil current. Symmetrically moving the compare values away from $C_{\mathrm{max}}/2$ (solid lines), such that they feature a distance of ΔC counter ticks, results in intermediate phases between the commutation from $+V_{\mathrm{dc}}$ to $-V_{\mathrm{dc}}$ and vice versa during which the applied coil voltage is zero (black line). Consequently, the current peaks are truncated, yielding a trapezoidal waveform. Therefore, the value of p, which denotes the ratio of the peak values of the trapezoidal and the triangular currents as discussed in Chapter 5, can be adjusted by choosing ΔC accordingly. The shown waveforms illustrate the case $p = 0.5$. As discussed above, the currents for radial stabilization of the rotor have a significantly lower frequency than the drive currents. Therefore, they can be considered as a slowly varying average value of the drive currents. Such a non-zero average value can be implemented by shifting the compare values asymmetrically around $C_{\mathrm{max}}/2$ while leaving ΔC constant (dotted lines). The offset of the average of the two compare values (black dotted line) from $C_{\mathrm{max}}/2$ is determined by the output of the radial position controller.

All four combined drive and radial bearing currents are generated according to this scheme. To implement a $180\,^\circ$ phase shift between two opposite coils, the switching signals of the left and right half bridge are reversed. A phase shift of $90\,^\circ$ between adjacent coils is implemented by using two otherwise identical counters that are phase-shifted by $90\,^\circ$. As

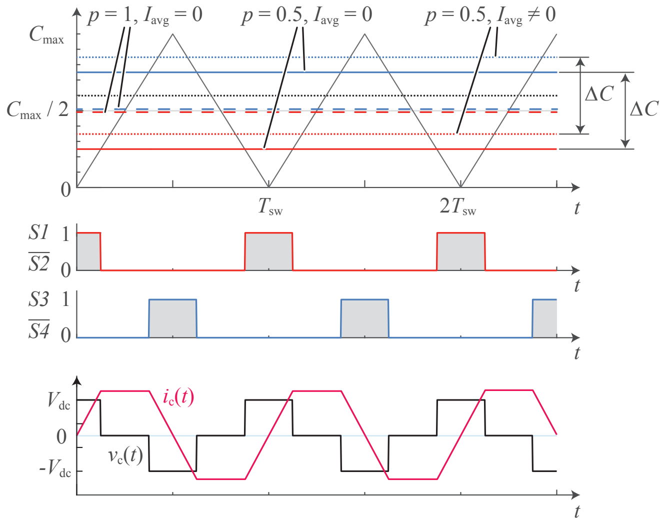

Figure 7.7: Modulation scheme for the switching signals resulting in trapezoidal drive currents superimposed onto the radial bearing currents.

a result, one counter is used to generate the switching signals for coils 1 and 3, while the second counter is used for coils 2 and 4.

7.2.3 Implementation

In order to control the currents in the axial suspension coil and the four radial coils individually, five H-bridges are required. The bridge that supplies the axial suspension coil additionally requires a current sensing circuit, which is implemented by symmetrical shunt resistors in each leg, as shown in Fig. 7.8. The voltage drop across these resistors is measured using an instrumentation amplifier circuit, as shown in Fig. 7.9. The output of this circuit is sampled by an ADC (LTC2361), buffered, and relayed to the digital control hardware. The shunt resistors and current sensing circuit are omitted for the drive channels.

Aside from this difference, all five H-bridges are implemented identically using discrete N-channel MOSFETs (FDD3682). These MOSFETs are driven by half-bridge gate drivers with only one signal input featuring

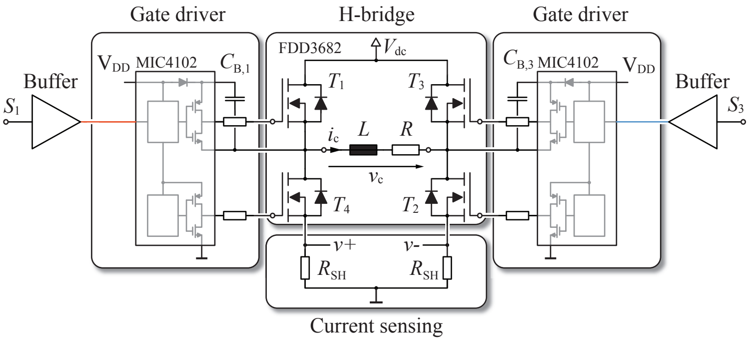

Figure 7.8: Circuit diagram of the H-bridge for generating the axial bearing current including shunt resistors for current sensing.

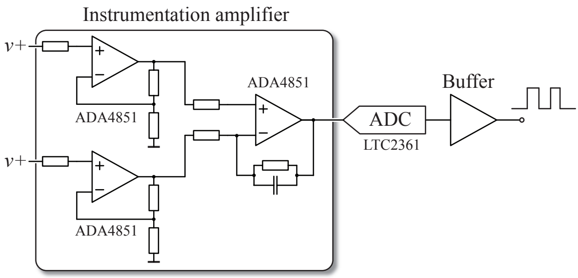

Figure 7.9: Instrumentation amplifier circuit used for current sensing.

internal dead time generation and shoot through protection (MIC4102). Both aforementioned components are rated for a maximum voltage of 100 V. An annotated photograph of the implemented power electronic converter PCB is shown in Fig. 7.10. The functional groups for generating the currents for the drive and radial AMB as well as for the axial magnetic suspension have been marked using red and blue lines, respectively. All logic input and output signals are routed via buffers from and to the control board.

The employed dc-link voltage for the axial magnetic suspension system was 24 V. Once levitation of the rotor is obtained, the inductor current is in the range below 100 mA, depending on the levitation height. However,

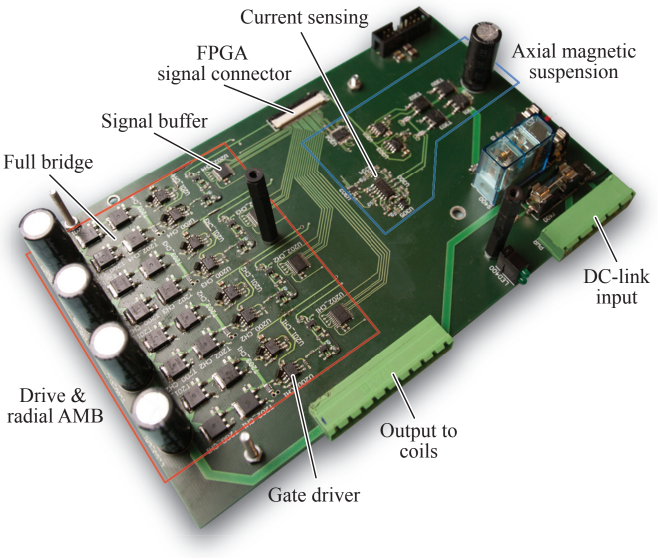

Figure 7.10: Annotated photograph of the power electronic converter PCB.

significantly higher currents are required for attaining initial levitation. The switching frequency of this H-bridge was chosen as $f_{\mathrm{sw}} = 100\,\mathrm{kHz}$ to yield sufficient dynamics and a low current ripple. The current sensing circuit features a maximum bandwidth of 125 kHz, facilitating fast current control between consecutive switching cycles.

The dc-link voltage of the drive and radial AMB coils was varied in the range of $\leq 48\,\mathrm{V}$ to adjust the drive current, which reached maximum values of $\approx 8\,\mathrm{A}$. The switching frequency of the four H-bridges was varied to adjust the drive frequency. With the employed components, frequencies of up to $\approx 1.5\,\mathrm{MHz}$ are possible. The electrolytic capacitors visible in Fig. 7.10 are only used for low-frequency buffering of the dc-link voltage. Additional ceramic capacitors for high-frequency buffering are mounted on the back of the PCB close to the respective bridges.

The presented converter system was designed with the primary goal of providing high robustness, and reaching a high power density was not a concern. If the design of a compact integrated system is to be pursued in the future (see Chapter 9), the use of modern gallium nitride (GaN) wide-bandgap semiconductor switches is expected to yield significant benefits.

Chapter 8

Experimental Results

To verify the models presented in the previous chapters and to obtain measured results for the achievable rotational speeds, an experimental setup for the ultra-high-speed spinning ball motor was designed and implemented. This chapter provides an overview of this setup and presents the result of various acceleration experiments based on which the achievable rotational speeds are assessed. Moreover, the performance of the magnetic suspension system is analyzed and the torque model presented in Chapter 4 is verified experimentally. The occurring failure mechanism of the rotors at ultra-high rotational speeds is investigated by means of microscope images and related to the models of Chapter 2.

8.1 Setup

An annotated overview of the experimental setup is shown in Fig. 8.1. Subsequently, an explanation of the relevant components is provided.

Structural Parts of the Motor

The structural parts of the motor are visible on the left hand side of Fig. 8.1 and consist of various platforms on which the necessary components are mounted. The four coils used for driving and stabilizing the rotor in the radial direction, the position sensors, the light sources, and the optical waveguide for the speed sensor are mounted on the adjustable stator platform. The latter can be used for the combined vertical adjustment of all aforementioned components. In addition, the radial position

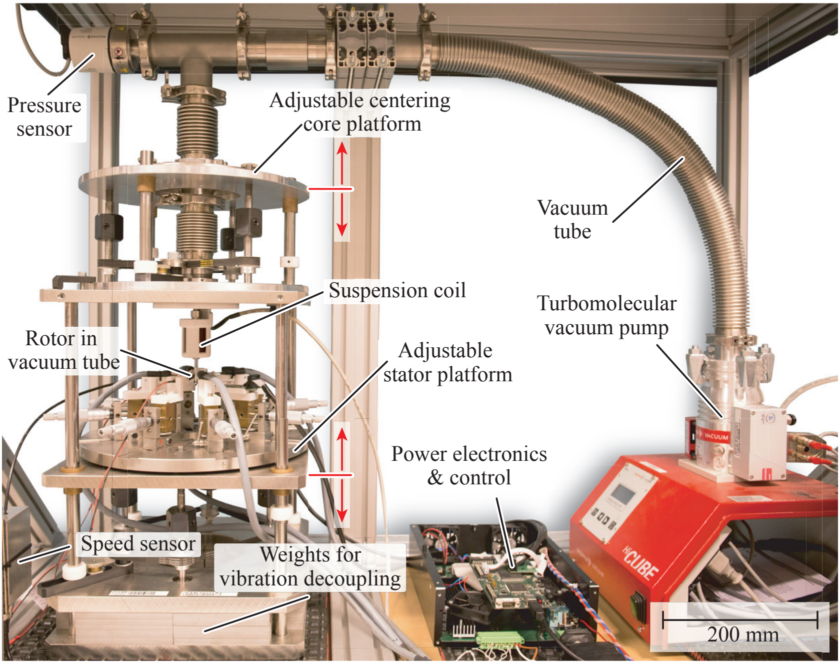

Figure 8.1: Annotated overview of the experimental setup.

of each component can be adjusted individually using high precision micrometers.

The coil for axial suspension of the rotor against the gravitational force is mounted on a fixed platform above the stator and is designed as outlined in Chapter 3. Above its upper end, it contains a vacuum fitting (Swagelok) that connects an exchangeable glass vacuum tube to the rest of the vacuum system. Vacuum-tight sealing of the glass tube at its lower end below the rotor is achieved using epoxy resin. The ferromagnetic centering core is mounted inside the vacuum chamber at the level of the adjustable centering core platform and extends downward to slightly above the rotor. By adjusting the height of the aforementioned platform, the position of the centering core is adjusted in the vertical direction, allowing for the alteration of the levitation height of the rotor with respect to the stator and axial actuator.

Vacuum System

To allow for the vertical adjustment of the centering core platform, flexible hoses are used. All vacuum system components are manufactured from stainless steel to yield high cleanliness, gas tightness, and sufficient mechanical strength, which makes the vacuum system suitable for reaching pressures in the high vacuum range.

The pressure is measured by a full range gauge (Pfeiffer Vacuum PKR 251), which is suitable for pressures from 5×10^{-7} Pa to 10^5 Pa in air. However, its rated accuracy of $\approx \pm 30$ % is only reached in the range from 10^{-6} Pa to 10^4 Pa due to the employed measurement techniques. As such a wide range of pressures cannot be measured using a single physical principle, the gauge employs two separate measurement systems, namely a Pirani and a cold cathode system, both of which conduct indirect gas-dependent pressure measurements. The former uses a heated metal wire that is introduced into the vacuum chamber. The gas pressure is determined indirectly from the heat transfer occurring at the wire, which depends on the number of gas molecules in its vicinity. In the employed sensor, this principle is used for the upper pressure range from 10^{-2} Pa to 10^4 Pa. Below a pressure of 1 Pa, the cold cathode system can be used. In such systems a voltage in the kV range is applied between a cathode and an anode to accelerate electrons. Upon traveling through the gas in the vacuum chamber, they ionize gas molecules, which results in a discharge current that is proportional to the gas pressure. By employing a cylindrical design of the electrodes in combination with an external arrangement of permanent magnets, referred to as an inverted magnetron, electrons can be made to travel on spiral trajectories, which increases the sensitivity of the device and extends its applicability to lower pressure ranges (see [94] for details). Due to the permanent magnets in the sensor, it should be installed sufficiently far away from the magnetic suspension system to prevent interference. At the same time, its location should be sufficiently close to the rotor to minimize measurement errors caused by pressure gradients in the vacuum chamber. Therefore, the sensor was installed directly above the mechanical support structure of the motor and attached to the overall system using a tee pipe.

All vacuum tubes, except for the one directly around the rotor, have an inner diameter of $d_{\mathrm{T}} = 40\,\mathrm{mm}$ (ISO-KF DN 40), which results in relatively large dimensions of the overall setup. A large diameter is beneficial for reducing pressure gradients inside the vacuum chamber, which are related to the throughput under free molecular flow conditions by

$$q_{pV} = \frac{\overline{c}}{4} AP(p_1 - p_2), \tag{8.1}$$

where p_1 and p_2 denote the considered pressure levels and $A = \pi d_{\mathrm{T}}^2/4$ is the cross-sectional area of the tube. P defines the transmission probability of a gas molecule through the tube, which is given for a tube with length $l_{\mathrm{T}} \gg d_{\mathrm{T}}$ as

$$P = \frac{4}{3}\frac{d_{\mathrm{T}}}{l_{\mathrm{T}}}. \tag{8.2}$$

Consequently, $q_{pV} \propto d_{\mathrm{T}}^3$ holds. Therefore, a larger tube diameter also makes it possible to reach the desired vacuum pressure quicker, which reasons the choice of the tube diameter.

The vacuum is generated by a two-stage pump system consisting of a membrane pump that is capable of reaching medium vacuum pressures (Pfeiffer Vacuum MVP 015-2) and a turbomolecular pump (Pfeiffer Vacuum HiPace 80) with a theoretical final pressure limit of $< 10^{-6}\,\mathrm{Pa}$, which is shown on the right hand side of Fig. 8.1. The former is connected to the exhaust side of the turbomolecular pump. To reduce vibrations that originate from the pump system to a minimum, a flexible vacuum tube, which is fixed to an external frame prior to connection with the motor setup, is used at the pump inlet. Moreover, the motor structure is placed on flexible rubber pads and features additional weights at its bottom to reduce vibrations. The membrane pump is connected via a bendable plastic tube and placed on the floor to eliminate vibrational coupling.

With the described setup, final vacuum pressures in the upper $10^{-4}\,\mathrm{Pa}$ range can be reached, which corresponds to high vacuum conditions. For reaching lower pressures in the ultra-high vacuum range, significant additional effort including bake-out of the vacuum chamber would be required [93]. As discussed in Chapter 4, this would not yield an advantage in terms of the drag torque acting on the rotor as the desired free molecular flow range is reliably reached already at pressures of $10^{-1}\,\mathrm{Pa}$. Evacuation of the system to $10^{-1}\,\mathrm{Pa}$ and $10^{-2}\,\mathrm{Pa}$ is reached within approximately 10 min and 30 min, respectively. Reducing the pressure to below $10^{-3}\,\mathrm{Pa}$ requires several hours.

The vacuum glass tube is usually destroyed by steel fragments after mechanical failure of the rotor occurs. Other more robust transparent materials, such as acrylic glass, were tested but found to yield inferior optical properties. To prevent loose debris from exiting the experimental setup, it is placed under a protective cover, which is closed during acceleration experiments.

Electronics and Measurement Instruments

The power electronic system and control electronics are shown in the center of Fig. 8.1 and are supplied by laboratory power supplies. The control electronics is connected to a PC that is used to adjust the control parameters and to visualize the sensor output data. The sensor signals are transmitted via shielded cables between the acquisition boards and the control electronics PCB to prevent cross coupling with the high frequency drive currents. Additional shielding around the twisted lead wires of the drive coils is employed. The output signal of the speed sensor is connected to an oscilloscope (Agilent MSO6034A) which determines the frequency of the modulated signal by calculating its FFT in real time. The oscilloscope is connected to a PC for data analysis purposes.

8.2 Magnetic Suspension Performance

After assembly of the setup, the gains and signal filters of the digital control system for vertical suspension of the rotor were adjusted to yield stable levitation at the desired position. Figure 8.2 shows a detailed annotated view of the motor components in the vicinity of the rotor. The inset shows a zoomed view of the levitated rotor, which was successfully stabilized without any mechanical contact.

To validate the theoretical model of the dynamic translatory behavior of the magnetically suspended rotor as outlined in Section 3.5, the parameters of the experimental system were identified by measuring the natural frequency ω_n and decay rate σ of radial oscillations. As radial stabilization could not reliably be obtained under vacuum conditions, the measurements were carried out at atmospheric pressure for the passively damped system. The result is shown in Fig. 8.3(a), which illustrates that oscillations are weakly damped and require more than 100 s to subside.

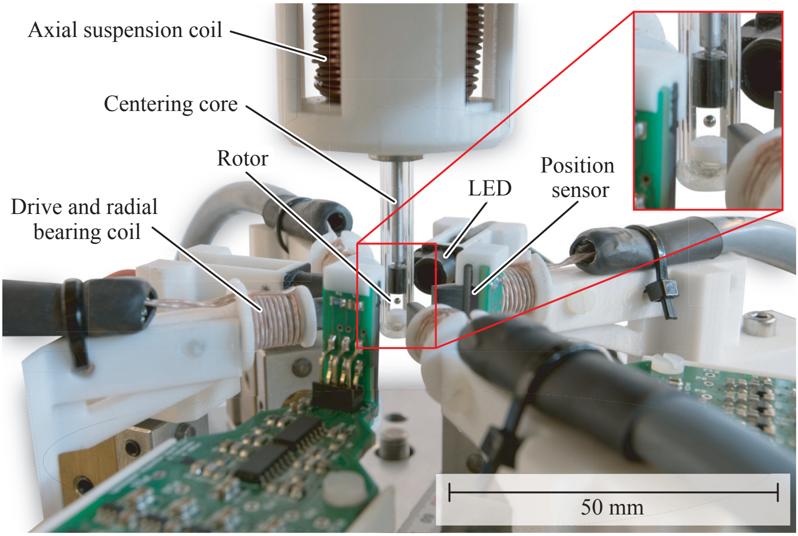

Figure 8.2: Photograph of the experimental setup with a magnetically suspended rotor. All relevant motor and sensor components including a zoomed view of the levitating rotor inside the glass vacuum tube are shown.

Table 8.1: Identified parameters of the experimental system

Rotor radius	a	$0.4\,\mathrm{mm}$
Rotor mass	m	$\approx 2\,\mathrm{mg}$
Decay rate	σ	$0.023\,\mathrm{s}^{-1}$
Natural frequency	$\omega_\mathrm{n} \approx \omega_0$	$52.4\,\mathrm{s}^{-1}$
Passive radial damping	$b_r = b_{r,\mathrm{c}} = 2m\sigma$	$0.93 \times 10^{-7}\,\mathrm{Ns/m}$
Radial stiffness	$k_r = \omega_0^2 m$	$5.60\,\mathrm{mN/m}$

This underlines the problem of low passive radial damping as discussed in Chapter 3. Based on the assumption that $\omega_\mathrm{n} \approx \omega_0$, which is justified due to the low damping factor, the system parameters were obtained as listed in Table 8.1. The measured values for the passive radial stiffness and radial damping are within the expected range as identified by theoretical considerations in Section 3.5.

To verify the performance of the proposed active radial damping by

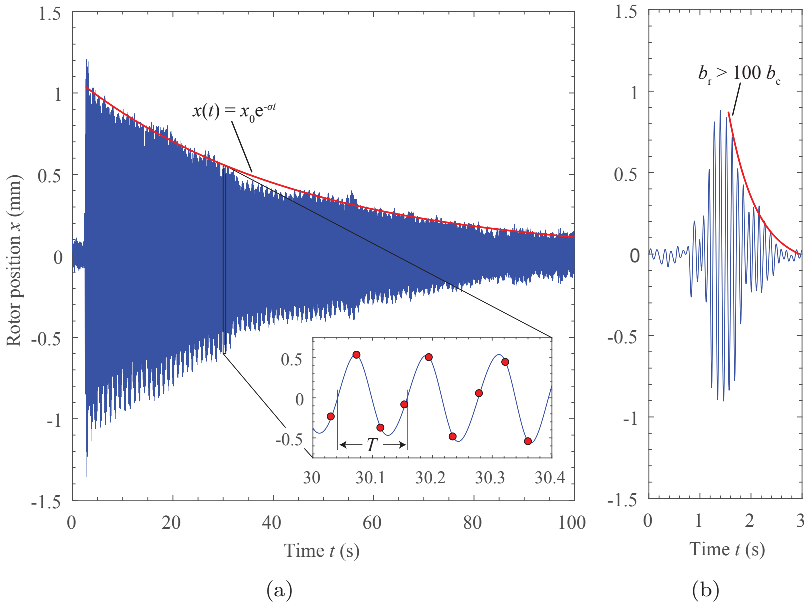

Figure 8.3: Rotor dynamics in the horizontal direction (a) without and (b) with active magnetic damping.

means of a magnetic bearing, the translatory behavior of the rotor as a response to a similar disturbance as that in the previous considerations was measured under high vacuum conditions. The result is shown in Fig. 8.3(b), which illustrates that the damping factor is more than 100 times larger than in the previous measurements. Oscillations subside within less than 2 s, thereby greatly increasing the stability of the magnetic suspension system. Reliable and robust magnetic suspension of the rotor in all translatory degrees of freedom, as attained by the presented AMB structure, is the prerequisite for reaching ultra-high rotational speeds.

8.3 Torque Characteristics

The torque model presented in Chapter 4 was verified through acceleration experiments during which the slip frequency f varied depending on the rotational speed of the rotor. The overall torque acting on the rotor was obtained from the angular acceleration rate as

$$T = I\dot{\omega}_{\mathrm{r}} \approx I\frac{\Delta\omega_{\mathrm{r}}}{\Delta t} \tag{8.3}$$

with the moment of inertia

$$I = \frac{2}{5}ma^2 = \frac{8}{15}\pi\rho a^5. \tag{8.4}$$

Using (8.3) requires the calculation of the angular acceleration as the small difference of two comparably large quantities containing measurement noise. To avoid the problems associated with this procedure, a polynomial was fitted to the experimental data. Only data points with an error between this polynomial and the measured values of less than 0.5 % (usually smaller) and at instants for which measurement values exist were used to obtain the angular acceleration.

A comparison of the modeled and measured torque characteristics of the motor including drag due to air friction is shown in Fig. 8.4. A rotor of 0.5 mm in diameter was used and the field frequency was chosen as 800 kHz, corresponding to a synchronous rotational speed of 48 Mrpm. The pressure at high rotational speeds during the experiment was 1.35×10^{-2} Pa. The shown error bars result from the calculation of the angular acceleration based on rotational speed measurements. The latter have a worst-case resolution of 500 Hz (30 000 rpm). The shaded blue area represents the ±30 % uncertainty of the pressure measurement (see above). The torque increases with the angular slip frequency due to a higher eddy current density inside the rotor, as expected. The residual between the measured and the modeled torque, as shown in the inset, is < 15 % for all slip frequencies and < 5 % for $f > 250$ kHz. The increased deviation at low slip frequencies (high rotational speeds) is attributed to the low relative level of the motor torque, which increases the effect of the drag torque caused by active magnetic damping in the horizontal direction.

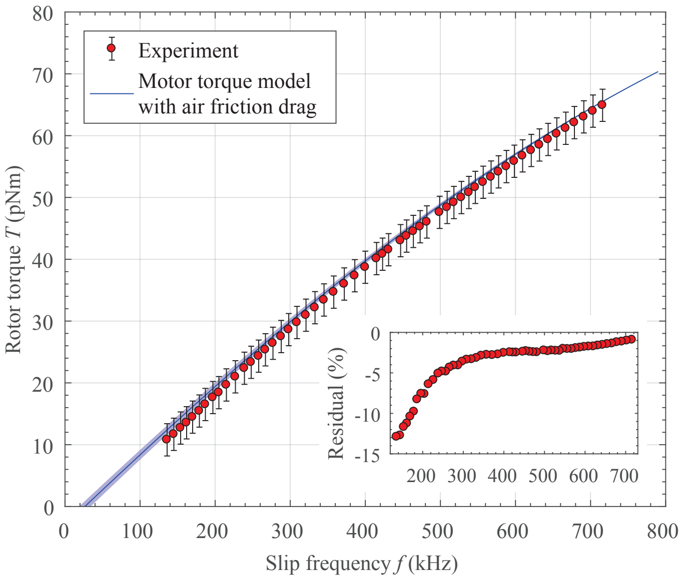

Figure 8.4: Comparison of the measured and modeled torque characteristics of the motor for a 0.5 mm rotor.

Figures 8.5(a) and 8.5(b) show the corresponding current density distributions inside the rotor for slip frequencies of 150 kHz and 700 kHz, respectively. These distributions were obtained by a harmonic analysis to take the trapezoidal shape of the drive currents and magnetic drive field into account, where the scaling factor $p = 0.5$ was used during the experiments and calculations (see Chapter 5 for details).

The resulting rotor temperature, as obtained by the models presented in Chapter 4, is shown in Fig. 8.6 for the same experimental conditions. While the temperature is undesirably high for high slip frequencies (low rotational speeds), it decreases to uncritical values for slip frequencies $f \lesssim 400\,\text{kHz}$ (high rotational speeds) and approaches the ambient temperature for $f \to 0$ due to decreasing eddy current losses. For the provided case, critical rotor temperatures are only obtained for rotational speeds $n < 24\,\text{Mrpm}$, which is less than 60 % of the bursting speed of the considered rotor. For higher rotational speeds, at which the strength of

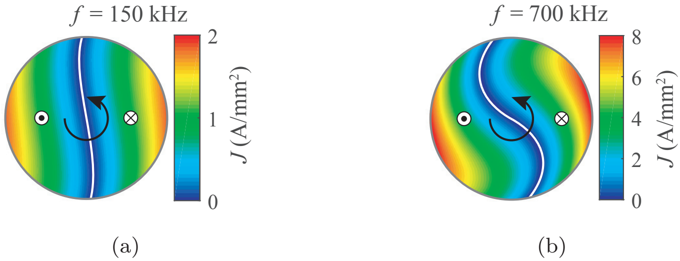

Figure 8.5: Current density distributions inside the rotor on the horizontal plane through its equator at slip frequencies of (a) 150 kHz and (b) 700 kHz, respectively.

the material is critical, the rotor temperature is bound to uncritical values below 150 °C. As the initial heating of the sphere at lower rotational speeds does not cause permanent alteration of the material structure, which is only anticipated to occur at temperatures $\gtrsim$ 600 °C for the considered materials [141], it is not expected to have a detrimental effect on the achievable rotational speed. If a rotor temperature below 150 °C over the entire range of rotational speeds is desired nevertheless, this can be achieved by controlling the slip frequency accordingly, which results in a lower acceleration rate. The inset of Fig. 8.6 shows the ratio of heat transfer between the rotor and the environment due to radiation and free molecular conduction. It can be seen that heat transfer due to radiation is roughly 40–130 times higher than that caused by free molecular conduction. Consequently, the rotor temperature is expected to remain in the same range even for very low vacuum pressures.

8.4 Achieved Rotational Speeds

Three exemplary acceleration curves to the bursting speeds of different rotors are displayed in Fig. 8.7. The shown rotational speeds were only limited by the mechanical stress due to centrifugal forces. The rate of acceleration is decreased at higher rotational speeds due to the lower slip frequency. It can be observed that smaller rotors are accelerated faster, as discussed in Section 4.2. The shown error bars represent the 500 Hz resolution of the speed measurements. The highest rotational speed achieved in this work was 40.26 Mrpm ($a = 0.25$ mm), for which the distribution of

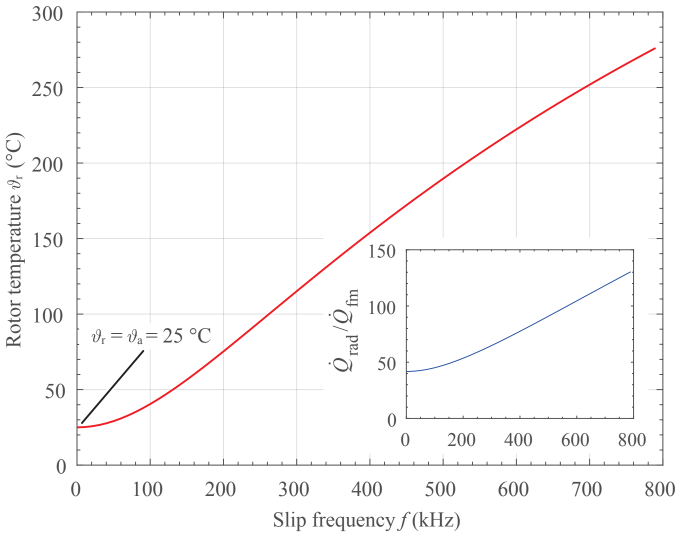

Figure 8.6: Rotor temperature over the considered slip frequency range. The inset shows the ratio of heat transfer between the rotor and the environment due to radiation and free molecular conduction.

the maximum principal normal stress inside the rotor shortly before its explosion is shown in the inset of Fig. 8.7. The used rotor material was 100Cr6 (1.3505) martensitic chrome steel ($\rho_r = 7610\,\mathrm{kg/m^3}$, $\nu = 0.3$).

In order to obtain a statistically significant number of samples for quantitative analyses, a series of ~ 50 experiments with various rotor diameters, materials, and initial material conditions was carried out. High variability was observed for the bursting speeds as shown Fig. 8.8. The displayed error bars show the 95 % confidence intervals for the respective mean. The observed variations are attributed to fluctuations in the thermal treatment, initial stress conditions, and potential flaws of the rotor materials. Moreover, anisotropies of residual stresses may cause a dependency of the achievable rotational speed on the axis of rotation.

An initial theoretical estimate of the achievable rotational speed was obtained using the maximum normal stress theory (see Section 2.1.2). The maximum value of σ_1 in the center of the sphere was compared to the UTS σ_t of the material and failure was predicted if $\sigma_1 \geq \sigma_t$. A value

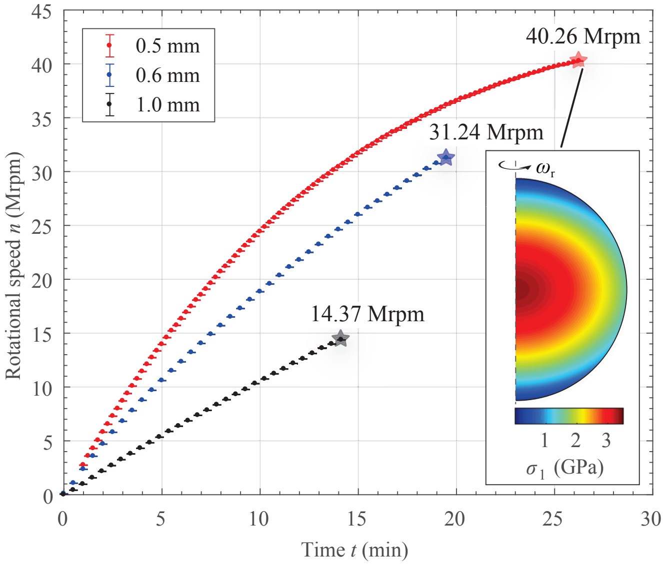

Figure 8.7: Acceleration curves for rotors of different diameters to their bursting speeds. The inset shows the maximum principal normal mechanical stress inside the rotor for the highest achieved rotational speed of 40.26 Mrpm shortly before its explosion.

of $\sigma_t = 1570\,\mathrm{N/mm^2}$ was used, which is commonly found in the literature for the UTS of small size ball bearing spheres made from 100Cr6 material [141–143]. The obtained achievable rotational speeds (theory curve in Fig. 8.8) are in good agreement with those obtained experimentally for the bigger spheres tested in this study but underestimate the mean of the achievable rotational speeds for smaller spheres by up to 46 %. In [39], this was attributed to a decreasing probability of flaws in the rotor.

An improved estimate for the achievable rotational speed was obtained by measuring the hardness of rotors of the same size and from the same manufacturing batch as those used in the acceleration experiments. The samples were prepared by grinding and polishing to expose different inner surfaces. On these surfaces, the Vickers hardness was determined at multiple locations using a microhardness tester (Wolpert MXT-α). All measured hardness values were within 5 % of their mean for rotors

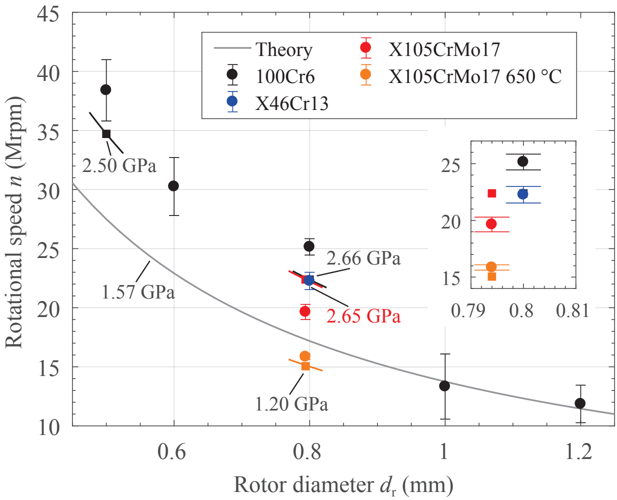

Figure 8.8: Achievable rotational speeds for different rotor sizes, materials, and initial stress conditions. The inset shows a magnification of the values for the diameters 0.794 mm and 0.8 mm, illustrating the influence of the material and thermal treatment on the achievable rotational speed.

without any additional material treatment. The UTS obtained from the mean value of these measurements based on the model provided in [144] was found to be higher than the aforementioned tabulated value. The attainable rotational speeds estimated based on these results are shown in Fig. 8.8 as lines with square markers alongside the respective UTS values. The deviation from the mean value of the experimentally obtained rotational speeds is reduced to less than 12 %.

Further experiments were carried out with rotors that were thermally treated prior to acceleration to reduce and equalize initial mechanical stresses. The thermal treatment consisted of heating the rotors to 650 °C with subsequent slow cooling to room temperature. All obtained hardness measurements for such rotors were within 2 % of their mean. The hardness, UTS, and bursting speeds of these samples were significantly decreased. The spread of the attained rotational speeds was greatly reduced with the range of all measured values lying within 2 % of their mean. The predicted rotational speeds are within ∼ 5 % of the measured values for these samples, which is a significant improvement over previous studies [6, 39]. The remaining underestimation of the achievable rotational speed is attributed to the conservative estimates for the UTS based on the hardness [144] and the assessment of failure based on Rankine's theory [45]. Some plastic ductile material flow near the axis of rotation is expected to occur, which redistributes and, thereby, lowers the stress inside the rotor.

8.5 Failure Mechanisms

To investigate the occurring failure mechanism at ultra-high rotational speeds more closely, the bursting of rotors was recorded by means of high frame rate photography. A high-speed camera (Photron FASTCAM SA1.1) was used to record 100 000 frames per second (fps) at a shutter speed of 1/283 000 s. The low exposure time requires high intensity lighting, which was provided by a high brightness LED (Advanced Illumination SL073) pointed directly into the camera lens from the opposite side of the rotor. The resulting images are provided in Fig. 8.9 and shown the rotor shadow. At 100 000 fps the attained image resolution is 192x160 px with a spatial resolution of ∼23 µm/px (≈ 6 % of the rotor radius) for the chosen field of view. Higher frame rates would be possible, but the spatial resolution would be decreased due to a smaller number of recordable pixels.

Figure 8.9 shows a time lapse sequence of rotors ($a = 0.4$ mm) exploding due to a high centrifugal force. In (a), the levitated rotor is still intact one frame before exploding. Frame (b) shows a rotor fractured into multiple parts. Rotor fractures hitting the inner wall of the vacuum glass tube, which are marked by red bars in all frames, are shown in (c). Complete disintegration of the rotor occurs within less than 10 µs. Therefore, the sequence was assembled by combining images from two different rotor explosions at 21.3 Mrpm (a), (c), as well as 23.4 Mrpm (b) to enhance the temporal resolution. No obvious deformation of the rotor is visible prior to explosion. Slight optical distortions are due to the circular glass vacuum tube. After hitting the walls of the vacuum chamber, the latter is destroyed by the inertia of the rotor fragments. The images confirm that the achievable rotational speed is only constricted by the

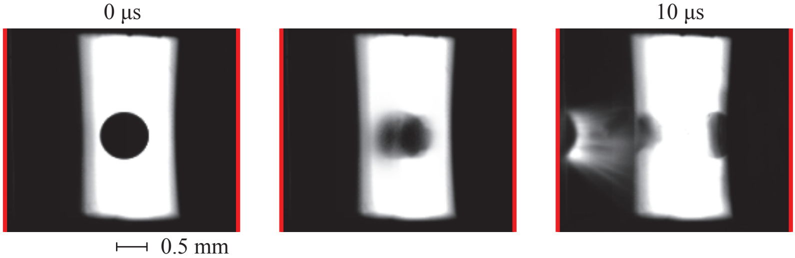

(a) (b) (c)

Figure 8.9: Rotors exploding due to high centrifugal force. High-speed image sequence showing a rotor (a = 0.4 mm), initially intact (a), fractured into multiple parts (b), and individual fractures hitting the wall of the vacuum glass tube (c).

mechanical stress limit of the rotor and that the latter is levitated in a stable manner until material failure occurs.

Subsequent to rotor failure, sufficiently large fragments were collected and their microscopic properties, particularly those of the fracture surfaces, were examined. Initial inspection of the rotor fragments was carried out using a zoom microscope (Leica M205 FA). Multifocus images were generated by recording a stack of multiple images focused on different parts of the fragments followed by their digital assembly. Such pictures are displayed in Fig. 8.10 and show that most of the larger fragments exhibit a wedge shape (a) and no significant deformation of the outer spherical contour. Some of the edges seem damaged and are contaminated by glass particles due to the collision with the vacuum tube. Closer inspection of an exemplary surface of one of the fragments (b) exhibits mostly characteristics typical of brittle tensile fracture, which validates the appropriateness of the used failure theory.

In addition, three-dimensional surface structures of the fragments were recorded using a laser scanning confocal microscope (Zeiss LSM 880). The same surface as shown in Fig. 8.10(b) is displayed in Fig. 8.10(c) including its three-dimensional structure. The acquired image data has a spatial resolution of 0.35 µm in the x and y directions and 0.49 µm in the z direction, respectively. It shows that there are no apparent voids or defects at which stress concentration and commencement of the failure could have occurred, which is in agreement with the theory stated in [39].

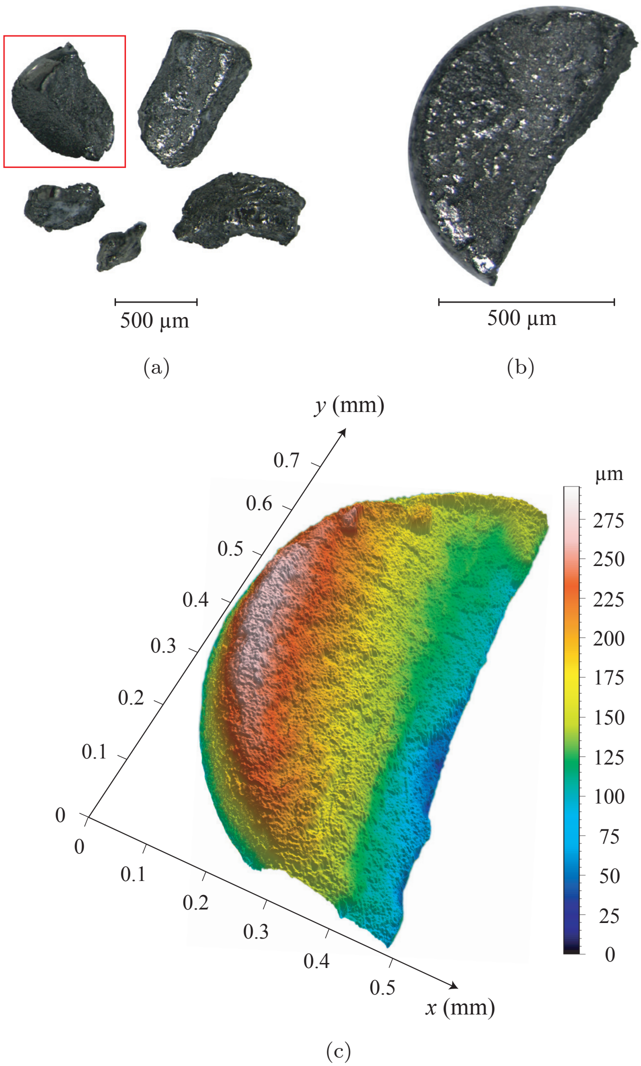

Figure 8.10: Microscope images of exploded rotor fragments. (a) Overview of recovered larger wedge-shaped rotor fragments of a 0.8 mm diameter rotor. (b) Detailed view of one exemplary surface of the fragments (red box). (c) Three-dimensional view of a fracture surface highlighting its structure.

In summary, the experimental findings are in good agreement with the models provided in the previous chapters. A new highest measured rotational speed of 40.26 Mrpm for an electrically driven rotor was achieved and a quantitative study of the achievable rotational speeds for various rotors was presented.

Chapter 9

Conclusion

9.1 Summary

A historical overview of high rotational speeds and their fields of application has shown that the highest rotational speed achieved by an electric motor dates back to 1947 and had not been reproduced or exceeded since. Recent years have shown an application-driven trend toward ultra-high rotational speeds, which sparked interest in the underlying limits and challenges.

To investigate and extend these boundaries, the modeling, design, and implementation of an ultra-high-speed electric motor has been presented. Guidelines for selecting suitable rotor materials and geometries have been provided based on their specific strength and dynamic rotational stability, respectively. To reduce bearing friction, a magnetic suspension system, by which the rotor is levitated without mechanical contact, has been employed. An actuator that allows for the integration of a vacuum system was designed, and a suitable topology for active magnetic stabilization of all translatory degrees of freedom of the rotor was developed and implemented. A detailed analytical model of the drive, which operates by the principle of a solid rotor induction machine, has been provided. In combination with mathematical models for the air friction losses and heat transfer mechanisms between the rotor and its environment, the thermal behavior of the rotor was assessed. It was shown that spinning the rotor under vacuum conditions is necessary. Suitable stator designs capable of handling the required magnetic field frequencies in the megahertz range were designed by employing power ferrite materials. A transmissive optical sensor system, which is capable of measuring the rotor position in all degrees of freedom through the wall of the vacuum chamber, was developed and implemented. Moreover, a sensor system for measuring the rotational speed of the rotor based on the modulation of scattered light has been demonstrated. A power electronics converter system and fully digital control structure for the combined generation of high-frequency drive currents and the coil currents for magnetic suspension of the rotor was presented.

The aforementioned components were combined to implement an experimental prototype of the ultra-high-speed motor. The latter was used to evaluate the performance of the active magnetic suspension system, which was found to yield the desired damping and stable levitation of the rotor throughout the entire attainable range of rotational speeds. The experimentally identified system parameters were found to be in good agreement with the provided theoretical values. The torque characteristics of the machine were verified through acceleration experiments and found to match the provided models. To provide a statistically significant number of samples for quantitative analyses, a series of acceleration experiments to the bursting speeds of different rotors was conducted. An investigation of the failure mechanism was carried out by high-speed imaging of the bursting process and subsequent microscopic analysis of the rotor fragments. It was shown that the presented failure models are suitable for predicting the achievable rotational speeds if close attention is given to the exact rotor material properties, such as the tensile strength and initial stress conditions.

During the acceleration experiments, ultra-high rotational speeds were successfully reached in a repeatable manner. The highest rotational speed achieved in this work was 40 260 000 rpm with a rotor of 0.5 mm in diameter. To the author's knowledge, this is the highest measured rotational speed achieved by an electric motor to date. It succeeds that published in 1947, which had not been reproduced or exceeded for almost 70 years.

9.2 Outlook

This thesis has provided insights into suitable technologies and their application for achieving ultra-high rotational speeds. Transferring these findings to future drive systems will facilitate higher rotational speeds and power densities.

Possible areas of future research include:

- The presented experimental setup is relatively large due to the adjustment possibilities of the individual components. A significantly smaller, more integrated system would provide the possibility to demonstrate ultra-high rotational speeds in a high density setup.
- If such a system can be manufactured with sufficiently low tolerances, further downscaling of the rotor, and, thereby, an increase of the achievable rotational speed seem possible. High precision manufacturing techniques, such as those employed for PCB manufacturing could beneficially be applied. Using even smaller rotors would additionally require a redesign of the position sensor system to yield sufficient sensitivity.
- An integrated system would also require an increased power density of the power electronic converter system. Due to the high frequency operation, GaN wide-bandgap semiconductor switches are expected to yield significant benefits.
- New rotor materials, such as carbon-based atom structures, are highly promising with regard to their specific strength and would facilitate significantly increased rotational speeds without further downscaling of the rotor. As soon as suitable manufacturing techniques that allow for precise mesoscale assembly of such materials become available, such rotors should be tested.
- If a higher motor torque is required, a rotor consisting of a permanent magnet could be employed. This would result in various challenges. The achievable rotational speed for the same rotor size would be lower than for the employed steels, due to the lower specific strength of common PM materials. Operation of the motor based on the principle of a synchronous machine would require alterations to the stator design. Field-oriented control of the drive and bearing currents at ultra-high rotational speeds would be highly demanding with regard to the required control.
- Circumferential speeds of up to 1047 m/s and centrifugal accelerations of $4.47 \times 10^8\ g$ were reached in this work. Such high accelerations open up new possibilities for hypergravity and materials testing experiments. To provide a suitable setup for such experiments, several adjustments to the current system, particularly with regard to the vacuum chamber, would be necessary.

- Possibilities for application of the presented principles to future drive systems have to be analyzed based on the desired fields of use. A partial redesign of the system components has to be undertaken according to the imposed requirements.

Appendix A

Magnetic Drive Field Derivation

This appendix provides the calculation steps and boundary conditions based on which the solution for the magnetic vector potential of the drive field inside and outside the rotor, as presented in Section 4.1.3, was obtained.

A.1 Boundary Conditions

Calculation of the vector potential is divided into two regions, namely, that inside the sphere ($r \leq a$) and that around it ($r > a$). As the surrounding is not conductive, $\sigma = 0$ holds outside the sphere, which simplifies

$$-\Delta\vec{A} + \mu_0\mu_r\sigma\frac{\partial\vec{A}}{\partial t} = 0 \tag{A.1}$$

to

$$\Delta\vec{A} = 0. \tag{A.2}$$

Two boundary conditions result from the requirements that the radial component of the magnetic flux density B_{rad} and the tangential component of the magnetic field H_{tan} have to be steady, corresponding to

$$\vec{n} \cdot ||\vec{B}|| = 0 \;\Leftrightarrow\; B_{\text{rad}}^{\text{out}} - B_{\text{rad}}^{\text{in}} = 0 \;\Rightarrow\; (\vec{n} \times \vec{\nabla}) \cdot ||\vec{A}|| = 0 \tag{A.3}$$

$$\vec{n} \times ||\vec{H}|| = \vec{0} \;\Leftrightarrow\; H_{\text{tan}}^{\text{out}} - H_{\text{tan}}^{\text{in}} = 0 \;\Rightarrow\; \vec{n} \times ||\frac{1}{\mu_0\mu_r}\vec{\nabla} \times \vec{A}|| = \vec{0}, \tag{A.4}$$

where $\vec{n}$ denotes the normal vector to the considered surface.

Far away from the sphere ($r \gg a$), the magnetic flux density is homogeneous and not influenced by the rotor. Consequently, the vector potential additionally has to fulfill the asymptotic condition

$$\vec{A} \longrightarrow \vec{A}_0 = \frac{1}{2}\vec{B}_0 \times \vec{r} \tag{A.5}$$

with

$$\vec{r} = \begin{pmatrix} r \\ 0 \\ 0 \end{pmatrix} \cdot \begin{pmatrix} \vec{e}_r \\ \vec{e}_\theta \\ \vec{e}_\varphi \end{pmatrix}. \tag{A.6}$$

A.2 Vector Potential

Based on (A.5) and the formulated rotating magnetic flux density

$$\vec{B}_0 = \mathrm{Re}\{B_0 \vec{b} e^{j\omega t}\}, \tag{A.7}$$

the ansatz

$$\vec{A} = \frac{1}{2} B_0 \,\mathrm{Re}\{F(r)\vec{b} \times \vec{r} e^{j\omega t}\} \tag{A.8}$$

is used for the solution of

$$\vec{B} = \vec{\nabla} \times \vec{A} \tag{A.9}$$

in the entire space. $F(r)$ denotes a complex-valued function that describes the amplification of the external magnetic flux density B_0 in the various regions and has to be chosen such that (A.1) and all aforementioned boundary conditions are satisfied. In spherical coordinates, this can be rewritten as

$$\vec{A} = \frac{1}{2} B_0 r \,\mathrm{Re}\left\{ F(r) \begin{pmatrix} 0 \\ j\cos\varphi - \sin\varphi \\ -\cos\theta(\cos\varphi + j\sin\varphi) \end{pmatrix} \cdot \begin{pmatrix} \vec{e}_r \\ \vec{e}_\theta \\ \vec{e}_\varphi \end{pmatrix} e^{j\omega t} \right\}. \tag{A.10}$$

For the space inside the sphere, using (A.10) in (A.1) results in $F(r)$ having to fulfill the ODE

$$\frac{\partial^2 F(r)}{\partial r^2} + \frac{4}{r}\frac{\partial F(r)}{\partial r} - j\mu\sigma\omega F(r) = 0 \quad \text{for} \quad r \leq a. \tag{A.11}$$

A solution can be obtained as

$$F(r) = C_1 \left(\frac{\sin(c_{\mathrm{ec}} r)}{(c_{\mathrm{ec}} r)^3} - \frac{\cos(c_{\mathrm{ec}} r)}{(c_{\mathrm{ec}} r)^2} \right) = C_1 f(c_{\mathrm{ec}} r), \tag{A.12}$$

where C_1 denotes an integration constant and the eddy current constant was defined according to [90] as

$$c_{\mathrm{ec}} = \sqrt{-j\mu\sigma\omega} = \frac{1-j}{\delta} \tag{A.13}$$

with the skin depth

$$\delta = \sqrt{\frac{2}{\mu\sigma\omega}}. \tag{A.14}$$

In the space around the sphere, the condition $\sigma = 0$ simplifies (A.11) to

$$\frac{\partial^2 F(r)}{\partial r^2} + \frac{4}{r}\frac{\partial F(r)}{\partial r} \quad \text{for} \quad r > a, \tag{A.15}$$

for which the solution

$$F(r) = C_2 + C_3 \frac{1}{r^3} \tag{A.16}$$

with two additional integration constants C_2 and C_3 can be obtained.

To fulfill the boundary condition of (A.3),

$$F^{\mathrm{out}}(r \to a) - F^{\mathrm{in}}(r \to a) = 0 \tag{A.17}$$

has to hold. Using (A.12) and (A.16) yields

$$F(r) = C_1' \frac{f(c_{\mathrm{ec}} r)}{f(c_{\mathrm{ec}} a)} \tag{A.18}$$

and

$$F(r) = C_2 + C_3' \left(\frac{a}{r}\right)^3, \tag{A.19}$$

respectively. Moreover,

$$C_1' = C_2 + C_3' \tag{A.20}$$

has to hold. The asymptotic condition of (A.5) yields

$$F(r) \to 1 \quad \text{for} \quad r \gg a, \tag{A.21}$$

which resutls in $C_2 = 1$.

The boundary condition of (A.4) results in the differential equation

$$\begin{aligned} \frac{1}{\mu_0}\left(r\frac{\partial F^{\mathrm{out}}(r\to a)}{\partial r} + 2F^{\mathrm{out}}(r\to a)\right) \\ - \frac{1}{\mu}\left(r\frac{\partial F^{\mathrm{in}}(r\to a)}{\partial r} + 2F^{\mathrm{in}}(r\to a)\right) = 0. \end{aligned} \tag{A.22}$$

From this, C_3' can be derived as

$$C_3' = D(c_{\mathrm{ec}}a) = \frac{(2\mu_r+1)g(c_{\mathrm{ec}}a)-1}{(\mu_r-1)g(c_{\mathrm{ec}}a)+1}, \tag{A.23}$$

where

$$g(c_{\mathrm{ec}}a) = f(c_{\mathrm{ec}}a)\frac{c_{\mathrm{ec}}a}{\sin(c_{\mathrm{ec}}a)} = \frac{1-(c_{\mathrm{ec}}a)\cot(c_{\mathrm{ec}}a)}{(c_{\mathrm{ec}}a)^2}. \tag{A.24}$$

This results in

$$F^{\mathrm{in}}(r) = [1+D(c_{\mathrm{ec}}a)]\frac{f(c_{\mathrm{ec}}r)}{f(c_{\mathrm{ec}}a)} \tag{A.25}$$

and

$$F^{\mathrm{out}}(r) = 1 + D(c_{\mathrm{ec}}a)\left(\frac{a}{r}\right)^3. \tag{A.26}$$

Inserting this solution into the ansatz (A.8) and taking the material relations into account yields

$$\vec{A} = \frac{1}{2}B_0\,\mathrm{Re}\left\{[1+D(c_{\mathrm{ec}}a)]\frac{f(c_{\mathrm{ec}}r)}{f(c_{\mathrm{ec}}a)}\vec{b}\times\vec{r}e^{j\omega t}\right\} \tag{A.27}$$

and

$$\vec{J} = \frac{B_0}{2\mu a^2}\,\mathrm{Re}\left\{(c_{\mathrm{ec}}a)^2[1+D(c_{\mathrm{ec}}a)]\frac{f(c_{\mathrm{ec}}r)}{f(c_{\mathrm{ec}}a)}\vec{b}\times\vec{r}e^{j\omega t}\right\} \tag{A.28}$$

for $r \leq a$ and

$$\vec{A} = \frac{1}{2}B_0\,\mathrm{Re}\left\{\left[1+D(c_{\mathrm{ec}}a)\left(\frac{a}{r}\right)^3\right]\vec{b}\times\vec{r}e^{j\omega t}\right\} \tag{A.29}$$

for $r > a$. These solutions have been used for the considerations presented in Chapter 4.

Bibliography

[1] C. Zwyssig, J. W. Kolar, and S. D. Round, "Megaspeed Drive Systems: Pushing Beyond 1 Million r/min," *IEEE/ASME Transactions on Mechatronics*, vol. 14, no. 5, pp. 564–574, Oct. 2009.

[2] A. Borisavljevic, H. Polinder, and J. A. Ferreira, "On the Speed Limits of Permanent-Magnet Machines," *IEEE Transactions on Industrial Electronics*, vol. 57, no. 1, pp. 220–227, Jan. 2010.

[3] G. F. Marshall and G. E. Stutz, *Handbook of Optical and Laser Scanning.* CRC Press, 2011.

[4] J. W. Beams, "High Rotational Speeds," *Journal of Applied Physics*, vol. 8, no. 12, pp. 795–806, 1937.

[5] J. W. Beams and J. L. Young, "Centrifugal Fields," *Phys. Rev.*, vol. 71, pp. 131–131, Jan 1947.

[6] R. Katano and S. Shimizu, "Production of Centrifugal Fields Greater Than 100 Million Times Gravity," *Review of Scientific Instruments*, vol. 50, no. 7, pp. 805–810, 1979.

[7] A. Boletis, "High Speed Micromotor on a Three Axis Active Magnetic Bearing," *PhD Thesis, EPFL*, 2005.

[8] J. W. Beams, "High Speed Centrifuging," *Reviews of Modern Physics*, vol. 10, no. 4, p. 245, 1938.

[9] T. Svedberg and J. B. Nichols, "Determination of Size and Distribution of Size of Particle by Centrifugal Methods," *Journal of the American Chemical Society*, vol. 45, no. 12, pp. 2910–2917, 1923.

[10] T. Svedberg, "The Ultra-Centrifuge and the Study of High-Molecular Compounds," *Nature*, pp. 1051–1062, 1937.

[11] E. Henriot and E. Huguenard, "Les Grandes Vitesses Angulaires Obtenues par les Rotors sans Axe Solide," *J. Phys. Radium*, vol. 8, no. 11, pp. 433–443, 1927.

[12] F. T. Holmes, "Axial Magnetic Suspensions," *Review of Scientific Instruments*, vol. 8, no. 11, pp. 444–447, 1937. [Online]. Available: http://dx.doi.org/10.1063/1.1752213.

[13] F. Holmes and J. Beams, "Frictional Torque of an Axial Magnetic Suspension," *Nature*, vol. 140, pp. 30–31, 1937.

[14] C. S. Smith, "High Rotational Speeds in Vacuum," *Review of Scientific Instruments*, vol. 12, no. 1, pp. 15–20, 1941. [Online]. Available: http://dx.doi.org/10.1063/1.1769773.

[15] L. E. MacHattie, "The Production of High Rotational Speed," *Review of Scientific Instruments*, vol. 12, no. 9, pp. 429–435, 1941.

[16] J. W. Beams, J. L. Young, and J. W. Moore, "The Production of High Centrifugal Fields," *Journal of Applied Physics*, vol. 17, no. 11, pp. 886–890, 1946. [Online]. Available: http://scitation.aip.org/content/aip/journal/jap/17/11/10.1063/1.1707658.

[17] J. W. Beams, "Magnetic Suspension for Small Rotors," *Review of Scientific Instruments*, vol. 21, no. 2, pp. 182–184, 1950. [Online]. Available: http://dx.doi.org/10.1063/1.1745523.

[18] C. Livermore, A. R. Forte, T. Lyszczarz, S. D. Umans, A. A. Ayon, and J. H. Lang, "A High-Power MEMS Electric Induction Motor," *Journal of Microelectromechanical Systems*, vol. 13, no. 3, pp. 465–471, 2004.

[19] C. Teo, L. Liu, H. Li, L. Ho, S. Jacobson, F. Ehrich, A. Epstein, and Z. Spakovszky, "High-Speed Operation of a Gas-Bearing Supported MEMS-Air Turbine," *Journal of Tribology*, vol. 131, no. 3, 2009.

[20] B. Sun, F. Han, L. Li, and Q. Wu, "Rotation Control and Characterization of High-Speed Variable-Capacitance Micromotor Supported on Electrostatic Bearing," *IEEE Transactions on Industrial Electronics*, vol. 63, no. 7, pp. 4336–4345, 2016.

[21] B. E. Kane, "Levitated Spinning Graphene Flakes in an Electric Quadrupole Ion Trap," *Phys. Rev. B*, vol. 82, p. 115441, Sep 2010. [Online]. Available: http://link.aps.org/doi/10.1103/PhysRevB.82.115441.

[22] Y. Arita, M. Mazilu, and K. Dholakia, "Laser-Induced Rotation and Cooling of a Trapped Microgyroscope in Vacuum," *Nature Communications*, vol. 4, 2013.

[23] Guinness World Records (2017). Highest Manmade Rpm. [Online]. Available: http://www.guinnessworldrecords.com/world-records/highest-manmade-rpm.

[24] K. Kim, J. Guo, Z. Liang, F. Zhu, and D. Fan, “Man-Made Rotary Nanomotors: A Review of Recent Developments,” *Nanoscale*, vol. 8, no. 20, pp. 10 471–10 490, 2016.

[25] K. Kim, X. Xu, J. Guo, and D. Fan, “Ultrahigh-Speed Rotating Nanoelectromechanical System Devices Assembled from Nanoscale Building Blocks,” *Nature Communications*, vol. 5, 2014.

[26] A. L. Balk, L. O. Mair, P. P. Mathai, P. N. Patrone, W. Wang, S. Ahmed, T. E. Mallouk, J. A. Liddle, and S. M. Stavis, “Kilohertz Rotation of Nanorods Propelled by Ultrasound, Traced by Microvortex Advection of Nanoparticles,” *ACS Nano*, vol. 8, no. 8, pp. 8300–8309, 2014.

[27] L. O. Mair, B. A. Evans, A. Nacev, P. Y. Stepanov, R. Hilaman, S. Chowdhury, S. Jafari, W. Wang, B. Shapiro, and I. N. Weinberg, “Magnetic Microkayaks: Propulsion of Microrods Precessing near a Surface by Kilohertz Frequency, Rotating Magnetic Fields,” *Nanoscale*, vol. 9, pp. 3375–3381, 2017. [Online]. Available: http://dx.doi.org/10.1039/C6NR09459G.

[28] A. Lehmuskero, R. Ogier, T. Gschneidtner, P. Johansson, and M. Käll, “Ultrafast Spinning of Gold Nanoparticles in Water Using Circularly Polarized Light,” *Nano Letters*, vol. 13, no. 7, pp. 3129–3134, 2013.

[29] L. Shao, Z.-J. Yang, D. Andrén, P. Johansson, and M. Käll, “Gold Nanorod Rotary Motors Driven by Resonant Light Scattering,” *ACS Nano*, vol. 9, no. 12, pp. 12 542–12 551, 2015. [Online]. Available: http://dx.doi.org/10.1021/acsnano.5b06311.

[30] U. Kafader and J. Schulze, “Similarity Relations in Electromagnetic Motors – Limitations and Consequences for the Design of Small DC Motors,” *Proc. 9th Int. Conf. New Actuators, (ACTUATOR’04)*, 2004, pp. 14–16.

[31] M. A. Rahman, A. Chiba, and T. Fukao, “Super High Speed Electrical Machines – Summary,” *IEEE Power Engineering Society General Meeting*, 2004, pp. 1272–1275.

[32] A. Binder and T. Schneider, “High-Speed Inverter-Fed AC Drives,” *International IEEE Aegean Conference on Electrical Machines and Power Electronics (ACEMP’07)*, 2007, pp. 9–16.

[33] C. Zwyssig, “An Ultra-High-Speed Electrical Drive System,” Ph.D. Dissertation, ETH Zurich, 2008.

[34] T. Baumgartner, “A Magnetically Levitated 500 000 RPM Electrical Drive System,” Ph.D. Dissertation, ETH Zurich, 2013.

[35] A. E. Looser, “Gas Bearing with Active Magnetic Damping for Ultra-High-Speed Electrical Drive Systems,” Ph.D. Dissertation, ETH Zurich, 2013.

[36] C. T. Chin, C. Lancée, J. Borsboom, F. Mastik, M. E. Frijlink, N. de Jong, M. Versluis, and D. Lohse, “Brandaris 128: A Digital 25 Million Frames per Second Camera with 128 Highly Sensitive Frames,” *Review of Scientific Instruments*, vol. 74, no. 12, pp. 5026–5034, 2003.

[37] E. C. Gelderblom, H. J. Vos, F. Mastik, T. Faez, Y. Luan, T. J. Kokhuis, A. F. van der Steen, D. Lohse, N. de Jong, and M. Versluis, “Brandaris 128 Ultra-High-Speed Imaging Facility: 10 Years of Operation, Updates, and Enhanced Features,” *Review of Scientific Instruments*, vol. 83, no. 10, p. 103706, 2012.

[38] J. W. Beams, E. Smith, and J. Watkins, “High-Constant-Speed Rotating Mirror,” *Journal of the Society of Motion Picture and Television Engineers*, vol. 58, no. 2, pp. 159–168, 1952.

[39] J. W. Beams, “Some Experiments on the Bursting of Spherical Rotors by Centrifugal Forces,” *Proceedings of the Society for Experimental Stress Analysis*, vol. 7, p. 1, 1949.

[40] J. W. Beams, J. B. Breazeale, and W. L. Bart, “Mechanical Strength of Thin Films of Metals,” *Phys. Rev.*, vol. 100, pp. 1657–1661, Dec 1955. [Online]. Available: http://link.aps.org/doi/10.1103/PhysRev.100.1657.

[41] J. W. Beams, “Production and Use of High Centrifugal Fields,” *Science*, vol. 120, no. 3121, pp. 619–625, 1954. [Online]. Available: http://science.sciencemag.org/content/120/3121/619.

[42] A. Boletis and H. Bleuler, “Achieving Ultra-High Rotating Speeds,” *8th International Symposium on Magnetic Bearings (ISMB)*, 2002, pp. 539–542.

[43] A. Boletis and H. Bleuler, "Three Axis AMB High Speed Micro Motor," *9th International Symposium on Magnetic Bearings (ISMB)*, 2004, pp. 1–6.

[44] W. D. Callister Jr and D. G. Rethwisch, *Fundamentals of Materials Science and Engineering: An Integrated Approach*. John Wiley & Sons, 2012.

[45] J. A. Collins, *Failure of Materials in Mechanical Design: Analysis, Prediction, Prevention*. John Wiley & Sons, 1993.

[46] H. Goldstein, *Classical Mechanics*. Pearson Education India, 2011.

[47] C. Lee, X. Wei, J. W. Kysar, and J. Hone, "Measurement of the Elastic Properties and Intrinsic Strength of Monolayer Graphene," *Science*, vol. 321, no. 5887, pp. 385–388, 2008.

[48] Y. Liu, B. Xie, Z. Zhang, Q. Zheng, and Z. Xu, "Mechanical Properties of Graphene Papers," *Journal of the Mechanics and Physics of Solids*, vol. 60, no. 4, pp. 591–605, 2012.

[49] S. Timoshenko and J. N. Goodier, *Theory of Elasticity*, 3rd ed. McGraw-Hill, 1970.

[50] E. J. Hearn, *Mechanics of Materials 2: The Mechanics of Elastic and Plastic Deformation of Solids and Structural Materials*. Butterworth-Heinemann, 1997.

[51] C. Chree, "The Stresses and Strains in Isotropic Elastic Solid Ellipsoid in Equilibrium under Bodily Forces Derivable from a Potential of the Second Degree," *Proceedings of the Royal Society of London*, vol. 58, no. 347-352, pp. 39–59, 1895. [Online]. Available: http://rspl.royalsocietypublishing.org/content/58/347-352/39.short.

[52] M. Goldberg and M. Sadowsky, "Stresses in an Ellipsoidal Rotor in a Centrifugal Force Field," *Journal of Applied Mechanics*, vol. 26, pp. 549–552, 1959.

[53] P. Washabaugh and D. J. Scheeres, "Energy and Stress Distributions in Ellipsoids," *Icarus*, vol. 159, no. 2, pp. 314–321, 2002.

[54] C. S. Jog, *Continuum Mechanics: Foundations and Applications of Mechanics*, 3rd ed. Cambridge University Press, 2015.

[55] A. I. Lurie, *Theory of Elasticity*. Springer, 2005.

[56] J. Braendlein, P. Eschmann, L. Hasbargen, and K. Weigand, *Ball and Roller Bearings: Theory, Design and Application*, 3rd ed. Wiley, 1999.

[57] D. Jiles, *Introduction to Magnetism and Magnetic Materials.* CRC press, 2015.

[58] F. Fiorillo, *Characterization and Measurement of Magnetic Materials.* Academic Press, 2005.

[59] S. Tumanski, *Handbook of Magnetic Measurements (Series in Sensors).* CRC Press, 2011.

[60] S. Foner, "Versatile and Sensitive Vibrating-Sample Magnetometer," *Review of Scientific Instruments*, vol. 30, no. 7, pp. 548–557, 1959. [Online]. Available: http://scitation.aip.org/content/aip/journal/rsi/30/7/10.1063/1.1716679.

[61] A. Zieba and S. Foner, "Detection Coil, Sensitivity Function, and Sample Geometry Effects for Vibrating Sample Magnetometers," *Review of Scientific Instruments*, vol. 53, no. 9, pp. 1344–1354, 1982.

[62] A. W. Pacyna and K. Ruebenbauer, "General Theory of a Vibrating Magnetometer with Extended Coils," *Journal of Physics E: Scientific Instruments*, vol. 17, no. 2, p. 141, 1984.

[63] R. Shull, R. McMichael, L. Swartzendruber, and S. Leigh, "Absolute Magnetic Moment Measurements of Nickel Spheres," *Journal of Applied Physics*, vol. 87, no. 9, pp. 5992–5994, 2000.

[64] B. J. Hamrock, S. R. Schmid, and B. O. Jacobson, *Fundamentals of Fluid Film Lubrication.* CRC press, 2004.

[65] H. Bleuler, M. Cole, P. Keogh, R. Larsonneur, E. Maslen, Y. Okada, G. Schweitzer, A. Traxler *et al.*, *Magnetic Bearings: Theory, Design, and Application to Rotating Machinery.* Springer, 2009.

[66] A. Chiba, T. Fukao, O. Ichikawa, M. Oshima, M. Takemoto, and D. G. Dorrell, *Magnetic Bearings and Bearingless Drives.* Elsevier, 2005.

[67] W. Trimmer and K. Gabriel, "Design Considerations for a Practical Electrostatic Micro-Motor," *Sensors and Actuators*, vol. 11, no. 2, pp. 189–206, 1987.

[68] S. F. Bart, T. A. Lober, R. T. Howe, J. H. Lang, and M. F. Schlecht, "Design Considerations for Micromachined Electric Actuators," *Sensors and Actuators*, vol. 14, no. 3, pp. 269–292, 1988.

[69] N. Maluf and K. Williams, *An Introduction to Microelectromechanical Systems Engineering.* Artech House, 2004.

[70] W.-K. Rhim, S. K. Chung, D. Barber, K. F. Man, G. Gutt, A. Rulison, and R. E. Spjut, "An Electrostatic Levitator for High-Temperature Containerless Materials Processing in 1-g," *Review of Scientific Instruments*, vol. 64, no. 10, pp. 2961–2970, 1993.

[71] P. L. Chapman and P. T. Krein, "Smaller Is Better? [Micromotors and Electric Drives]," *IEEE Industry Applications Magazine*, vol. 9, no. 1, pp. 62–67, 2003.

[72] F. Paschen, "Ueber die zum Funkenübergang in Luft, Wasserstoff und Kohlensäure bei verschiedenen Drucken erforderliche Potentialdifferenz," *Annalen der Physik*, vol. 273, no. 5, pp. 69–96, 1889.

[73] E. Husain and R. Nema, "Analysis of Paschen Curves for Air, N2 and SF6 using the Townsend Breakdown Equation," *IEEE Transactions on Electrical Insulation*, no. 4, pp. 350–353, 1982.

[74] H. Bleuler, "A Survey of Magnetic Levitation and Magnetic Bearing Types," *JSME International Journal. Ser. 3, Vibration, Control Engineering, Engineering for Industry*, vol. 35, no. 3, pp. 335–342, 1992.

[75] S. Earnshaw, "On the Nature of the Molecular Forces Which Regulate the Constitution of the Luminiferous Ether," *Trans. Camb. Phil. Soc*, vol. 7, pp. 97–112, 1842.

[76] E. Okress, D. Wroughton, G. Comenetz, P. Brace, and J. Kelly, "Electromagnetic Levitation of Solid and Molten Metals," *Journal of Applied Physics*, vol. 23, no. 5, pp. 545–552, 1952.

[77] P. R. Rony, "The Electromagnetic Levitation of Metals," Lawrence Radiation Laboratory and University of California, Berkeley, Technical Report, 1964.

[78] E. Fromm and H. Jehn, "Electromagnetic Forces and Power Absorption in Levitation Melting," *British Journal of Applied Physics*, vol. 16, no. 5, p. 653, 1965.

[79] L. Holmes, "Stability of Magnetic Levitation," *Journal of Applied Physics*, vol. 49, no. 6, pp. 3102–3109, 1978.

[80] J. Priede and G. Gerbeth, “Stability Analysis of an Electromagnetically Levitated Sphere,” *Journal of Applied Physics*, vol. 100, no. 5, p. 054911, 2006.

[81] O. Muck, “Verfahren und Vorrichtung zum Schmelzen, insbesondere von Leitern u. dgl. durch elektrische Induktionsstroeme,” Patent DE422 004, 1925.

[82] J. Jackson, *Classical Electrodynamics*. Wiley, 1999.

[83] J.-P. Yonnet, “Permanent Magnet Bearings and Couplings,” *IEEE Transactions on Magnetics*, vol. 17, no. 1, pp. 1169–1173, 1981.

[84] P. S. Epstein, “On the Resistance Experienced by Spheres in Their Motion through Gases,” *Physical Review*, vol. 23, no. 6, p. 710, 1924.

[85] Y. W. Yap and J. E. Sader, “Sphere Oscillating in a Rarefied Gas,” *Journal of Fluid Mechanics*, vol. 794, pp. 109–153, 005 2016. [Online]. Available: https://www.cambridge.org/core/article/div-class-title-sphere-oscillating-in-a-rarefied-gas-div/923259AB688D63ED147904199009C494.

[86] J. K. Fremerey, “The Spinning Rotor Gauge,” *Journal of Vacuum Science & Technology A: Vacuum, Surfaces, and Films*, vol. 3, no. 3, pp. 1715–1720, 1985. [Online]. Available: http://dx.doi.org/10.1116/1.573007.

[87] J. Fremerey, “Residual Drag Torque on Magnetically Suspended Rotating Spheres,” *Review of Scientific Instruments*, vol. 43, no. 10, pp. 1413–1417, 1972.

[88] J. Beams, “Rotors Driven by Light Pressure,” *Physical Review*, vol. 72, no. 10, p. 987, 1947.

[89] H. Hertz, “Über die Induction in rotirenden Kugeln,” Ph.D. Dissertation, Humboldt-Universität zu Berlin, 1880.

[90] T. Reichert, T. Nussbaumer, and J. W. Kolar, “Complete Analytical Solution of Electromagnetic Field Problem of High-Speed Spinning Ball,” *Journal of Applied Physics*, vol. 112, no. 10, pp. –, 2012. [Online]. Available: http://scitation.aip.org/content/aip/journal/jap/112/10/10.1063/1.4765676.

[91] W. R. Smythe, *Static and Dynamic Electricity*, 3rd ed. CRC Press, 1989.

[92] E. Michaelides, C. T. Crowe, and J. D. Schwarzkopf, *Multiphase Flow Handbook.* CRC Press, 2016.

[93] J. F. O'Hanlon, *A User's Guide to Vacuum Technology.* John Wiley & Sons, 2003.

[94] K. Jousten, *Handbook of Vacuum Technology.* John Wiley & Sons, 2016.

[95] O. Sawatzki, "Das Strömungsfeld um eine rotierende Kugel," *Acta Mechanica*, vol. 9, no. 3-4, pp. 159–214, 1970.

[96] H. Lamb, *Hydrodynamics.* Cambridge University Press, 1932.

[97] W. H. H. Banks, "The Laminar Boundary Layer on a Rotating Sphere," *Acta Mechanica*, vol. 24, no. 3, pp. 273–287, Sep 1976. [Online]. Available: https://doi.org/10.1007/BF01190376.

[98] F. P. Bowden and R. G. Lord, "The Aerodynamic Resistance to a Sphere Rotating at High Speed," *Proceedings of the Royal Society of London A: Mathematical, Physical and Engineering Sciences*, vol. 271, no. 1345, pp. 143–153, 1963. [Online]. Available: http://rspa.royalsocietypublishing.org/content/271/1345/143.

[99] L. Howarth, "Note on the Boundary Layer on a Rotating Sphere," *The London, Edinburgh, and Dublin Philosophical Magazine and Journal of Science*, vol. 42, no. 334, pp. 1308–1315, 1951.

[100] O. Sawatzki and J. Zierep, "Das Stromfeld im Spalt zwischen zwei konzentrischen Kugelflächen, von denen die innere rotiert," *Acta Mechanica*, vol. 9, no. 1, pp. 13–35, Mar 1970. [Online]. Available: https://doi.org/10.1007/BF01176606.

[101] Q. Liu and A. Prosperetti, "Wall Effects on a Rotating Sphere," *Journal of Fluid Mechanics*, vol. 657, pp. 1–21, 2010.

[102] J. W. Beams, D. M. Spitzer Jr., and J. P. Wade Jr., "Spinning Rotor Pressure Gauge," *Review of Scientific Instruments*, vol. 33, no. 2, pp. 151–155, 1962. [Online]. Available: http://dx.doi.org/10.1063/1.1746520.

[103] P. Harbour and R. Lord, "A Rotating Sphere, Absolute Vacuum Gauge," *Journal of Scientific Instruments*, vol. 42, no. 2, p. 105, 1965.

[104] R. Feres and G. Yablonsky, "Knudsen's Cosine Law and Random Billiards," *Chemical Engineering Science*, vol. 59, no. 7, pp. 1541–1556, 2004.

[105] F. C. Hurlbut, "Studies of Molecular Scattering at the Solid Surface," *Journal of Applied Physics*, vol. 28, no. 8, pp. 844–850, 1957. [Online]. Available: http://dx.doi.org/10.1063/1.1722872.

[106] D. H. Gabis, S. K. Loyalka, and T. S. Storvick, "Measurements of the Tangential Momentum Accommodation Coefficient in the Transition Flow Regime with a Spinning Rotor Gauge," *Journal of Vacuum Science & Technology A: Vacuum, Surfaces, and Films*, vol. 14, no. 4, pp. 2592–2598, 1996. [Online]. Available: http://dx.doi.org/10.1116/1.579986.

[107] J. A. Bentz, R. V. Tompson, and S. K. Loyalka, "Measurements of Viscosity, Velocity Slip Coefficients, and Tangential Momentum Accommodation Coefficients Using a Modified Spinning Rotor Gauge," *Journal of Vacuum Science & Technology A: Vacuum, Surfaces, and Films*, vol. 19, no. 1, pp. 317–324, 2001. [Online]. Available: http://dx.doi.org/10.1116/1.1335833.

[108] R. Lord and P. Harbour, "An Approximate Method of Calculating Transition Regime Heat Transfer and Shear," *AIAA Journal*, vol. 6, no. 2, p. 244, 1968.

[109] F. P. Bowden and P. J. Harbour, "The Aerodynamic Resistance to a Sphere Rotating at High Mach Numbers in the Rarefied Transition Regime," *Proceedings of the Royal Society of London A: Mathematical, Physical and Engineering Sciences*, vol. 293, no. 1433, pp. 156–168, 1966. [Online]. Available: http://rspa.royalsocietypublishing.org/content/293/1433/156.

[110] F. Kreith, "Convection Heat Transfer in Rotating Systems," *Advances in Heat Transfer*, vol. 5, pp. 129–251, 1969.

[111] E. H. Kennard, *Kinetic Theory of Gases.* McGraw-Hill, 1938.

[112] A. Filippov and D. Rosner, "Energy Transfer between an Aerosol Particle and Gas at High Temperature Ratios in the Knudsen Transition Regime," *International Journal of Heat and Mass Transfer*, vol. 43, no. 1, pp. 127–138, 2000.

[113] G. S. Springer, "Heat Transfer in Rarefied Gases," *Advances in Heat Transfer*, vol. 7, pp. 163–218, 1971.

[114] C. Yunus and J. G. Afshin, "Heat and Mass Transfer: Fundamentals and Applications," *McGraw-Hill*, pp. 488–489, 2011.

[115] D. G. Holmes and T. A. Lipo, *Pulse Width Modulation for Power Converters: Principles and Practice.* John Wiley & Sons, 2003.

[116] J. Muehlethaler, "Modeling and Multi-Objective Optimization of Inductive Power Components," Ph.D. Dissertation, ETH Zurich, 2012.

[117] W. G. Hurley, E. Gath, and J. G. Breslin, "Optimizing the AC Resistance of Multilayer Transformer Windings with Arbitrary Current Waveforms," *IEEE Transactions on Power Electronics*, vol. 15, no. 2, pp. 369–376, 2000.

[118] X. Nan and C. Sullivan, "Simplified High-Accuracy Calculation of Eddy-Current Loss in Round-Wire Windings," *35th IEEE Power Electronics Specialists Conference (PESC'04)*, 2004, pp. 873–879. [Online]. Available: http://ieeexplore.ieee.org/stamp/stamp.jsp?arnumber=1355533.

[119] *2605SA1 Magnetic Alloy*, Metglas, 2011.

[120] *3C90 Material Specification*, Ferroxcube, 2008.

[121] K. Venkatachalam, C. Sullivan, T. Abdallah, and H. Tacca, "Accurate Prediction of Ferrite Core Loss with Nonsinusoidal Waveforms Using Only Steinmetz Parameters," *IEEE Workshop on Computers in Power Electronics*, 2002, pp. 36–41. [Online]. Available: http://ieeexplore.ieee.org/stamp/stamp.jsp?arnumber=1196712.

[122] J. Muehlethaler, J. Biela, J. W. Kolar, and A. Ecklebe, "Core Losses under the DC Bias Condition Based on Steinmetz Parameters," *IEEE Transactions on Power Electronics*, vol. 27, no. 2, pp. 953–963, 2012.

[123] A. J. Moulson and J. M. Herbert, *Electroceramics: Materials, Properties, Applications.* John Wiley & Sons, 2003.

[124] R. S. Elliot, *Electromagnetics: History, Theory, and Applications.* IEEE, 1993.

[125] J. Boehm, R. Gerber, and N. Kiley, "Sensors for Magnetic Bearings," *IEEE Transactions on Magnetics*, vol. 29, no. 6, pp. 2962–2964, 1993.

[126] C. Dodd and W. Deeds, "Analytical Solutions to Eddy-Current Probe-Coil Problems," *Journal of Applied Physics*, vol. 39, no. 6, pp. 2829–2838, 1968.

[127] J. Haus, *Optical Sensors: Basics and Applications.* Wiley, 2010.

[128] M. Giubilato and S. Mattiazzo, "Novel Imaging Sensor for High Rate and High Resolution Applications," *Proceedings of the SNIC Symposium*, 2006, pp. 1–6.

[129] Y. Sugiyama, Y. Matsui, H. Toyoda, N. Mukozaka, A. Ihori, T. Abe, M. Takabe, and S. Mizuno, "A 3.2 kHz, 14-bit Optical Absolute Rotary Encoder with a CMOS Profile Sensor," *IEEE Sensors Journal*, vol. 8, no. 8, pp. 1430–1436, 2008.

[130] *Two-Dimensional PSD S5990-01*, Hamamatsu Photonics, 5 2013.

[131] H. J. Woltring, "Single- and Dual-Axis Lateral Photodetectors of Rectangular Shape," *IEEE Transactions on Electron Devices*, vol. 22, no. 8, pp. 581–590, 1975.

[132] Hamamatsu, *Hamamatsu Opto-Semiconductor Handbook*, Hamamatsu Photonics, May 2013.

[133] U. Tietze, C. Schenk, and E. Gamm, *Electronic Circuits: Handbook for Design and Application.* Springer, 2015.

[134] H. K. Khalil, *Nonlinear Systems*, 3rd ed. Prentice Hall, 2002.

[135] T. Başar and P. Bernhard, *H-Infinity Optimal Control and Related Minimax Design Problems: A Dynamic Game Approach.* Springer Science & Business Media, 2008.

[136] L. T. Harrison, *Current Sources and Voltage References: A Design Reference for Electronics Engineers.* Newnes, 2005.

[137] S. Franco, *Design with Operational Amplifiers and Analog Integrated Circuits.* McGraw-Hill Series in Electrical and Computer Engineering, 2015.

[138] G. R. Stanley and K. M. Bradshaw, "Precision DC-to-AC Power Conversion by Optimization of the Output Current Waveform – The Half Bridge Revisited," *IEEE Transactions on Power Electronics*, vol. 14, no. 2, pp. 372–380, 1999.

[139] J. Schellekens, J. Duarte, H. Huisman, and M. Hendrix, "Elimination of Zero-Crossing Distortion for High-Precision Amplifiers," *37th Conference of the IEEE Industrial Electronics Society (IECON'11)*, 2011, pp. 3370–3375.

[140] M. Mauerer, A. Tüysüz, and J. W. Kolar, "Distortion Analysis of Low-THD/High-Bandwidth GaN/SiC Class-D Amplifier Power Stages," *IEEE Energy Conversion Congress and Exposition (ECCE'15)*, 2015, pp. 2563–2571.

[141] J. R. Davis, *Metals Handbook*. ASM International, 1998.

[142] H. Bhadeshia, "Steels for Bearings," *Progress in Materials Science*, vol. 57, no. 2, pp. 268 – 435, 2012. [Online]. Available: http://www.sciencedirect.com/science/article/pii/S0079642511000922.

[143] E. V. Zaretsky, "Rolling Bearing Steels – A Technical and Historical Perspective," *Materials Science and Technology*, vol. 28, no. 1, pp. 58–69, 2012.

[144] E. Pavlina and C. Van Tyne, "Correlation of Yield Strength and Tensile Strength with Hardness for Steels," *Journal of Materials Engineering and Performance*, vol. 17, no. 6, pp. 888–893, 2008. [Online]. Available: http://dx.doi.org/10.1007/s11665-008-9225-5.